



Università di Pisa

DIPARTIMENTO DI FISICA
Corso di Laurea Magistrale in Fisica

TESI DI LAUREA MAGISTRALE

**A novel method for tau-lepton lifetime measurement
with early Belle II data**

Candidato:
Stefano Moneta

Relatori:
Prof. Francesco Forti
Prof. Eugenio Paoloni

Abstract

The Belle II experiment, operating at the SuperKEKB electron-positron collider, is going to collect 50 ab^{-1} of integrated luminosity by 2030, a factor 50 more than its predecessors. The large cross section for $e^+e^- \rightarrow \tau^+\tau^-$ at the $\Upsilon(4S)$ resonance energy, will yield to about 46 billion produced τ pairs, making Belle II, besides a B -factory, a τ -factory as well.

The τ -lepton is a powerful laboratory for both Standard Model (SM) and beyond SM measurements. A precise τ lifetime measurement, in particular, can contribute to the test of lepton flavor universality within the SM. Also, lifetime measurements are very effective tools to monitor detector performance and alignment. Furthermore, they are challenging in case of a particle such as τ -lepton, whose lifetime uncertainty is below 0.2% at present. To achieve a competitive precision a very good understanding of detector performance is needed. At Belle II, τ pairs have an expected mean decay length of about $250 \mu\text{m}$.

In this thesis, a new method for τ lifetime measurement is studied. The method aims to fully reconstruct $e^+e^- \rightarrow \tau^+\tau^-$ events, where both taus decay with one neutrino only, i.e. hadronically. For this class of events, which potentially represents 42% of the total τ pair decays, τ four-momenta can be reconstructed up to a two-fold ambiguity, just measuring the momenta of all hadronic final states and requiring four-momentum conservation. Thanks to the nano-beam collision scheme adopted by SuperKEKB machine, the beam spot size at the interaction point is much smaller than in any of the previous collider experiments. The primary vertex position on the transverse plane can hence be treated as a fixed constraint. Using the information on the impact parameter of reconstructed tracks, the vertex relations can be included in a unique system of equations together with the kinematic relationships. The system can be numerically solved through a χ^2 -like minimization where the τ decay lengths and momenta, as well as the primary vertex position along the beam direction, are considered as free parameters.

The method proposed is tested for the 1-prong \times 3-prong decay topology, where the vertex position of the 3-prong τ can be independently fitted. A selection of these events in Belle II had been developed on Monte Carlo and applied on 34.6 fb^{-1} data, collected during 2019 and early 2020 runs. The full event reconstruction method gives a proper decay time resolution $\sigma(t) = 65 \text{ fs}$, obtained for the 3-prong side. In addition, the interaction point along the beam direction (z direction) is also reconstructed

with a resolution $\sigma(\text{IP}_z) = 20 \mu\text{m}$, thus making possible a precise event per event monitoring of the beam spot position.

Contents

Introduction	vii
1 Physics motivation	1
1.1 The Standard Model	1
1.1.1 Possible extensions	4
1.2 Tau physics	5
1.2.1 Tau Lepton Flavor Violating decays	6
1.2.2 Lepton Flavor Universality	6
2 The Belle II experiment	13
2.1 SuperKEKB	13
2.1.1 Nano-beam scheme	14
2.2 Belle II detector	16
2.2.1 Vertex Detector	17
2.2.2 Central Drift Chamber	18
2.2.3 Particle Identification Detector	19
2.2.4 Electromagnetic Calorimeter	20
2.2.5 K_L and μ detector	21
2.3 Software and reconstruction	21
2.3.1 Monte Carlo generators	22
2.3.2 Tracking	22
2.3.3 ECL clusters	23
2.3.4 Vertex Fitter	24
2.4 Operations and future plans	24
3 τ lifetime reconstruction method	27
3.1 Lifetime measurement	27
3.2 Previous methods	28
3.2.1 LEP	28
3.2.2 $\Upsilon(4S)$ and B-factories	31
3.3 Full reconstruction method	33
3.3.1 Kinematic reconstruction	33
3.3.2 Decay length reconstruction at Belle II	36

3.3.3	Full reconstruction	38
3.4	Reconstruction procedure	40
3.4.1	Reconstruction of tau pair momenta	41
3.4.2	Reconstruction of tau decay time	42
4	Event selection and reconstruction	47
4.1	Event Topology	47
4.1.1	Background sources	48
4.2	Dataset	50
4.2.1	Data samples	50
4.2.2	Monte Carlo samples	50
4.3	Event selection	51
4.3.1	Preselection	51
4.3.2	Data/MC agreement	55
4.3.3	Optimization cuts	58
4.4	Candidate reconstruction	60
4.4.1	Tau momentum reconstruction	61
4.4.2	Tau Lifetime reconstruction	63
5	τ lifetime extraction	65
5.1	Reconstructed parameters	65
5.1.1	Tau candidate kinematics	65
5.1.2	Interaction Point	66
5.2	Resolution function	67
5.2.1	Resolution on signal	68
5.2.2	Background subtraction	72
5.3	Lifetime fit	75
	Conclusions and outlook	79
	Bibliography	81

Introduction

The Standard Model (SM) provides a consistent theory for electroweak and strong interactions. Still, several experimental observations as dark matter, neutrino oscillations, and matter-antimatter asymmetry are not explained within SM. It is therefore a general belief that this model needs to be extended but, at the energy scales directly accessible by hadron colliders, no evidence of Beyond Standard Model (BSM) particles has yet been found. Pushing on the intensity frontier in high precision experiments is now the most promising path for testing the SM and indirectly accessing BSM physics.

Belle II is currently one of the leading experiment at the luminosity frontier. Located at the SuperKEKB asymmetric $e^+ e^-$ collider, operating at the center of mass energy of $\Upsilon(4s)$, it plans to collect 50 ab^{-1} integrated luminosity by 2030. Besides being a B -factory, Belle II is also the best laboratory to study τ -lepton physics. With a tau pair production cross section $\sigma(ee \rightarrow \tau\tau) = 0.919 \text{ nb}$, about 50×10^9 tau pairs will be produced in a clean environment during the full operation. Such amount will be by far the highest ever acquired, exceeding by a factor 50 the previous generation B -factories BaBar and Belle.

The aim of this thesis is to study a new method for the τ -lepton lifetime measurement, which can take advantage of the large $\tau\tau$ sample produced, the clean environment of an $e^+ e^-$ collider such SuperKEKB, and the new vertex detector of Belle II.

In Chapter 1, after a general introduction to the electroweak SM framework, an overview of the most important experimental tests to the SM Lepton Flavor Universality is presented. An important ingredient of one of these tests is the τ -lepton lifetime. Chapter 2 describes the SuperKEKB colliding scheme, the Belle II detector and the software framework. The novel method developed for this thesis is outlined along chapter 3, and in chapter 4 a τ pair decay topology is selected in order to test the method on a early Belle II data sample. Finally, in chapter 5, we present a preliminary study to extract the tau lifetime from the reconstructed proper time.

Chapter 1

Physics motivation

In this chapter a brief introduction of the Standard Model is given, focusing especially on the electroweak sector. Focusing on the tau physics, the present status of experimental tests on the SM Lepton Flavor Universality are given.

1.1 The Standard Model

The Standard Model (SM) of particle physics describes the known fundamental constituents of the Universe and their interactions. SM framework (Figure 1.1) includes 12 spin-1/2 matter constituents divided into 3 lepton generations, 3 quark generations, 4 vector gauge bosons and 1 scalar Higgs [1].

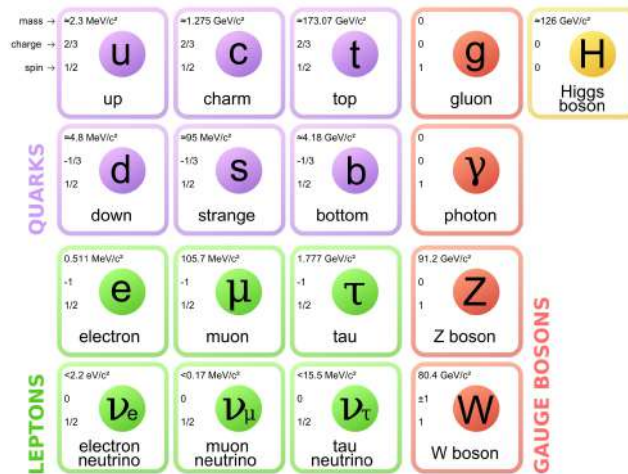


Figure 1.1: The elementary particles of the Standard Model. The model contains 12 spin-1/2 fermions: 6 quarks and 6 leptons, divided into 3 flavor families (columns). 4 gauge bosons account for strong (gluon), electromagnetic (photon) and weak (Z , W) interactions. Finally, the Higgs scalar boson generates the masses of leptons and gauge bosons through the spontaneous symmetry breaking.

In the quantum field theory scheme, the SM is described by a Lagrangian invariant under the action of the local gauge symmetry group $SU(3)_C \otimes SU(2)_L \otimes U(1)_Y$. $SU(3)_C$ is the symmetry group of quantum chromodynamics (QCD) while $SU(2)_L \otimes U(1)_Y$ determines the electroweak theory (EW). The two theories are combined in the Standard Model Lagrangian [2]

$$\mathcal{L}_{SM} = \mathcal{L}_{QCD} + \mathcal{L}_{EW}$$

The QCD Lagrangian \mathcal{L}_{QCD} describes strong interactions. In the fundamental representation of $SU(3)_C$ quark fields transform as triplets and thus they assume 3 possible strong charge values, called color charge, usually denoted as R, G and B (Red, Green and Blue). There are 8 independent group generators to which correspond 8 spin-1 massless gauge fields called gluons.

The electroweak Lagrangian \mathcal{L}_{EW} is built requiring local gauge symmetry $SU(2)_L \otimes U(1)_Y$, i.e. invariance under weak isospin and weak hypercharge transformations. In the fundamental representation, the $SU(2)_L$ group generator is a weak isospin triplet $\vec{\tau} = (\tau^1, \tau^2, \tau^3)$, which couples to the 3 massless vector gauge bosons $\vec{W}_\mu = (W_\mu^1, W_\mu^2, W_\mu^3)$ with a coupling constant g . All fermions are represented by left-handed weak isospin doublets L . Explicitly, for leptons and quarks:

$$L = \begin{pmatrix} \nu_e \\ e^- \end{pmatrix}_L \quad \begin{pmatrix} \nu_\mu \\ \mu^- \end{pmatrix}_L \quad \begin{pmatrix} \nu_\tau \\ \tau^- \end{pmatrix}_L \quad \begin{pmatrix} u \\ d' \end{pmatrix}_L \quad \begin{pmatrix} c \\ s' \end{pmatrix}_L \quad \begin{pmatrix} t \\ b' \end{pmatrix}_L$$

The weak isospin eigenvalues of the τ^3 operator are $T^3 = +1/2$, for the upper component in the doublet, and $T^3 = -1/2$, for the lower one. Right-handed fermions are singlets with $T^3 = 0$. The eigenstates of weak-isospin d', s', b' are mixtures of the mass eigenstates d, s, b via the Cabibbo-Kobayashi-Maskawa (CKM) unitary matrix:

$$\begin{pmatrix} d' \\ s' \\ b' \end{pmatrix} = \begin{pmatrix} V_{ud} & V_{us} & V_{ub} \\ V_{cd} & V_{cs} & V_{cb} \\ V_{td} & V_{ts} & V_{tb} \end{pmatrix} \begin{pmatrix} d \\ s \\ b \end{pmatrix}$$

The CKM matrix contains 4 independent parameters (3 angles and 1 phase). Similarly, the neutrino $SU(2)_L$ eigenstates are related to the mass eigenstates through the unitary Pontecorvo-Maki-Nakagawa-Sakata (PMNS) matrix:

$$\begin{pmatrix} \nu_e \\ \nu_\mu \\ \nu_\tau \end{pmatrix} = \begin{pmatrix} U_{1e} & U_{2e} & U_{3e} \\ U_{1\mu} & U_{2\mu} & U_{3\mu} \\ U_{1\tau} & U_{2\tau} & U_{3\tau} \end{pmatrix} \begin{pmatrix} \nu_1 \\ \nu_2 \\ \nu_3 \end{pmatrix}$$

which also contains other 4 independent parameters (3 mixing angles and a phase).

Finally, in the fundamental representation of $U(1)_Y$, there is only one massless vector gauge boson B_μ , coupling to the generator singlet Y with a constant g' . The elements are singlet of $U(1)_Y$ and the weak hypercharge operator Y acts like

$$Y = 2(Q - T^3)$$

where Q is the electromagnetic charge and T^3 is the eigenvalue of τ^3 .

The gauge symmetry in the Lagrangian is obtained substituting the derivatives ∂^μ with the covariant ones. For the electroweak $SU(2)_L \otimes U(1)_Y$ gauge group:

$$\partial^\mu \longrightarrow D^\mu = \partial^\mu + ig\vec{\tau} \cdot \vec{W}^\mu + ig'\frac{Y}{2}B^\mu$$

Higgs mechanism

Masses of fermions and gauge bosons are generated by the $SU(2)_L \otimes U(1)_Y$ gauge invariant coupling with the Higgs field. The SM predicts one Higgs boson consisting of two complex scalar fields placed in a weak isospin doublet with weak hypercharge $Y = 1$

$$\phi = \begin{pmatrix} \phi^+ \\ \phi^0 \end{pmatrix}$$

The Higgs Lagrangian, written such as to be $SU(2)_L \otimes U(1)_Y$ local gauge invariant, is

$$\mathcal{L}_{Higgs} = (D_\mu \phi)^\dagger (D^\mu \phi) - V(\phi) \quad V(\phi) = \mu^2 (\phi^\dagger \phi) + \lambda (\phi^\dagger \phi)^2$$

$V(\phi)$ is the Higgs potential with $\mu^2 < 0$ and $\lambda > 0$. In order to apply perturbation theory, the potential should be expanded around its minimum. However, $V(\phi)$ has not a minimum for $\phi = (0, 0)$ as usually happens, but a set of infinite degenerate minima for

$$\phi^\dagger \phi = -\frac{\mu^2}{2\lambda}$$

and the choice of a minimum leads to (spontaneous) symmetry break. The minimum chosen is

$$\phi = \frac{1}{\sqrt{2}} \begin{pmatrix} 0 \\ v \end{pmatrix}$$

such that $\langle 0 | \phi^+ | 0 \rangle = 0$ and $\langle 0 | \phi^0 | 0 \rangle = v/\sqrt{2}$ where $v = \sqrt{-\mu^2/\lambda}$ is the vacuum expectation value. The Higgs field can be expanded around this minimum and redefined in unitary gauge as

$$\phi = \frac{1}{\sqrt{2}} \begin{pmatrix} 0 \\ v + h \end{pmatrix} \quad (1.1)$$

Substituting inside \mathcal{L}_{Higgs} , the kinetic part can be rearranged to have explicit mass terms:

$$\left(\frac{1}{2}vg\right)^2 W_\mu^+ W^{-\mu} + \frac{1}{8}v^2 (A^\mu \quad Z^\mu) \begin{pmatrix} 0 & 0 \\ 0 & g^2 + g'^2 \end{pmatrix} \begin{pmatrix} A^\mu \\ Z^\mu \end{pmatrix}$$

Here the physical weak and electromagnetic fields $(W^\pm)^\mu$, Z^μ , A^μ appeared with their respective mass terms. Regarding the charged weak boson:

$$W^\pm = \frac{1}{\sqrt{2}} (W^1 \mp iW^2) \quad M_W = \frac{1}{2}vg$$

While the physical electromagnetic field A^μ and neutral weak field Z^μ are linear combinations of B^μ and W_3^μ through the mixing matrix

$$\begin{pmatrix} A^\mu \\ Z^\mu \end{pmatrix} = \begin{pmatrix} \cos \theta_W & \sin \theta_W \\ -\sin \theta_W & \cos \theta_W \end{pmatrix} \begin{pmatrix} B^\mu \\ W_3^\mu \end{pmatrix}$$

their masses are $M_A = 0$ and $M_Z = \frac{1}{2}v\sqrt{g^2 + g'^2}$. θ_W is known as Weinberg angle and $\tan \theta_W = g'/g$. It can also be expressed as a function of weak boson masses:

$$\cos \theta_W = \frac{M_W}{M_Z}$$

The remaining terms of $(D_\mu\phi)^\dagger(D^\mu\phi)$ determine the coupling between Higgs field and weak bosons. From the potential $V(\phi)$ the Higgs mass $M_H = \sqrt{2\lambda}v$ is obtained as well as the self coupling terms.

Fermion masses are also generated from the interaction with the Higgs field. In particular, for charged leptons and down type quarks, an interaction Lagrangian invariant under $SU(2)_L \otimes U(1)_Y$ can be written as

$$\mathcal{L} = -g_f \bar{L}\phi R \tag{1.2}$$

where g_f is the Yukawa coupling constant for the fermion f , whose value is not a priori predicted by the SM. L and R are left-handed and right-handed chiral spinors, i.e. a doublet and a singlet under the $SU(2)_L$ symmetry. After the spontaneous symmetry breaking, the Higgs isospin doublet ϕ can be expressed as (1.1).

Inserting everything in the Lagrangian (1.2)

$$\mathcal{L} = -\frac{g_f}{\sqrt{2}}v \bar{f}f - \frac{g_f}{\sqrt{2}}\bar{f}fh \tag{1.3}$$

The first term is the fermion mass term with $m_f = g_f v/\sqrt{2}$, while the second one accounts for the interaction between the fermionic current and the Higgs boson and it is proportional to m_f/v . An analogous Lagrangian is obtained for the up-type quarks.

1.1.1 Possible extensions

The minimal SM described above contains 25 independent free parameters:

- 12 Yukawa terms determining the fermion masses
- 3 coupling constants for the gauge interactions: α_s , g and g'
- 2 parameters μ and λ describing the Higgs potential
- 4 parameters for the mixing of down type quarks (CKM matrix)
- 4 parameters accounting for neutrino oscillations (PMNS matrix)

Table 1.1: List of present, past and foreseen τ -factories recording the highest number of tau pairs. The Future electron-positron Circular Collider (FCC-ee) would initially operate at the Z-peak invariant mass. Up to that, Belle II is expected to collect the largest number of tau pairs in a e^+e^- collider.

τ factory	CMS energy	$N(e^+e^- \rightarrow \tau^+\tau^-)$
LEP I	Z-pole	$\approx 10^8$
KEKB + PEP II	$\Upsilon(4S)$	$\approx 10^9$
SuperKEKB (2030)	$\Upsilon(4S)$	$\approx 5 \times 10^{10}$
FCC-ee (~ 2045)	Z-pole	$\approx 10^{11}$

Some subtended patterns, such as the fact that fermions are grouped into three mass-hierarchy families, or that the coupling constants α_s , g and g' are approximately of the same order of magnitude, seem to suggest an underlined symmetry beyond the SM. The introduction of a new and larger (broken) symmetry could reduce the high number of free parameters and possibly explain some of the open issues left in the SM. One of the most intriguing is the experimental evidence, at the cosmological level, of the presence of a dark matter, incompatible with any of the SM particles [3].

A possible extension of SM is the Supersymmetry (SUSY) theory, which, for each SM particle, predicts the existence of a supersymmetric partner with different spin. SUSY partners of leptons and quarks are scalar sleptons and squarks, the correspondent of gauge bosons are spin-1/2 gauginos while the vector Higgsino is the partner of the Higgs. There are several SUSY models where the lightest supersymmetric particle is a suitable dark matter candidate. To date, SUSY particles have been directly searched at the Large Hadron Collider (LHC) excluding masses below ~ 1 TeV [4].

1.2 Tau physics

The τ -lepton represents a good probe for testing the SM. Because of its high mass, it is believed to couple strongly with beyond SM particles and it could be a preferred channel for new physics discoveries. Furthermore, as it is the only lepton which can decay to hadrons and its decays are well-understood, the τ -lepton can be exploited for precision QCD measurements at the 1 GeV energy scale.

Electron-positron colliders are particularly suitable for investigating tau physics. Tau leptons are produced in pairs through the electroweak process $e^+e^- \rightarrow \gamma/Z \rightarrow \tau^+\tau^-$ which has a cross section comparable with $e^+e^- \rightarrow \text{hadrons}$ background. In addition, since the tau decays with neutrinos, a good reconstruction of the event missing momentum is possible at lepton colliders where, unlike hadron collider, the total initial energy could be known with precision.

High luminosity electron-positron colliders have been designed for precise measurements in the electroweak sector. The accelerators that have produced (or plan to produce) the highest tau pair yields are listed in table 1.1. Other e^+e^- colliders

working at lower center of mass energies, like IHEP and BINP, are expected to produce much lower statistics. Although they can run at the tau production threshold, with some advantage on systematics, especially on the τ -mass measurement.

1.2.1 Tau Lepton Flavor Violating decays

While gauge invariance is a fundamental requirement of the SM Lagrangian, the lepton family number conservation appears as an accidental symmetry. The experimental observation of neutrino oscillations opens to the possibility of observing a violation of the lepton family number for charged leptons as well. In the tau sector various charged Lepton Flavor Violating (LFV) decays can be searched for at collider experiments.

Given the parameters of the PMNS mixing matrix and the limits on neutrino masses, the expected branching ratio for the LFV decay $\tau \rightarrow \mu\gamma$ happening through a W loop is $< 10^{-53}$. However, many of the predicted beyond SM theories could explicitly break lepton flavor symmetry, in that case an higher branching ratio would be observed experimentally.

With 50 ab^{-1} integrated luminosity, Belle II is expected to set branching ratio upper limits of 10^{-9} for $\tau \rightarrow \mu\gamma$ decays and 10^{-10} for $\tau \rightarrow \mu\mu\mu$, therefore extending of about two order of magnitude the results from previous generation B-factories (see Figure 1.2).

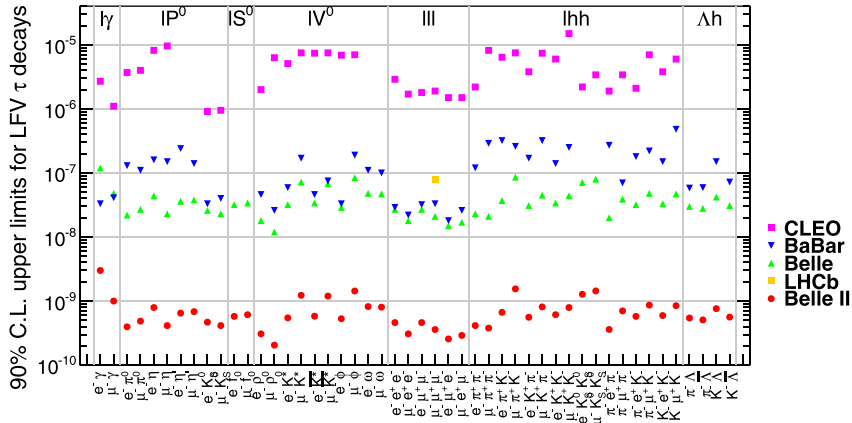


Figure 1.2: Upper limits at 90% confidence level of the τ LFV decays. Present limits are indicated, together with the extensions expected with the Belle II full statistics [5].

1.2.2 Lepton Flavor Universality

In the Standard Model, the presence of three fermion generations, distinguished only by the Yukawa interaction with the Higgs field, is yet to be explained. In particular, the electroweak gauge couplings are considered to be the same for all the three families. This symmetry enters the SM without any clear motivation and therefore needs to

be deeper investigate experimentally. A deviation from universal couplings would represent an evidence of physics beyond the SM.

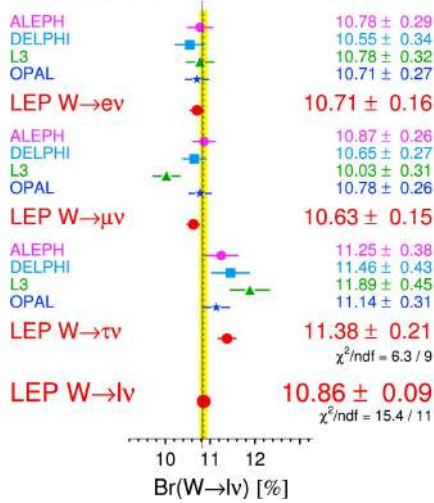
Such principle can be tested with high precision in the charged lepton sector studying the coupling of e , μ and τ with W and Z bosons. To date, no relevant violation of the lepton universality (LU) has been observed for electron and muon couplings. Regarding the tau sector, however, precise measurements seem to suggest possible violation. The principal experimental tests to τ -lepton universality come from

- Measurements of W -boson partial widths.
- Branching fractions comparisons of B decaying semileptonically.
- Precise measurements of τ -lepton properties.

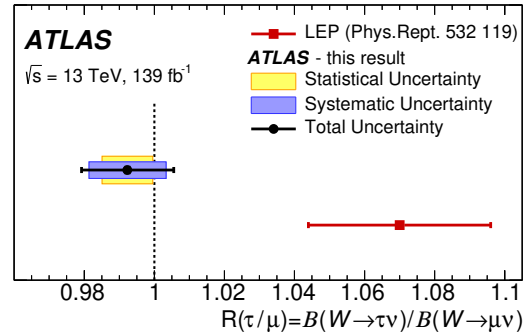
In the following the status of this tests is outlined.

W boson branching ratio

W Leptonic Branching Ratios



(a) W leptonic branching fractions measured at LEP.



(b) Results from ATLAS, using the top-antitop production.

Figure 1.3: Results for LU tests from the W boson leptonic branching fractions. At LEP (a) a 2.6σ excess in the decay $W \rightarrow \tau\nu$ respect to e and μ channels, was observed. However, ATLAS recently found the branching fraction $\mathcal{B}(W \rightarrow \tau\nu)/\mathcal{B}(W \rightarrow \mu\nu)$ to be compatible with unity.

Direct experimental tests of lepton flavor universality were carried on at the Large Electron Positron collider (LEP), where on-shell W -pairs were directly produced at center of mass energies above 160 GeV. The W boson partial widths measured at

LEP [6] show small excess of the branching fraction into τ lepton with respect to e and μ (Figure 1.3a)

$$\frac{2 \mathcal{B}(W \rightarrow \tau \bar{\nu}_\tau)}{\mathcal{B}(W \rightarrow e \bar{\nu}_e) + \mathcal{B}(W \rightarrow \mu \bar{\nu}_\mu)} = 1.066 \pm 0.025$$

with a deviation of 2.6 standard deviations from unity (the different phase space contribution is negligible). Although there is no statistical evidence, this result seems to suggest a possible violation of the LU assumed in the SM.

A recent study by ATLAS [7], exploiting the top and anti-top quark pair events produced at LHC, measured the ratio of the W branching fraction to τ with respect to μ , finding

$$\frac{\mathcal{B}(W \rightarrow \tau \bar{\nu}_\tau)}{\mathcal{B}(W \rightarrow \mu \bar{\nu}_\mu)} = 0.992 \pm 0.013$$

which is in agreement with SM expectation but differs from the LEP measurement $\mathcal{B}(W \rightarrow \tau \bar{\nu}_\tau)/\mathcal{B}(W \rightarrow \mu \bar{\nu}_\mu) = 1.070 \pm 0.026$ (see Figure 1.3b).

Semileptonic B decays

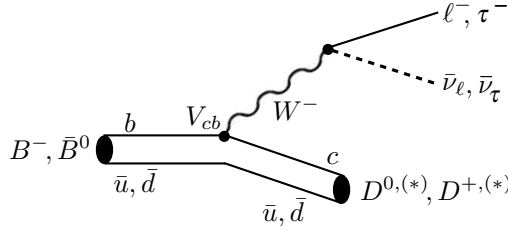


Figure 1.4: Diagram of the decay with $b \rightarrow c$ transition with a charged lepton $\ell = e, \mu$ or a τ in the final state. The measured branching ratios enter the $R(D)$ and $R(D^*)$, used to test LU.

BaBar, Belle and LHCb have independently found some additional hints to a possible LU violation studying leptonic and semileptonic decays of B mesons [8].

B leptonic and semileptonic decays are well understood in SM. A lepton universality test can be performed on the quantity $R(D^{(*)})$, defined as the ratio of branching fractions $\bar{B} \rightarrow D^{(*)} \tau^- \bar{\nu}_\tau$ and $\bar{B} \rightarrow D^{(*)} \ell^- \bar{\nu}_\ell$

$$R(D) = \frac{\mathcal{B}(\bar{B} \rightarrow D \tau^- \bar{\nu}_\tau)}{\mathcal{B}(\bar{B} \rightarrow D \ell^- \bar{\nu}_\ell)} \quad R(D^*) = \frac{\mathcal{B}(\bar{B} \rightarrow D^* \tau^- \bar{\nu}_\tau)}{\mathcal{B}(\bar{B} \rightarrow D^* \ell^- \bar{\nu}_\ell)}$$

where ℓ is an electron or a muon. The diagram of these decays is shown in Figure 1.4. The main advantage of considering $R(D)$ and $R(D^*)$ is to reduce the uncertainty coming from the knowledge of the decay form-factors. The most recent SM theoretical predictions averages, proposed by the Heavy Flavor Averaging Group (HFLAV) [9], are

$$R(D)^{\text{SM}} = 0.300 \pm 0.003 \quad R(D^*)^{\text{SM}} = 0.258 \pm 0.005$$

The combined results from Belle, Babar and LHCb are (Figure 1.5):

$$R(D) = 0.340 \pm 0.027 \pm 0.013 \quad R(D^*) = 0.295 \pm 0.011 \pm 0.008$$

where the first error is statistical and the second one is systematic. The excess respect to the SM are 1.4σ for $R(D)$ and 3.4σ for $R(D^*)$

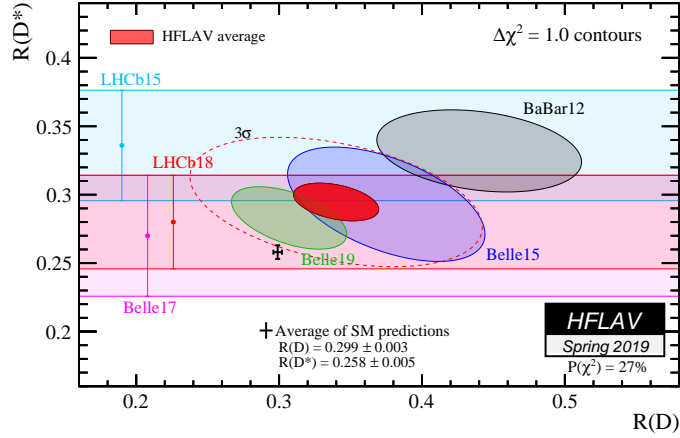


Figure 1.5: Status of $R(D)$ and $R(D^*)$ measurements. The red ellipse represents the world average, including both the separate measurements of $R(D^*)$ and results from simultaneous measurements of $R(D)$ and $R(D^*)$. The black point with error bars indicates the average of SM calculations. Plot from HFLAV 2019 [9].

τ -lepton decay

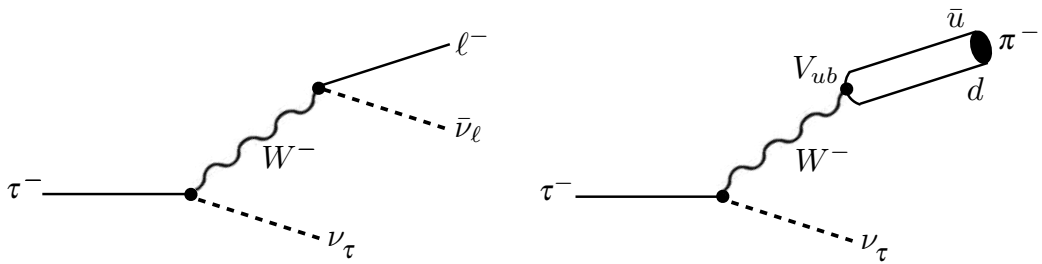


Figure 1.6: Feynman diagrams to the tree level of leptonic (left) and hadronic (right) τ -lepton decays. In SM, the amplitude of τ can be computed with high precision.

The universal coupling of W boson to leptons can be tested also from the decays of leptons itself. In general, considering a lepton λ decaying into a lighter lepton ρ ,

the width can be expressed like

$$\Gamma(\lambda \rightarrow \rho \bar{\nu}_\rho \nu_\lambda) = \frac{\mathcal{B}(\lambda \rightarrow \rho \bar{\nu}_\rho \nu_\lambda)}{\tau_\lambda} = \frac{G_\lambda G_\rho m_\lambda^5}{192\pi^3} f\left(\frac{m_\rho^2}{m_\lambda^2}\right) R_\gamma^\lambda R_W^\lambda \quad (1.4)$$

where

$$G_i = \frac{g_i^2}{4\sqrt{2}M_W^2}$$

is the Fermi coupling constant, while $f(x)$ and $R_{\gamma,W}^\lambda$ account respectively for phase-space and radiative corrections.

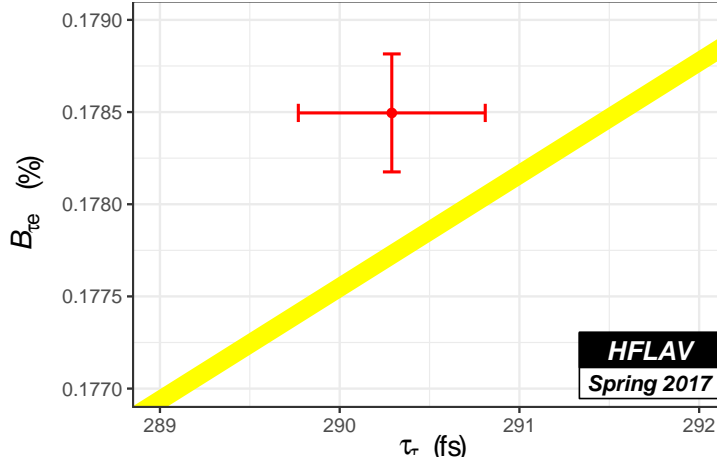


Figure 1.7: Present experimental values for τ -lepton lifetime and branching fraction $\mathcal{B}(\tau \rightarrow e \bar{\nu}_e \nu_\tau)$ [10]. The yellow band indicates the SM prediction given by (1.5) assuming LU ($g_\tau = g_e = g_\mu$), where the band-width is given by the τ mass uncertainty.

From (1.4), a test of $\tau - \mu$ and $\tau - e$ LU can be done using measured lepton masses, lifetimes and branching fractions. Exploiting relation (1.4) and using the averaged experimental values from PDG 2020 [11], we find the coupling constant ratios

$$\frac{g_\tau}{g_e} = 1.0029 \pm 0.0014 \quad \frac{g_\tau}{g_\mu} = 1.0010 \pm 0.0014$$

At present, both quantities are compatible with unity, where the uncertainty is dominated by τ lifetime and leptonic branching fractions. In figure 1.7, the present values for τ lifetime and $\mathcal{B}(\tau \rightarrow e \bar{\nu}_e \nu_\tau)$ are compared with the SM prediction assuming LU:

$$\mathcal{B}^{\text{SM}}(\tau \rightarrow e \bar{\nu}_e \nu_\tau) = \frac{\mathcal{B}(\mu \rightarrow e \bar{\nu}_e \nu_\mu)}{\tau_\mu/\tau_\tau} \frac{m_\tau^5}{m_\mu^5} \frac{f(m_e^2/m_\tau^2)}{f(m_e^2/m_\mu^2)} \frac{R_\gamma^\tau R_W^\tau}{R_\gamma^\mu R_W^\mu} \quad (1.5)$$

The discrepancy is not statistically significant, therefore improving the precision on τ_τ is necessary to directly prove LU within the SM, or finding out possible new physics contributions.

So far the most precise τ -lepton lifetime measurement was performed by the Belle experiment [12]

$$\tau_\tau = (290.17 \pm 0.53(\text{stat}) \pm 0.33(\text{syst})) \text{ fs}$$

The experimental error is expected to be further reduced by Belle II, which can count on much higher statistic and a upgraded detector.

Chapter 2

The Belle II experiment

The Belle II Experiment collects data at the new generation B-factory SuperKEKB, located at the High Energy Accelerator Research Organization (KEK) in Tsukuba, Japan. Belle II aims to perform the most precise Standard Model measurements in the electroweak and heavy flavor sector, searching for possible indications of new physics. It follows the path of the predecessor experiments BaBar and Belle, which observed for the first time CP-violation in the B mesons, and exploiting the high luminosity design of SuperKEKB, it plans to collect the record integrated luminosity of 50 ab^{-1} , corresponding to about 5×10^{10} tau pairs.

In this chapter the main features of the SuperKEKB collider and the Belle II detector are briefly outlined.

2.1 SuperKEKB

SuperKEKB is a 3 km length double ring electron-positron collider working mainly at the $\Upsilon(4S)$ center of mass energy ($\sqrt{s} = m_{\Upsilon(4S)} = 10.58 \text{ GeV}$). Electron and positron beams circulate in opposite directions in two adjacent storage rings, respectively called High Energy Ring (HER) and Low Energy Ring (LER). Belle II detector is located in their only intersection point [13]. Electrons and positrons are accelerated to their nominal energy by the Linear Accelerator (LINAC) and injected into bunches in the main rings. The positron emittance is reduced in a 1.1 GeV Damping Ring. Figure 2.1 shows the schematic view of the SuperKEKB facility.

The SuperKEKB accelerator is an upgrade of the previous generation B -factory KEKB, which, competing with PEP II at SLAC, achieved the instantaneous luminosity record of $2.11 \times 10^{34} \text{ cm}^{-2} \text{ s}^{-1}$. SuperKEKB is designed¹ to reach an instantaneous luminosity 40 times larger than its predecessor.

Since $B\bar{B}$ mesons are produced almost at rest in the $\Upsilon(4S)$ frame ($p_B^{\text{cms}} \simeq 330 \text{ MeV}$), for precise measurements of time-dependent CP-violation in B decays the

¹The designed luminosity is $8 \times 10^{35} \text{ cm}^{-2} \text{ s}^{-1}$, however, in the upgraded road-map, the target luminosity is changed to $6 \times 10^{35} \text{ cm}^{-2} \text{ s}^{-1}$.

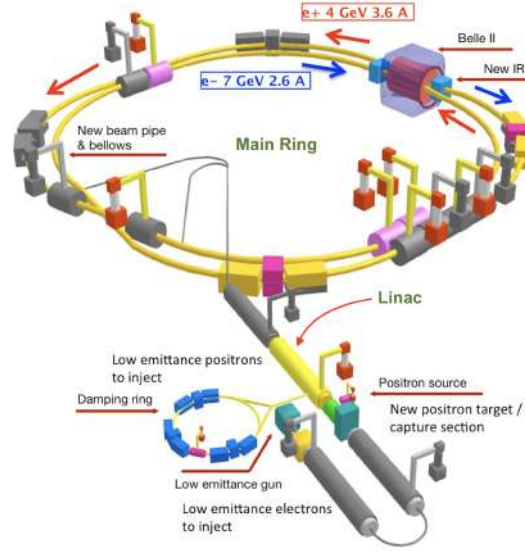


Figure 2.1: Schematic view of the SuperKEKB accelerator complex located at the High Energy Accelerator Research Organisation (KEK) in Tsukuba, Japan. Electron and positron beams are accelerated in the LINAC and injected into two circular storage rings, so that they circulate in opposite direction. A Damping Ring was built to reduce the positron emittance, as required for the nano-beam collision scheme.

center of mass needs to be boosted in the laboratory. The boost is obtained using asymmetric beam energies E_{e+} , E_{e-} that must satisfy

$$4E_{e+}E_{e-} = m_{\Upsilon(4S)}^2$$

neglecting electron mass. The desired boost factor is given by

$$\beta\gamma \simeq \frac{E_{e-} - E_{e+}}{m_{\Upsilon(4S)}}$$

At SuperKEKB $E_{e+} = 4 \text{ GeV}$ and $E_{e-} = 7 \text{ GeV}$, resulting in $\beta\gamma \simeq 0.28$ and a B mean decay length $\lambda_B \approx 130 \mu\text{m}$. Regarding τ -lepton pairs, as in the center of mass they are produced with a momentum $p_\tau \simeq 5 \text{ GeV}$, their mean decay path $\lambda_\tau \approx 250 \mu\text{m}$ is not significantly affected by the boost. Anyway, tau physics can benefit from a smaller $\beta\gamma$ since the tau pair is better separated in the laboratory. The center of mass boost is about two-third of what experienced in KEKB and half of the boost at PEP II, thus requiring a better vertex resolution. The symmetry reduction with respect to the predecessors is necessary to limit beam emittance and develop the high-luminosity scheme.

2.1.1 Nano-beam scheme

The luminosity upgrade of the KEKB facility to SuperKEKB is based on the nano-beam collision scheme developed for the SuperB project [14].

For an electron-positron collider, the instantaneous luminosity can be expressed like [15]

$$\mathcal{L} = \frac{\gamma_{e^\pm}}{2er_e} \left(1 + \frac{\sigma_y^*}{\sigma_x^*}\right) \left(\frac{I_{e^\pm} \cdot \xi_{y,e^\pm}}{\beta_y^*}\right) \left(\frac{R_L}{R_{\xi_y}}\right) \quad (2.1)$$

γ is the Lorentz factor for the colliding e^\pm , r_e is the classical electron radius, σ_x^* and σ_y^* are the horizontal and vertical beam sizes at the interaction point (IP), assumed to be equal for electron and positron. I_{e^\pm} are the beam currents and β is the function describing the amplitude of betatron oscillations in the transverse plane while β_y^* is its restriction on the y direction calculated at the IP. ξ_y is the vertical beam-beam tune shift, accounting for resonances due to bunch crossing. The main parameters to optimize for achieve high luminosity are β_y^* , I_\pm , and ξ_y .

At SuperKEKB, two Super Conducting Quadrupol magnets are placed before and after the interaction point in order to squeeze β_y^* by approximately a factor 20: from 5.9 mm obtained at KEKB to the designed value $\beta_y^* = 0.3$ mm. At the same time the beam currents I_{e^\pm} are doubled, thus leading to an expected increase in instantaneous luminosity by a factor ≈ 40 with respect to KEKB.

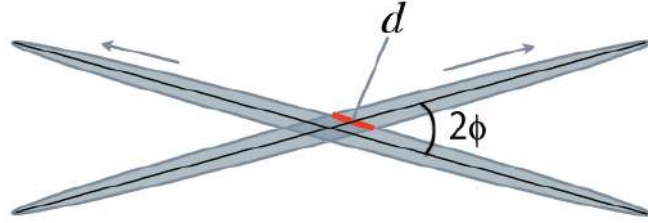


Figure 2.2: Principle of the nano-beam collision scheme. The two bunches overlap with an half-crossing angle ϕ , hence the effective beam length is $d \simeq \sigma_x^*/\phi$. With this scheme the luminosity can be increased limiting the hourglass effect.

The value of β function increases quadratically moving away from the interaction point, therefore long bunches are actually less focused than what predicted by the β^* entering expression (2.1). This effect, known as hourglass effect, lowers the expected instantaneous luminosity. To avoid it, the longitudinal beam size should be kept smaller than β_y^* . Within nano-beam scheme, such condition is fulfilled making the two beams collide with an incident angle ϕ . In this way the actual beam length d relevant for the hourglass effect is determined by the overlapping region, which, as clear from Figure 2.2, is

$$d = \frac{2\sigma_x^*}{\sin 2\phi} \simeq \frac{\sigma_x^*}{\phi}$$

thus the requirement becomes:

$$d < \beta_y^* \quad \longrightarrow \quad \frac{\sigma_x^*}{\phi} < \beta_y^*$$

In table 2.1 some nominal parameter of SuperKEKB collider are reported.

Table 2.1: Nominal accelerator values for High Energy Ring (HER) and Low Energy Ring (LER) at SuperKEKB.

	LER	HER
Beam energy [GeV]	4.007	7.000
Beam current [A]	3.60	2.60
Crossing angle ϕ [mrad]		41.5
Bunch number		2500
Particles per bunch	9.04×10^{10}	6.53×10^{10}
β_y^* [mm]	0.30	0.27
Horizontal beam size σ_x^* [μm]	10.1	10.7
Vertical beam size σ_y^* [nm]	48	62
Beam-beam parameter ξ_y	0.088	0.081
Luminosity \mathcal{L} [$\text{cm}^{-2}\text{s}^{-1}$]		8×10^{35}

2.2 Belle II detector

The Belle II detector [15], situated at the HER and LER beams interaction point (IP), is designed to take data in a high luminosity environment. As a result of the increased beam focusing and currents in SuperKEKB, the beam background is expected to be up to 30 times larger with respect to Belle and therefore some improvements are needed to maintain comparable or better performances.

The Cartesian right-handed system of coordinates of Belle II is defined with the z axis forming the same angle ϕ with the two nominal beams directions, such that in the center of mass it comes to point towards the HER direction. The transverse plane is defined by the x axis lying on the machine plane and pointing towards the center, and the y axis pointing upwards. θ is the polar angle respect to the positive z direction and φ the azimuthal angle in the transverse plane.

The Belle II detector is characterized by high hermeticity, with a full coverage in the azimuthal angle φ and an asymmetric acceptance in the polar angle $17^\circ < \theta < 150^\circ$. Considering the forward boost, the acceptance becomes almost symmetric in the center of mass system $21^\circ < \theta^{\text{cms}} < 156^\circ$.

A superconducting magnet generates a uniform solenoidal magnetic field of 1.5 T in the central part of the detector. For precise momentum measurement the magnetic field must be carefully mapped taking into account contributions from the focusing superconducting quadrupoles.

Figure 2.3 shows a cross section on the x - z plane of the full detector. The tracking system, composed of a silicon vertex detector (VXD) and a gaseous drift chamber (CDC), measures charged particles momenta and reconstructs production and decay vertexes. Photons and electrons are then stopped making them showering in a homogeneous electromagnetic calorimeter (ECL). Muons are discriminated in the outermost subdetector, which exploits the iron return yoke of the magnetic field to

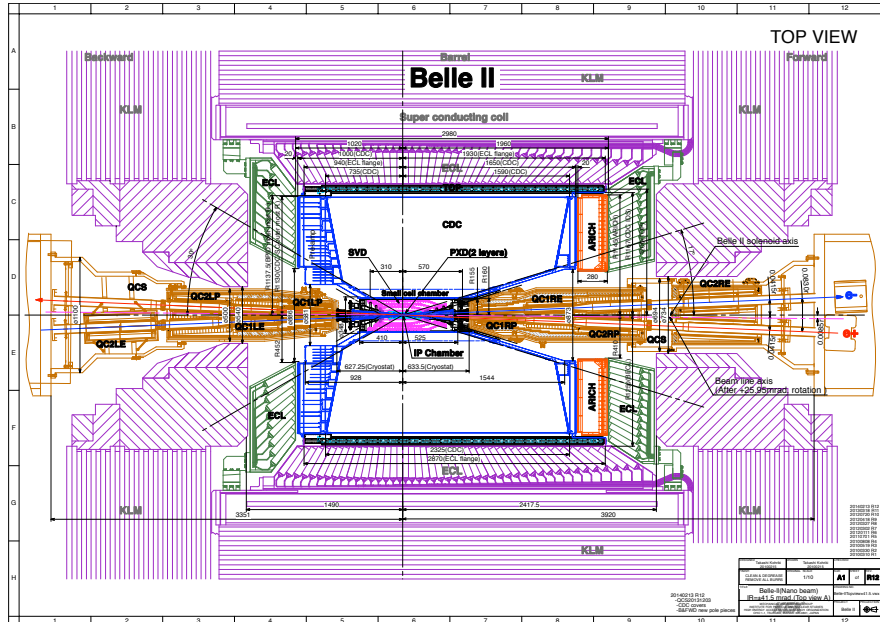


Figure 2.3: Cross section view in the x - z plane of the full Belle II detector. All the subdetectors are labeled. The superconducting quadrupoles (QCS) are placed along the beam line on the two sides.

detect long lived neutral hadrons. A non-destructive Cherenkov imaging particle identification detector (PID) is placed between CDC and ECL.

In the following, starting from the center and going outward, each subdetector is briefly described.

2.2.1 Vertex Detector

The Belle II innermost detector, located just outside the Beryllium beam pipe and surrounding the IP, is a 6-layers cylindrical vertex detector (VXD) composed of a inner pixel detector and an outer silicon strip detector. The VXD task is to measure with high precision charged particles tracks, impact parameters and reconstruct decay vertexes of B -mesons, D -mesons, τ -leptons and K_S^0 .

In order to improve vertex reconstruction in comparison to Belle, the first VXD layer is placed closer to the IP halving the beam pipe radius to 10 mm. At the same time the VXD external radius is increased from 60.5 mm to 135 mm.

Pixel Detector

At high luminosity the detector layers closest to the interaction region face an elevated hit rate due to beam background and low momentum QED processes. Hence, to limit channel occupancy, the two inner layers of VXD placed at $r = 14$ mm and $r = 22$ mm are a DEPFET (DEPLETED Field Effect Transistor) Pixel Detector (PXD).

A rendering of the PXD layers is shown in Figure 2.4. In the DEPFET technology the readout and the cooling system can be placed away from the $50\ \mu\text{m}$ -thick active sensors, thus minimizing the material budget responsible for multiple scattering.



Figure 2.4: View of the two-layers DEPFET Pixel Detector.

Silicon Vertex Detector

The remaining 4 layers are based on $320\ \mu\text{m}$ thick double sided silicon strip detectors (SVD) placed at 39 mm, 80 mm, 104 mm, and 135 mm distance from z axis. For the sensors of the inner layer (L3), strips on n -side are along the z direction with a $50\ \mu\text{m}$ pitch, while on the p -side strips are oriented on $r\varphi$ and have a $160\ \mu\text{m}$ pitch. For the other layers (L4, L5 and L6) the pitches increase to $75\ \mu\text{m}$ on the p -side and $240\ \mu\text{m}$ on the n -side. To reduce the number of wafers, in the forward region the 3 external layers use trapezoidal slanted sensors $300\ \mu\text{m}$ thick (see Figure 2.5). The total material budget of each layer is about 0.7% radiation lengths. The readout electronics is implemented using the APV25 amplifier chip having a shaping time of $50\ \text{ns}$.

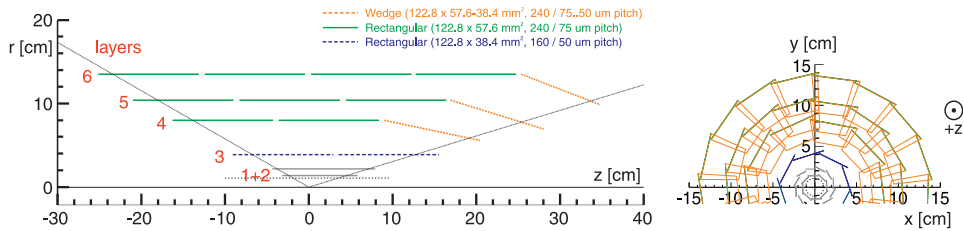


Figure 2.5: Schematic longitudinal (left) and transverse (right) view of the SVD layers. Note the geometrical arrangement of the slanted sensors in the 3 outermost layers.

2.2.2 Central Drift Chamber

The tracking system is completed by the Central multi-wire Drift Chamber (CDC). This subdetector, besides tracking, provides also particle identification information

measuring the dE/dx energy loss for tracks not reaching the PID detector ($p_t \lesssim 500$ MeV) and has an important role for the first level trigger as well. CDC is filled with a gas mixture of He (50%) and C_2H_6 (50%) having a drift velocity of 4 cm/ μ s. Wires are arranged in drift cells grouped radially on 56 layers alternating axial layers, with wires directed along z , and stereo layers, with skewed wires, making possible a 3D track reconstruction. Each cell is defined as one sense wire surrounded by 8 field wires. In total 14336 Tungsten sens wires and 42240 Aluminum field wires are present, respectively of diameter 30 μ m and 126 μ m.

In comparison to Belle, a better momentum resolution is obtained through a larger external radius (113 cm instead of 88 cm) and smaller drift cells make possible to operate under higher event rate.

2.2.3 Particle Identification Detector

The Particle Identification Detector (PID) is deputed mainly to discriminate kaons, pions and protons in a wide energy range. A good K - π separation is of particular importance for tagging different B decay modes. PID use two distinct detectors depending on the acceptance region: the barrel is provided with a Time of Propagation counter while in the forward region the particle identification is guaranteed by a Ring Imaging Cherenkov Detector. Both work measuring the angle of the emitted light Cherenkov cone, which is sensible to the particle velocity.

Time of Propagation

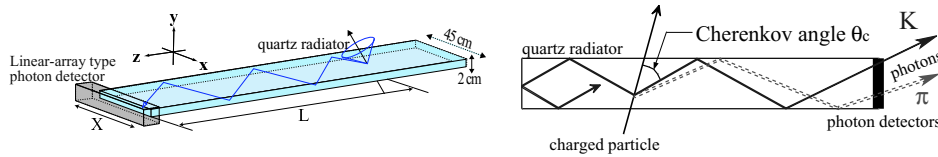


Figure 2.6: Scheme of the quartz bar used for the TOP detector. Cherenkov photons, subjected to total internal reflection, reach the photon detectors placed at one edge of the bar. The x , y positions and the time of arrival of the photons are used to reconstruct the Cherenkov angle.

The Time of Propagation (TOP) counter consists of 2 cm thick quartz bars. The Cherenkov photons generated by the passage of a charged particle propagate through the bar via internal reflection and are collected at one edge (see Figure 2.6). Microchannel plate photomultipliers (MCP PMTs) measure position and time of arrival reconstructing the 3D Cherenkov image. A minimum of 100 ps time resolution is required for the photomultipliers, which on each edge are divided in a 4×4 array and must be sensible to the single photon.

The TOP is composed of 16 quartz modules 45 cm wide and 2.75 m long arranged to cover the full φ angle around the CDC external radius. The polar angle acceptance is $31^\circ < \theta < 128^\circ$.

ARICH

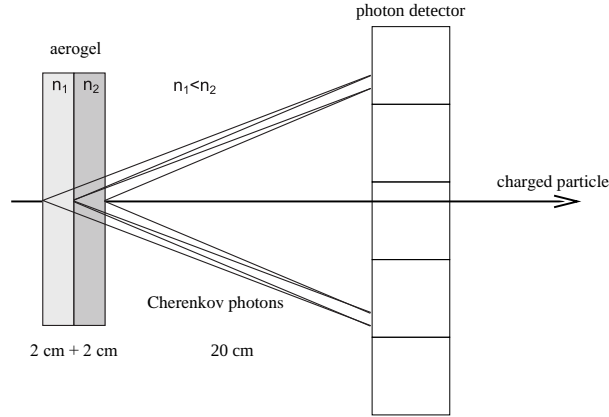


Figure 2.7: Operating principle of the ARICH detector. The charged particle crosses the non-homogeneous aerogel and the emitted Cherenkov photons are detected by the HAPDs, which reconstruct the Cherenkov ring.

In the forward endcap a proximity focusing aerogel Ring Imaging Cherenkov Detector (ARICH) is installed, covering the region $14^\circ < \theta < 30^\circ$. It is designed to provide a good photon separation in the momentum range from 400 MeV to 4 GeV. It consists of a 4 cm thick non-homogeneous aerogel Cherenkov radiator and an array of hybrid avalanche photon detectors (HAPD), separated by a 20 cm expansion gap. The operating principle of the ARICH is shown in Figure 2.7. The HAPD are sensible to the single photon position and estimate the Cherenkov angle reconstructing the full ring. In order to increase the Cherenkov photon yield maintaining a good angle resolution, the ARICH employs two materials with different refractive index $n_1 < n_2$ so that a focusing effect is obtained.

2.2.4 Electromagnetic Calorimeter

An electromagnetic calorimeter at Belle II should be able to detect photons in a broad spectrum with good energy resolution, and also to discriminate electrons from charged hadrons.

Table 2.2: Polar angle coverage of the ECL.

Forward endcap	$12.01^\circ < \theta < 31.36^\circ$
Barrel	$32.2^\circ < \theta < 128.7^\circ$
Backward endcap	$131.5^\circ < \theta < 155.03^\circ$

The Belle II Electromagnetic Calorimeter (ECL) is made by a total of 8736 CsI(Tl) crystals, approximately $(5 \times 5 \times 30)\text{cm}^3$ each, with the longitudinal dimension

corresponding to 16.2 radiation lengths. They are arranged in three sections, one covering the barrel and two placed at the endcaps. The acceptance of each section is reported in table 2.2, note that also for this detector the coverage is asymmetric. The scintillation light is read by two photodiodes attached on the rear face of each crystal and equipped with a waveform sampling readout, aiming to reduce secondary pulses from pile-up noise. The intrinsic energy resolution measured on a Belle prototype has been parametrized [16] as the quadratic sum:

$$\frac{\sigma_E}{E} = \frac{0.066\%}{E} \oplus \frac{0.81\%}{E^{1/4}} \oplus 1.34\%$$

where E is the photon energy in GeV and the first term comes from the electronic noise.

2.2.5 K_L and μ detector

The outermost detector identifies long lived particles that do not undergo electromagnetic showering and separate muons from charged hadrons (pions in particular).

The K_L and muon detector (KLM), located outside the ECL and the superconducting magnet, consists of a sandwich of active detectors and 4.7 cm thick iron, used as return yoke for the magnetic field. The total thickness is equivalent to about 3.9 interaction lengths, to be summed to the ≈ 0.8 interaction lengths of the ECL. K_L mesons are hence detected through hadronic showers which can start either from ECL or from KLM. Muons and non-showering charged hadrons cross the detector as minimum ionizing particles and are identified from the range information.

The KLM is divided in three sections, one for the barrel and two for the endcaps, covering a polar angle $20^\circ < \theta < 155^\circ$. The barrel are segmented into 14 and 12 active layers respectively. In the barrel the active detectors are glass-electrode resistive plate chambers (RPC), already utilized at Belle. However, the long RPC dead time make them not optimal for the Belle II endcaps, where a much higher background rate due to neutrons coming from the beam line is expected. Therefore, in the forward and backward sections and in the first 2 layers of the barrel, RPCs have been substituted by scintillator strips read out by Silicon photomultipliers.

2.3 Software and reconstruction

Aiming to collect 50 ab^{-1} of data, Belle II needs an efficient and reliable software for online and offline data handling. The Belle II software analysis framework (`basf2`) is implemented with processing blocks called *modules*, each executing a defined task. A sequence of modules makes up a *path*, hence, when a path is processed, the modules attached to it are executed in order. Different modules communicate sharing data and variables in a common object store.

`basf2` is responsible for Monte Carlo simulation of the physics processes and detector response, the reconstruction of physical high-level objects from raw datasets

and the analysis tools. The software version used throughout the present thesis is `release-04-02-08`.

2.3.1 Monte Carlo generators

An accurate simulation for particle production and decay is fundamental for precision measurements. Several Monte Carlo (MC) generators are included as `basf2` modules to simulate production and particle decays of all the relevant processes at the $\Upsilon(4S)$ energy.

The `PYTHIA` generator is used for continuum production and inclusive decays of light quarks, whereas some B and D mesons exclusive decay chains are handled by `EvtGen`. Bhabha events and other QED background processes such as two photons are generated by `BABAYAGA.NLO`. The production of tau pair events $e^+e^- \rightarrow \tau^+\tau^-(n\gamma)$ is simulated by the `KK2f` generator [17], included in the `KKMC` module. At $\sqrt{s} = 10.58$ GeV, it reproduces the production cross section with $\approx 0.4\%$ uncertainty [18]. `KK2f` simulates initial (ISR) and final state radiation (FSR) almost to next-to-next-to-leading order in QED and the interference of initial and final state radiation (IFI) at next-to-leading order. The beam parameters, including initial energy and primary vertex position, are provided to all the generators by a central database. Vertex position is smeared considering the HER and LER beam sizes and bunch length at the IP. Unlike `EvtGen` and `BABAYAGA.NLO`, `KK2f` does not include any beam energy smearing. Tau decays are then handled by the `TAUOLA` package, which also takes in account spin polarization effects.

The detector simulation is implemented in the `basf2` software by the `Geant4` package (version 10.1.2.) which simulates the interaction of long lived and secondary particles with the subdetectors. Other `basf2` modules are responsible for the subsequent hit digitization.

2.3.2 Tracking

Track objects are determined connecting the hits of charged particles in VXD and CDC detectors. At this aim a pattern recognition algorithm is exploited. In particular, for the VXD a cellular automaton model is used [19], while for the CDC a global track finder algorithm applying a Hough transformation [20] and a local track finder are combined. The true track candidates in VXD and CDC are finally merged together.

The coordinates of the POCA (point of closest approach to the origin of the coordinate system) and the momentum vector at the POCA are associated to every reconstructed track. The trajectory of a charged particle in a uniform magnetic field is described by a helix, defined by 5 independent parameters. The following parametrization is adopted for tracks at Belle II (see Figure 2.8):

- d_0 : the signed distance of the POCA respect to the origin in the transverse plane. The sign of d_0 depends on the sign of the vector product $\vec{d}_0 \times \vec{B}$, where \vec{B} is the magnetic field.

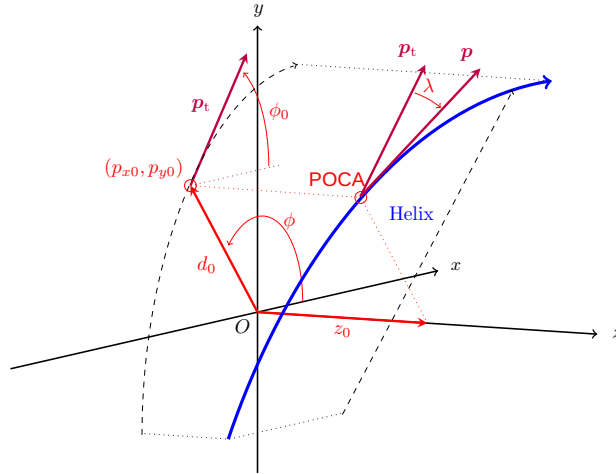


Figure 2.8: Scheme showing the tracking parameters used in the `basf2` software. The blue arrow represents the reconstructed helix. Credits: github.com/ndawe/tikz-track.

- z_0 : the z coordinate of the POCA.
- ϕ_0 : the angle between the transverse momentum p_t at the POCA and the x axis.
- $\tan \lambda$: λ is the angle between the momentum at the POCA and the transverse plane.
- ω : the curvature of the helix, with the sign given by the charge of the track.

The track expressed under such parametrization is then fitted using an algorithm based on a Kalman filter [21].

2.3.3 ECL clusters

The main task of the electromagnetic calorimeter is to detect photons and neutral hadrons with a good energy and position resolution. From a software point of view, physical objects are reconstructed in the calorimeter as clusters. A cluster is built summing up the energy deposits in contiguous ECL crystals. To decide which crystals to include in a cluster, a cluster reconstruction algorithm is used.

Firstly, connected regions are formed starting from a crystal with an energy deposit above 10 MeV and including the neighboring crystals with energy deposit over a background threshold. Connected regions sharing crystals are merged. Clusters are then formed starting from seed crystals having a local maximum energy deposit and adding iteratively the other crystals of the connected region. The energy of the i -crystal is assigned to the cluster with a weight

$$w_i = \frac{E_i e^{-Cd_i}}{\sum_k E_k e^{-Cd_k}}$$

where C is a constant and the index k runs over all the crystals in the cluster. E_i is the energy deposited in the i -crystal and d_i is the distance from its geometric center \vec{x}_i to the cluster's centroid \vec{x} , defined as

$$\vec{x} = \frac{\sum_i w'_i \vec{x}_i}{\sum_i w'_i} \quad \text{with} \quad w'_i = 4.0 + \log \left(w_i + \frac{E_i}{E_{\text{all}}} \right)$$

E_{all} is the sum of all the weighted energies in the cluster. The iteration terminates when the centroid positions of all clusters in the connected region are stable within 1 mm.

2.3.4 Vertex Fitter

The `TreeFitter` is the standard `basf2` module for fitting a whole particle decay chain [22]. Regarding tau-physics analysis it can be used for finding the vertex of the 3-prong decay $\tau \rightarrow \pi\pi\pi\nu$.

`TreeFitter` performs a progressive fit of the full decay chain. The parameters entering the fit are:

- the momentum vectors of each particle in the decay tree. For final state particles the energy E is given by the mass hypothesis constrain while for the mother particles it is assigned as an additional free parameter. Otherwise, if the mass of the mother is well defined, it can be added as a mass constrain. This is not possible for tau decays because of the missing neutrinos.
- 3 more parameters are assigned as the decay vertex position for every mother particle in the chain.

The whole system is optimized with a χ^2 -like minimization using a Kalman filter based approach [21].

2.4 Operations and future plans

At Belle II, first electron-positron collisions started in April 2018. On 15th June 2020, SuperKEKB achieved the world's highest instantaneous luminosity for a colliding-beam accelerator, equal to $2.22 \cdot 10^{34} \text{cm}^{-2}\text{s}^{-1}$, exceeding the previous record of $2.14 \cdot 10^{34} \text{cm}^{-2}\text{s}^{-1}$ detained by the Large Hadron Collider. The current record is set to $2.40 \cdot 10^{34} \text{cm}^{-2}\text{s}^{-1}$, obtained on June 21st 2020. The plot in Figure 2.9 shows the instantaneous luminosity during the last year of operations.

Regarding the integrated luminosity, considering the data acquired with the full detector installed (Phase III), about 74fb^{-1} of statistics have been recorded during 2019 and and first part of 2020 runs (see Figure 2.10a). By the end of 2021 the full data set is expected to be comparable with the statistics collected by the Belle experiment. An interruption in data taking is programmed between 2021 and 2022 in order to upgrade the PXD detector.

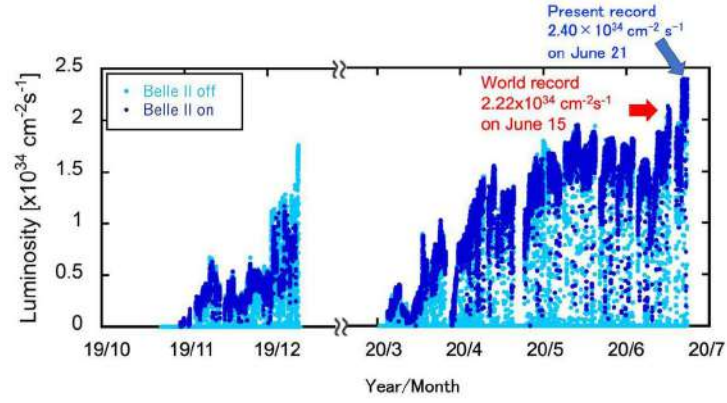
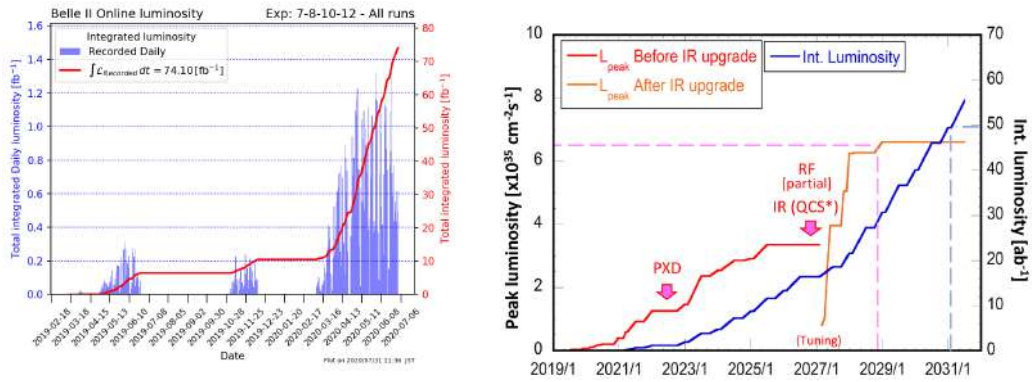


Figure 2.9: Instantaneous luminosity delivered by the SuperKEKB collider during the operations of end 2019 and beginning 2020. SuperKEKB now detains the luminosity record for a collider.

The long term plan, depicted in Figure 2.10b, foresees to further improve luminosity performances installing the new superconducting final focusing magnets (QCS), which should permit to squeeze β_y^* to 0.3 mm. In that case the peak instantaneous luminosity should reach the target value corresponding to $6 \times 10^{35} \text{cm}^{-2} \text{s}^{-1}$. Assuming 8 months of operation per year, the present expectation is to achieve the target $\approx 50 \text{ab}^{-1}$ integrated luminosity by 2030.



(a) Daily integrated luminosity for Phase III, Run 2019 (a,b,c) and Run 2020 (a-b). (b) Luminosity roadmap for Belle II operations during next decade.

Figure 2.10: Belle II already recorded about 74 fb^{-1} of integrated luminosity, and, by ~ 2030 , plans to collect the unprecedented value of 50 ab^{-1} .

Chapter 3

τ lifetime reconstruction method

In this chapter the method for reconstructing the τ -lepton lifetime in tau pair events is presented. Section 3.2 contains an overview of the most precise tau lifetime measurements performed during the last 25 years, all exploiting the tau pairs produced in the clean environment of a e^+e^- collider. The new method, here proposed for the Belle II experiment, puts together various techniques borrowed from previous measurements. It is described in details along section 3.3. Essentially, it is composed of two parts. The first, characterized in section 3.3.1, consists of a reconstruction of the full event kinematic, thus included the four momenta of taus and neutrinos. The second part (section 3.3.2), regards the reconstruction of decay lengths and primary vertex coordinates using impact parameters and fitted secondary vertexes. These two are eventually merged in a unique reconstruction method, as presented in 3.3.3. Finally, in section 3.4, the proposed method is tested on a pure tau pair 1-prong \times 3-prong MC signal sample.

3.1 Lifetime measurement

The decay of unstable particles is characterized by the lifetime parameter τ , whose inverse $\Gamma = 1/\tau$ represents the probability, per unit of time, for a particle to decay. This leads to an exponential dependence of the particle population $N(t)$:

$$\Delta N = N(t + \Delta t) - N(t) = -\frac{N(t)}{\tau} \Delta t$$

and for $\Delta t \rightarrow 0$

$$\frac{dN}{dt} = -\frac{N(t)}{\tau} \quad \Longrightarrow \quad N(t) = N(0) e^{-\frac{t}{\tau}}$$

Experimentally, for short-lived particles, proper time t is measured from the particle velocity βc and from the decay length $\ell = |\vec{x}_d - \vec{x}_p|$, where \vec{x}_d and \vec{x}_p are respectively the decay and the production vertex positions in the laboratory frame.

Taking into account the Lorentz factor $\gamma = 1/\sqrt{1 - \beta^2} = E/m$, it is

$$t = \frac{\ell}{\beta\gamma c} = \frac{m}{|\vec{p}|} \ell$$

Therefore the particle momentum needs to be reconstructed as well. The τ -lepton decays through charged current interaction, with a neutrino ν_τ in the final state, whose momentum is not measured by the detector. This means that the τ momentum is not directly reconstructed as the sum of the momenta of the final states, making the measurement of the τ lifetime particularly challenging.

The measured proper time distribution $\mathcal{F}(t)$ is the convolution of an exponential distribution with the normalized resolution function $\mathcal{R}(t - t_{\text{true}}; \vec{\xi})$

$$\mathcal{F}(t; \tau, \vec{\xi}) = \frac{1}{\tau} e^{-\frac{t_{\text{true}}}{\tau}} * \mathcal{R}(t - t_{\text{true}}; \vec{\xi}) = \int_0^\infty \frac{1}{\tau} e^{-\frac{t_{\text{true}}}{\tau}} \mathcal{R}(t - t_{\text{true}}; \vec{\xi}) dt_{\text{true}} \quad (3.1)$$

$\vec{\xi}$ is an array of parameters defining the resolution function. In some cases they can be in turn functions of t_{true} .

3.2 Previous methods

The τ -lepton lifetime measurement requires a precise measurement of the production and decay vertexes. Hence, direct measurements were not possible before the introduction of the Silicon vertex detector technology. At present, all the measurements are performed at electron-positron collider, where τ -leptons are produced in pairs through the process $e^+e^- \rightarrow \tau^+\tau^-$. Usually both taus are used for the lifetime determination. Tau decay modes are generally classified as N -prong, depending on the number N of final state charged particles. 1-prong and 3-prong are the modes considered in most of tau physics analysis, and, for lifetime measurement, both decays can be exploited.

In this section, the state of the art of previously used methods is briefly reviewed. Further details can be found on the cited references.

3.2.1 LEP

At the Large Electron-Positron collider (LEP), operating at the center of mass energy around the Z^0 boson mass-peak, τ -leptons were produced in pairs through the electro-weak process $e^+e^- \rightarrow Z^0 \rightarrow \tau^+\tau^-$. One of the advantages, with respect to B -factories, is that the mean decay length for τ -leptons produced at the Z^0 peak is $\lambda_\tau = \beta\gamma c\tau_\tau \simeq 2.2$ mm. Furthermore, being the collider symmetric, the tau energy in the laboratory frame is known, except for initial and final state radiations (ISR, FSR). The effects of ISR and FSR, together with the background contaminations, are subtracted using Monte Carlo simulations.

In the following, we briefly describe the tau lifetime measurements performed at the four main LEP experiments, i.e. OPAL, ALEPH, L3 and DELPHI.

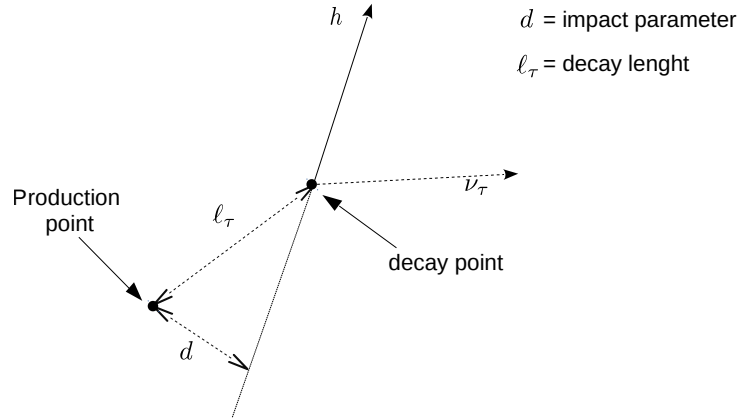


Figure 3.1: Scheme not in scale showing the relevant quantities for the proper time reconstruction in a τ decay. The decay length ℓ_τ is the distance from the τ -lepton production point and its decay point, whose position can be reconstructed only for 3-prong decays. Otherwise, the information on ℓ_τ is extrapolated from the impact parameter d of a final state track.

OPAL

The OPAL experiment used two distinct methods [23]:

- *Impact parameter method.* The decay length is estimated from the 1-prong impact parameter d , defined as the signed distance of closest approach to the interaction point in the transverse plane (see Figure 3.1). The mean value \bar{d} of the d distribution is computed for data and MC excluding the upper and lower 5% tails. The lifetime value on data is then estimated as

$$\tau_{\text{data}} = \frac{\bar{d}_{\text{data}}}{\bar{d}_{\text{MC}}} \tau_{\text{MC}}$$

- *Decay length method.* The tau decay vertex position is fitted from 3-prong tracks, while the nominal beam spot position is assumed as the τ production point. The distance of the two points is fitted to determine the average decay length, which is finally converted to a lifetime dividing by the Lorentz factor $\beta\gamma c$, assumed to be the same for all events.

In both methods, the final statistical uncertainty depends on the beam spot position and size.

ALEPH

Three different methods on the same data sample [24]. Two methods exploit the 1-prong \times 1-prong topology:

- *Momentum dependent impact parameter sum method.* The τ lifetime is extracted from a maximum likelihood fit of the (signed) impact parameters sum distribution $\delta = d_+ + d_-$ of 1-prong tracks.
- *Impact parameter difference method.* The expected value of the transverse impact parameter difference $d_+ - d_-$ can be written like

$$\langle d_+ - d_- \rangle = \frac{p_\tau}{m_\tau} \tau_\tau \Delta\varphi \sin \theta_\tau$$

where $\Delta\varphi$ is the difference in azimuthal angle of the two tracks. θ_τ is the polar angle of the τ direction, approximated to the thrust axis, defined as the direction \hat{n} which maximizes

$$\frac{\sum_i |\vec{p}_i \cdot \hat{n}|}{\sum_i |\vec{p}_i|}$$

where the sum runs over the momenta of all the particles in the event.

The third method uses tau decaying into 3-prong:

- *Decay length method.* The tau decay length is estimated from a least-squares fit where the IP and 3-prong vertex position are let as free parameters. As an estimate of the tau direction, the thrust axis is taken. The mean tau decay length is finally extracted through a maximum likelihood fit of the decay length distribution, using as probability density function the convolution of an exponential with a Gaussian resolution function.

L3

At L3 [25] the τ -lepton lifetime is also measured developing two separate techniques for 3-prong and 1-prong decays.

- *Decay length method.* For 3-prong tau decays, the secondary vertex is fitted and the decay length is computed as its distance from the nominal IP position. The obtained decay length distribution is then fitted maximizing the likelihood of the convolution of an exponential decay and a Gaussian resolution. The mean value of the exponential is converted to a lifetime estimating the average tau momentum.
- *Impact parameter method.* For 1-prong decays the distribution of the signed impact parameter in the transverse plane is considered. The distribution is then fitted using a model estimated from MC simulation and including τ -lifetime as a free parameter.

DELPHI

At the DELPHI experiment, three different methods were developed [26].

Two methods make use of the 1-prong \times 1-prong topology, reproposing the same techniques adopted by ALEPH, namely the *impact parameter difference method* and the *miss distance method* (which corresponds to the *momentum dependent impact parameter sum method*). The general idea behind both, is that the transverse impact parameter d of a prompt track from a τ decay depends on the decay length ℓ_τ as

$$d = \ell_\tau \sin \theta_\tau \sin(\varphi - \varphi_\tau)$$

where θ_τ and φ_τ are, respectively, the polar and azimuthal angle of the decaying tau. φ is the azimuth direction of the considered track.

Instead, for events with at least one tau decaying to 3-prong, the secondary vertex can be directly reconstructed:

- *Decay vertex method.* It exploits the distance ℓ_τ , measured in the transverse plane, between the reconstructed τ 3-prong vertex and the center of the beam crossing region. ℓ_τ is converted to the decay proper time as $t = \ell_\tau / \beta\gamma c \sin \theta_\tau$. θ_τ is the polar angle of the τ direction, approximated by the thrust axis of the event, and the factor $\beta\gamma$ is corrected for ISR/FSR.

3.2.2 $\Upsilon(4S)$ and B-factories

At the $\Upsilon(4S)$ center of mass tau-leptons are produced in pairs through the electromagnetic scattering $e^+e^- \rightarrow \tau^+\tau^-(\gamma)$. The mean tau decay length λ_τ scales about linearly with the cms energy (if the approximation $\sqrt{s} \gg m_\tau$ is valid) and at $\sqrt{s} = 10.58$ GeV, $\lambda_\tau \approx 250$ μm . Moreover, in experiment operating at asymmetric B-factories, such as Babar and Belle, the tau energy spectrum in the laboratory is not monochromatic.

CLEO II

The CLEO II detector was placed at the Cornell Electron-positron Storage Ring (CESR) working at the $\Upsilon(4S)$ center of mass energy. The same method is applied on the 1-prong \times 3-prong selection and on 3-prong \times 3-prong selection. The flight direction of the tau pair is approximated to the momentum vector of the 3-prong tracks (in the case 3-prong \times 3-prong the difference of the momenta on the two sides is taken). The decay length in the transverse plane ℓ_{xy} is then obtained through a fit including the IP position and the reconstructed 3-prong vertex. The proper time is eventually determined as

$$ct = \frac{m_\tau}{p_\tau} \frac{\ell_{xy}}{\sin \theta_\tau}$$

where θ_τ is the polar angle of the estimated tau pair direction and p_τ is known from the beam energy, being CESR a symmetric collider.

BaBar

The BaBar analysis uses tau pairs events in which one tau decays to 3-prong, and the other in one electron and two neutrinos [27]. The method closely mimic the CLEO II one. The decay vertex and the average interaction point are projected on the plane transverse to the total momentum. The transverse decay length ℓ_τ^t , determined as their distance in the transverse plane, is then converted to ℓ_τ dividing by $\sin\theta_\tau$, being θ_τ the polar angle of the τ direction, approximated to the total 3-prong momentum vector. The meanlife is finally obtained from the τ mass and the mean τ momentum, estimated from simulation.

Belle

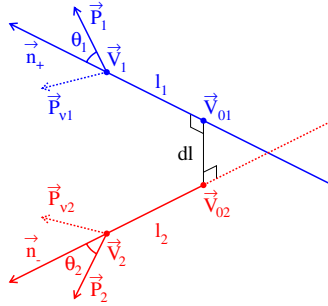


Figure 3.2: Scheme showing the τ decay length reconstruction variable used at the Belle experiment [12]. Both taus in the pair decay to 3-prong, the two sides are labeled as 1 and 2.

At the Belle experiment, the most precise τ -lepton lifetime measurement has been performed [12]. The events with both tau decaying to 3 pions and one neutrino were used as a sample, so that the secondary vertex positions \vec{V}_1 , for τ^+ and \vec{V}_2 for τ^- can be fitted. Then the two-folded system, described in the next section (see table 3.1), is solved using as input the measured hadronic momenta \vec{P}_1 , \vec{P}_2 and the nominal beam energies. The average of the two solutions is taken as τ^\pm momentum. Considering now the unit vectors \hat{n}_+ for the τ^+ momentum and \hat{n}_- for the τ^- momentum, they in general don't intersect. As shown in Figure 3.2, let dl be the minimum distance of the two directions and \vec{V}_{01} , \vec{V}_{02} the points of minimum distance for each line (see Figure 3.2). Then the distances l_1 , from \vec{V}_1 to \vec{V}_{01} , and l_2 , from \vec{V}_2 to \vec{V}_{02} , are taken as τ^+ and τ^- decay lengths respectively.

From the momentum estimated solving the two-folded system, the proper decay time distribution is obtained, and then fitted to extract the meanlife. A value $\tau_\tau = (290.17 \pm 0.53(\text{stat}) \pm 0.33(\text{sys})) \text{ fs}$ was obtained using 711 fb^{-1} of data.

3.3 Full reconstruction method

During the work of this thesis, we have developed a new method to measure τ lifetime at the Belle II experiment. The general idea is to combine the reconstruction of the tau momentum and decay length in a unique system of equations. This approach makes possible to use the information both from impact parameters of 1-prong tracks and from fitted vertex of 3-prong tracks. An important feature to be exploited, specific for the SuperKEKB collision scheme, is the strong constraint on the primary vertex position. The luminous region has nominal designed dimensions $\sigma_x^* \approx 10 \mu\text{m}$, $\sigma_y^* \approx 50 \text{ nm}$ and $\sigma_z^* \approx 250 \mu\text{m}$.

The kinematic reconstruction of tau pair events with only hadronic final states is a well-known technique, even adopted for τ -life measurement at Belle. A possible procedure to solve it, and its extension to include the τ decay length information, is shown in this section.

3.3.1 Kinematic reconstruction

An estimate of τ momentum is needed in order to reconstruct proper time. However, the tau four-momentum p_τ cannot be directly measured because of the unknown momentum carried away by one or more neutrinos in the final state. At Belle II, the τ leptons are produced in pairs through the process $e^+e^- \rightarrow \tau^+\tau^-$, hence the sum of the four-momenta $p_{\tau^+} + p_{\tau^-}$ is constrained to the total initial four-momentum in the laboratory p_{lab} . This introduces 8 unknowns quantities (p_{τ^+}, p_{τ^-}) and 4 constraints (p_{lab}).

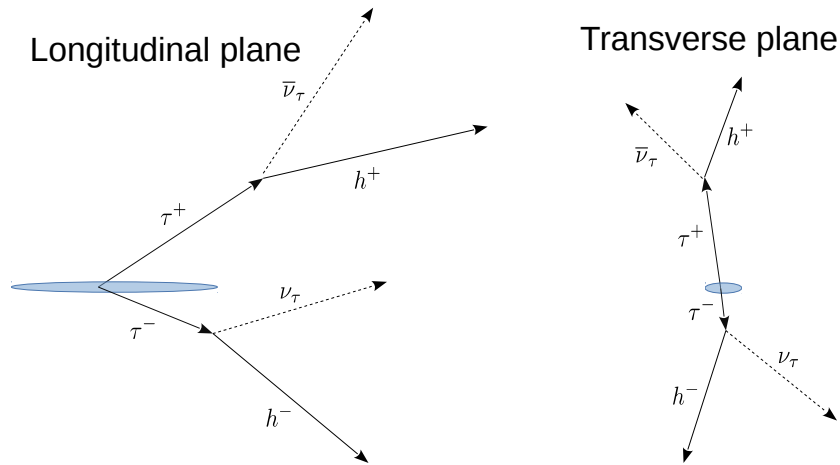


Figure 3.3: Sketch showing longitudinal (z, y) and transverse (x, y) view of τ pair production and subsequent decay into hadrons for an asymmetric collider. The blue area represents the beam spot region, note that the picture is not in scale.

Consider now events in which both τ decay like $\tau^\pm \rightarrow h^\pm \nu_\tau^{(\mp)}$, where h^\pm represents

Table 3.1: List of all the possible kinematic relations for an event $e^+e^- \rightarrow \tau^+\tau^-$ with both taus decaying to hadrons. The four-momenta of e^\pm and h^\pm are assumed known. Fixing also the masses of τ^\pm and neutrinos, the number of equations equal the number of unknowns. However, such system of equation has, in general, two distinct real solutions.

	Unknowns	Constraints
$p_{\tau^+} + p_{\tau^-} = p_{\text{lab}}$	8	p_{τ^+}, p_{τ^-}
$p_{\tau^+} = p_{h^+} + p_{\bar{\nu}}$	4	$p_{\bar{\nu}}$
$p_{\tau^-} = p_{h^-} + p_{\nu}$	4	p_{ν}
$p_{\tau^+}^2 = p_{\tau^-}^2 = m_\tau^2$		2
$p_{\bar{\nu}}^2 = p_{\nu}^2 = 0$		2
Total	16	16

one or more hadrons with total charge ± 1 (see Figure 3.3). The energy-momentum conservation in the decay implies $p_{\tau^+} = p_{h^+} + p_{\bar{\nu}}$ and $p_{\tau^-} = p_{h^-} + p_{\nu}$. These are 8 equations with 8 new unknowns, given by the neutrinos four-momenta, while p_{h^+} and p_{h^-} , the total four-momenta of the hadronic final states, are all measured by the detector. Four additional equations come from the on-shell condition for each of the two taus and neutrinos. All in all, the tau pair decay kinematic is described by a completely constrained system with 16 equations and 16 unknowns, summarized in table 3.1.

Though fully constrained, such a system has in general two real solutions [28], i.e. two distinct combinations of $(p_{\tau^+}, p_{\tau^-}, p_{\nu}, p_{\bar{\nu}})$ satisfy all the relations in table 3.1, but only one corresponds to the actual four momenta of taus and neutrinos. To show this ambiguity, the four-momentum conservation in the decay can be rewritten

$$p_{\tau^\pm} - p_{h^\pm} = p_{(\bar{\nu})}$$

Squaring both members, we obtain the angles θ_\pm between the direction of the τ^\pm and the total momentum vector of their hadronic final states h^\pm :

$$\cos \theta_\pm = \frac{2E_{\tau^\pm}E_{h^\pm} - m_\tau^2 - m_{h^\pm}^2}{|\vec{p}_{h^\pm}| \sqrt{E_{\tau^\pm}^2 - m_\tau^2}}$$

where we took advantage of the on-shell relations $p_{\tau^+}^2 = p_{\tau^-}^2 = m_\tau^2$ and $p_{\bar{\nu}}^2 = p_{\nu}^2 = 0$. m_{h^\pm} are the invariant masses of the hadronic final states h^\pm .

The τ^+ direction therefore lies on a conic surface of opening angle θ_+ having \vec{p}_{h^+} as axis; analogously for the τ^- momentum direction. The opening angles θ_+, θ_- both depend only on the unknown τ^\pm energies E_{τ^\pm} . For simplicity, let's assume the laboratory frame coinciding with the center of mass frame, i.e. $p_{\text{lab}} = (E_{\text{lab}}, \vec{0})$. In such a situation $E_{\tau^\pm} = E_{\text{lab}}/2$, so that $\cos \theta_\pm$ are determined just measuring p_{h^\pm} , while τ^+ and τ^- have the same direction. The intersection of the two cones gives in general two possible solution for the τ s direction.

The angle between the two hadrons momentum can be expressed as

$$\cos \phi = \hat{n}_+ \cdot \hat{n}_-$$

with \hat{n}_\pm unitary vectors for the two hadrons momentum directions:

$$\hat{n}_- = \frac{\vec{p}_-}{|\vec{p}_-|} = \begin{pmatrix} \sin \theta_- \\ 0 \\ \cos \theta_- \end{pmatrix} \quad \hat{n}_+ = \frac{\vec{p}_+}{|\vec{p}_+|} = \begin{pmatrix} \sin \theta_+ \cos \phi \\ \sin \theta_+ \sin \phi \\ -\cos \theta_+ \end{pmatrix} \quad (3.2)$$

hence we find

$$\cos \phi = \frac{\cos \theta_+ \cos \theta_-}{\sin \theta_+ \sin \theta_- - 1}$$

Minimization

Because of the four quadratic equations for the mass constraints, the system described in table 3.1 is of degree 2^4 and cannot be solved analytically in a closed form. A numerical resolution approach should then be undertaken.

First of all, the system is simplified using the neutrino mass constraints and the momentum conservation in the tau decays for removing neutrino four-momenta:

$$\begin{aligned} \vec{p}_\nu &= \vec{p}_{\tau^-} - \vec{p}_{h^-} & E_\nu &= |\vec{p}_\nu| = |\vec{p}_{\tau^-} - \vec{p}_{h^-}| \\ \vec{p}_{\bar{\nu}} &= \vec{p}_{\tau^+} - \vec{p}_{h^+} & E_{\bar{\nu}} &= |\vec{p}_{\bar{\nu}}| = |\vec{p}_{\tau^+} - \vec{p}_{h^+}| \end{aligned}$$

Hence the system is rewritten like

$$\begin{cases} E_{\tau^+} + E_{\tau^-} - E_{\text{lab}} = 0 \\ \vec{p}_{\tau^+} + \vec{p}_{\tau^-} - \vec{p}_{\text{lab}} = 0 \\ E_{\tau^-} - E_{h^-} - |\vec{p}_{\tau^-} - \vec{p}_{h^-}| = 0 \\ E_{\tau^+} - E_{h^+} - |\vec{p}_{\tau^+} - \vec{p}_{h^+}| = 0 \end{cases} \quad (3.3)$$

where the τ^\pm energies depend on the momenta $E_{\tau^\pm} = \sqrt{m_\tau^2 + \vec{p}_{\tau^\pm}^2}$ and $m_\tau \equiv m_{\tau^+} = m_{\tau^-}$ is assumed. The 6 equations left contain exactly 6 unknowns, given by the momentum vectors \vec{p}_{τ^+} and \vec{p}_{τ^-} . To solve the (3.3) numerically, a positive-defined function F_{kin} is introduced:

$$\begin{aligned} F_{\text{kin}}(\vec{p}_{\tau^+}, \vec{p}_{\tau^-}) &= (E_{\tau^+} + E_{\tau^-} - E_{\text{lab}})^2 + |\vec{p}_{\tau^+} + \vec{p}_{\tau^-} - \vec{p}_{\text{lab}}|^2 + \\ &\quad (E_{\tau^-} - E_{h^-} - |\vec{p}_{\tau^-} - \vec{p}_{h^-}|)^2 + (E_{\tau^+} - E_{h^+} - |\vec{p}_{\tau^+} - \vec{p}_{h^+}|)^2 \end{aligned} \quad (3.4)$$

with $E_{\tau^\pm} = \sqrt{m_\tau^2 + \vec{p}_{\tau^\pm}^2}$. By definition, F_{kin} is always ≥ 0 and $F_{\text{kin}} = 0$ if and only if \vec{p}_{τ^\pm} are solutions of (3.3). Therefore the kinematic system (3.3) can be solved finding the values \vec{p}_{τ^+} , \vec{p}_{τ^-} which event per event minimize F_{kin} . As there are two real solutions of the system 3.1, also F_{kin} will have a double minimum. We expect then that the minimization routine will randomly converge to one of the two minima.

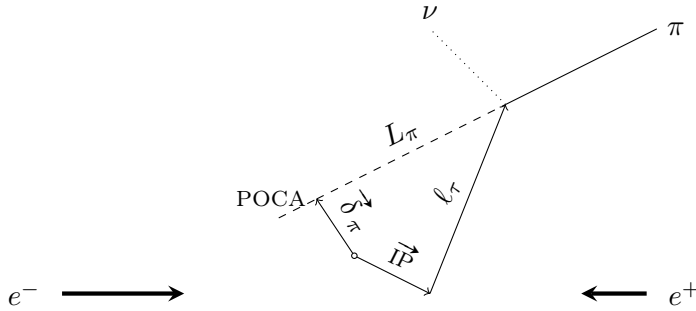


Figure 3.4: Scheme defining the tracking variables of interest for a τ -lepton decaying to 1-prong. The empty circle represents the origin of coordinates. In general, the production point of the τ will be displaced from the origin by a vector \vec{IP} . ℓ_τ is the path of the decaying tau. L_π is the distance between the decay vertex and the point of closest approach (POCA) of the final hadron. $\vec{\delta}_\pi$ is its 3-dimensional impact parameter, defined respect to the origin.

3.3.2 Decay length reconstruction at Belle II

In the following, we propose an idea to estimate the τ decay length both for 1-prong and 3-prong decays, provided the presence of only one neutrino in each tau final state. Let us assume for simplicity that the tau momentum vectors are known. In the next section, this method will be merged with the kinematic reconstruction described above.

One of the major advantages of Belle II respect to the previous generation B-factories is the tiny beam spot size at the interaction point. In particular, reaching $\beta_y^* \simeq 0.3$ mm, the expected vertical beam size is $\sigma_y^* \simeq 50$ nm. The implication of such high focusing is that the y coordinate of the primary vertex position is constrained to the nominal IP_y with a Gaussian uncertainty ≈ 50 nm.

1-prong: impact parameter

Suppose the τ -lepton decaying to one charged hadron π (which can be either a pion or a kaon) and a neutrino, with possibly additional neutral hadrons. Suppose also that the momentum \vec{p}_π and the 3D impact parameter of the charged hadron have been measured, while the tau momentum is assumed to be known. The goal is to extrapolate the tau decay length from these quantities.

For the 1-prong topology, the tau decay vertex position cannot be directly measured. However, the decay vertex must lay along the 1-prong track, hence the impact parameter of the charged track provide information on the tau decay length. In order to show this explicitly, let's refer to the sketch in Figure 3.4. The 3-dimensional impact parameter $\vec{\delta}_\pi$ of the charged hadron corresponds to the point of closest approach (POCA) position with respect to the origin of the coordinate system. The actual interaction point (IP) will be in general displaced from the origin, we denote its position as \vec{IP} . Looking again at Figure 3.4, the following vectorial relation is

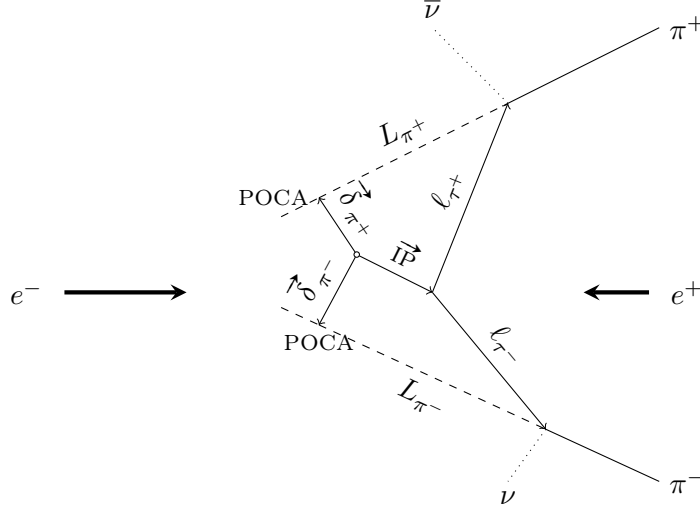


Figure 3.5: Schematic view of a tau pair event production and decay to one charged hadron on each side. The notation is the same as in Figure 3.4, except that the two sides are distinguished by a \pm index.

straightforward:

$$\vec{\text{IP}} + l_\tau \hat{n}_\tau = \vec{\delta}_\pi + L_\pi \hat{n}_\pi \quad (3.5)$$

where $\hat{n}_\tau = \vec{p}_\tau / |\vec{p}_\tau|$ and $\hat{n}_\pi = \vec{p}_\pi / |\vec{p}_\pi|$ are the unit vectors defining the tau and hadron¹ momentum directions, respectively. l_τ is the tau decay length while L_π is the distance from the POCA to the secondary vertex, along the 1-prong charged track. Assuming tau momenta reconstructed, the only unknowns in (3.5) are $\vec{\text{IP}}$, l_τ and L_π .

The same argument can be repeated for the second tau, in an event where both leptons decay with hadronic 1-prong mode. Distinguishing variables from τ^+ and τ^- decay, as shown in Figure 3.5, relation (3.5) is automatically extended as

$$\begin{cases} \vec{\text{IP}} + l_{\tau^+} \hat{n}_{\tau^+} = \vec{\delta}_{\pi^+} + L_{\pi^+} \hat{n}_{\pi^+} \\ \vec{\text{IP}} + l_{\tau^-} \hat{n}_{\tau^-} = \vec{\delta}_{\pi^-} + L_{\pi^-} \hat{n}_{\pi^-} \end{cases} \quad (3.6)$$

These are 6 independent relations containing 7 unknown quantities, namely $\vec{\text{IP}}$, l_{τ^\pm} and L_{π^\pm} . We can now make use of the beam spot constraint fixing IP_y and thus reducing the number of unknowns to 6. So the information on the primary vertex enters the decay length reconstruction. It is worth to emphasize that, for the 1-prong \times 1-prong topology, a completely constrained system of equations like the one in table (3.6) is possible only thanks to the nano-beam collision scheme implemented at SuperKEKB.

¹We emphasize that in case of a 1-prong decay with additional neutral hadrons, \vec{p}_π is the momentum of the charged hadron only. However, the full momentum \vec{p}_h on the 1-prong side is always the one entering the kinematic relations (3.3).

3-prong: decay length

A similar approach is possible considering the 3-prong decay as well. In this case the position $\vec{v}_{3\pi}$ of the vertex $\tau \rightarrow 3\pi$ can be fitted using, for instance, the `TreeFitter` module provided by `basf2`. Referring to the variables in Figure 3.6, a triangular relation can be written as

$$\vec{\text{IP}} + \ell_\tau \hat{n}_\tau = \vec{v}_{3\pi} \quad (3.7)$$

where the unknowns are $\vec{\text{IP}}$ and ℓ_τ . Again, using the constraint on IP_y , the 3 equations in (3.7) contain only 3 unknown quantities, hence the 3-prong topology permits to reconstruct the decay length ℓ_τ even without considering the other tau in the pair.

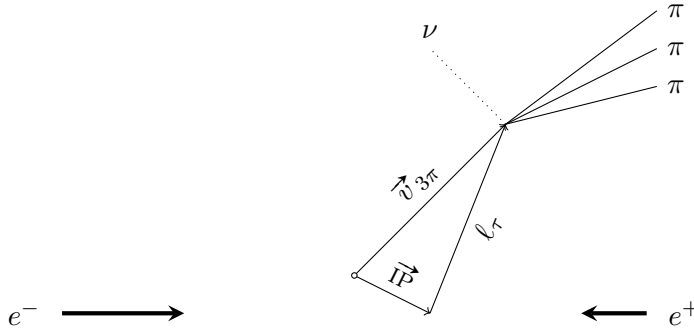


Figure 3.6: Scheme of a produced τ -lepton which decays to 3 charged hadrons. In this case, the position of the decay vertex respect to the origin (empty circle) can be directly fitted. The position of the primary vertex, $\vec{\text{IP}}$, still needs to be reconstructed, but the y coordinate can be fixed, thanks to the small vertical size of the beam spot at Belle II.

Extending the reconstruction to the full pair, the system will be in general overconstrained: 5 unknown and 6 equations for the 1-prong \times 3-prong topology; 4 unknown with 6 equations considering the 3-prong \times 3-prong topology.

3.3.3 Full reconstruction

The two system of equations obtained for the tau pair kinematic and decay length can be merged together. In section 3.3.2, tau momenta were assumed to be known. As shown in section 3.3.1, their values can be found with a two-fold ambiguity solving the kinematic system (3.3). Merging it with the geometrical constraints on track directions and vertex positions solves the two-fold ambiguity, as the new part is a linear system, having in general at most a unique solution. Table 3.1 is therefore extended to 3.2 for the mixed 1-prong \times 3-prong case.

Following the same discussion of section 3.3.1, the system can be solved numerically minimizing a positive defined function F , which is now extended to include the new equations. Taking again as a reference the 1-prong \times 3-prong case (but the same procedure is replicable for all the topologies with both taus decaying hadronically), a

11-parameters function can be written:

$$\begin{aligned}
F(\vec{p}_{\tau^+}, \vec{p}_{\tau^-}, \ell_{\tau^+}, \ell_{\tau^-}, \text{IP}_x, \text{IP}_z, L_{h^+}) = \\
\left\{ (E_{\tau^+} + E_{\tau^-} - E_{\text{lab}})^2 + |\vec{p}_{\tau^+} + \vec{p}_{\tau^-} - \vec{p}_{\text{lab}}|^2 + \right. \\
\left. (E_{\tau^+} - E_{h^+} - |\vec{p}_{\tau^+} - \vec{p}_{h^+}|)^2 + (E_{\tau^-} - E_{h^-} - |\vec{p}_{\tau^-} - \vec{p}_{h^-}|)^2 \right\} / (\text{GeV}^2) + \\
\left\{ |\vec{\text{IP}} + \ell_{\tau^-} \hat{n}_{\tau^-} - \vec{v}_{3\pi}|^2 + \left| \vec{\text{IP}} + \ell_{\tau^+} \hat{n}_{\tau^+} - \vec{\delta}_{\pi^+} - L_{\pi^+} \hat{n}_{\pi^+} \right|^2 \right\} / (100 \mu\text{m})^2
\end{aligned} \quad (3.8)$$

where $E_{\tau^\pm} = \sqrt{m_\tau^2 + \vec{p}_{\tau^\pm}^2}$ and $\hat{n}_i = \vec{p}_i / |\vec{p}_i|$. The signs \pm labeling the two opposite taus are used just to distinguish the 1-prong side from the 3-prong one. The measured quantities are the energies and momenta of the hadronic final state E_h , \vec{p}_h , and the POCA position $\vec{\delta}_\pi$ of the 1-prong charged hadron, while the vertex position \vec{v}_{3h} is fitted separately using the 3-prong tracks. The total energy and momentum of the beams in the laboratory frame (E_{lab} , \vec{p}_{lab}), as well as IP_y , are fixed event per event to their nominal values.

Table 3.2: Relations containing all the kinematic information (included from table 3.1) and the vertexes constraints for a tau pair to 1-prong \times 3-prong hadrons. Such system is completely constrained, furthermore, the two-fold ambiguity for the tau momenta is removed using the information on the track parameters.

	Unknowns	Constraints
$p_{\tau^+} + p_{\tau^-} = p_{\text{lab}}$	8	p_{τ^+}, p_{τ^-}
$p_{\tau^+} = p_{h^+} + p_{\bar{\nu}}$	4	$p_{\bar{\nu}}$
$p_{\tau^-} = p_{h^-} + p_{\nu}$	4	p_{ν}
$p_{\tau^+}^2 = p_{\tau^-}^2 = m_\tau^2$		2
$p_{\bar{\nu}}^2 = p_{\nu}^2 = 0$		2
$\vec{\text{IP}} + \ell_{\tau^-} \hat{n}_{\tau^-} = \vec{v}_{3\pi}$	3	$\text{IP}_x, \text{IP}_z, \ell_{\tau^-}$
$\vec{\text{IP}} + \ell_{\tau^+} \hat{n}_{\tau^+} = \vec{\delta}_{\pi^+} + L_{\pi^+} \hat{n}_{\pi^+}$	2	ℓ_{τ^+}, L_{π^+}
Total	21	22

The function F is the sum of 12 quadratic terms, each representing a constraint. As long as they have different dimensions, the minimization routine would favor the biggest ones. Then the 6 terms of F accounting for the vertex constraints are rescaled by a dimensional constant $100 \mu\text{m}$, while the vertex constraints by 1 GeV . In this way all the terms are adimensional and of the same order of magnitude.

The set of parameters which minimize F contains the full information needed to estimate the proper decay time for both taus in the pair:

$$ct_{\tau^\pm} = \frac{\ell_{\tau^\pm}}{(\beta\gamma)_{\tau^\pm}} = \frac{m_\tau}{|\vec{p}_{\tau^\pm}|} \ell_{\tau^\pm}$$

Furthermore, three additional parameters, namely IP_x , IP_z , and L_{π^+} are optimized as well. These supplementary information, in particular the primary vertex position, can be used as a control-check for the minimization.

In principle, the method described works for all the tau pair events where both taus decay with only one neutrino. This means that the leptonic decays $\tau \rightarrow \ell \nu_\tau \nu_\ell$, with $\ell = e, \mu$, are excluded, while the method can be applied on about 42% of the produced tau pairs. Indeed about 65% of the total tau decay modes have one neutrino only. The main accessible modes are listed in table 3.3.

Table 3.3: List of the τ -lepton hadronic decay channels having a branching fraction above 1%. The values are taken from PDG [11].

τ^- decay modes		BR [%]
$\pi^- \pi^0 \nu_\tau$	1-prong	25.5
$\pi^- \nu_\tau$	1-prong	10.8
$\pi^- 2\pi^0 \nu_\tau$	1-prong	9.3
$\pi^- \pi^+ \pi^- \nu_\tau$	3-prong	9.0
$\pi^- \pi^+ \pi^- \pi^0 \nu_\tau$	3-prong	2.7
$\pi^- 3\pi^0 \nu_\tau$	1-prong	1.0

3.4 Reconstruction procedure

The method described in section 3.3 is tested on a pure signal MC sample. The simulated topology is a τ pair event where one τ decays in a charged pion and a neutrino while the other τ decays to three charged pions plus one neutrino. Such a signal makes possible to check the full reconstruction approach in the mixed case: the impact parameter information exploited on the 1-prong side and the fitted vertex constraint on the 3-prong tau.

The signal sample is thus composed of 100000 $\tau(\rightarrow \pi\nu)\tau(\rightarrow \pi\pi\pi\nu)$ events, generated through the `KK2f` generator [17] and simulated with Geant4, using the standard Belle II software framework `basf2`. At the generation level, the tau lifetime is $c\tau_\tau = 87.03 \mu\text{m}$. After the Belle II detector simulation, all events with exactly 4 reconstructed charged pions of total zero charge are kept. An additional selection is performed requiring 3 tracks to be daughters of a tau (tagged as 3-prong), and the remaining track to be daughter of the other tau (labeled as 1-prong). In this way, fake tracks or interactions with the detector material are rejected. The events selected amount to 64497.

Firstly the kinematic only reconstruction will be performed. The minimization exploits a quasi-Newton method, namely the Broyden-Fletcher-Goldfarb-Shanno (BFGS) algorithm [29].

3.4.1 Reconstruction of tau pair momenta

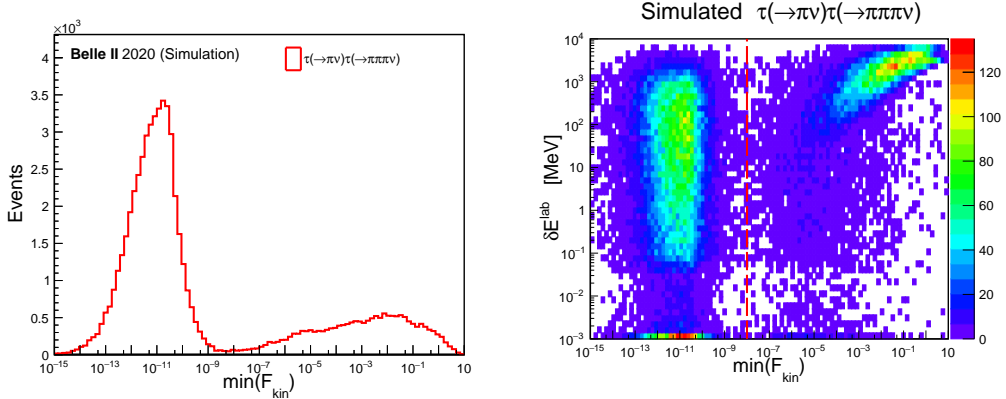
The function to be minimized event per event is

$$\begin{aligned}
 F_{\text{kin}}(\vec{p}_{\tau_{1\text{-prong}}}, \vec{p}_{\tau_{3\text{-prong}}}) = & \\
 & (E_{\tau_{1\text{-prong}}} + E_{\tau_{3\text{-prong}}} - E_{\text{lab}})^2 + \\
 & |\vec{p}_{\tau_{1\text{-prong}}} + \vec{p}_{\tau_{3\text{-prong}}} - \vec{p}_{\text{lab}}|^2 + \\
 & (E_{\tau_{1\text{-prong}}} - E_{h_{1\text{-prong}}} - |\vec{p}_{\tau_{1\text{-prong}}} - \vec{p}_{h_{1\text{-prong}}}|)^2 + \\
 & (E_{\tau_{3\text{-prong}}} - E_{h_{3\text{-prong}}} - |\vec{p}_{\tau_{3\text{-prong}}} - \vec{p}_{h_{3\text{-prong}}}|)^2
 \end{aligned} \tag{3.9}$$

The tau energy is determined by the mass shell condition $E_{\tau} = \sqrt{m_{\tau}^2 + \vec{p}_{\tau}^2}$, with the mass fixed to the PDG average one $m_{\tau} = 1.777$ GeV. $h_{3\text{-prong}}$ refers to the four-momentum sum of the 3 pions from the 3-prong decay:

$$E_{h_{3\text{-prong}}} = \sum_{i=1}^3 E_{\pi_i} \quad \vec{p}_{h_{3\text{-prong}}} = \sum_{i=1}^3 \vec{p}_{\pi_i}$$

The initial four-momentum in the laboratory frame is set event per event to the total nominal beam four-momentum, that, in the produced MC, is always equal to $E_{\text{lab}} = 11.006$ GeV, $\vec{p}_{\text{lab}} = (0.457, 0.0, 2.999)$ GeV. The measured hadronic momenta $\vec{p}_{h_{1\text{-prong}}}$ and $\vec{p}_{h_{3\text{-prong}}}$ are chosen as the starting parameters for tau momenta in the minimization.



(a) Minimum value found for function (3.9). (b) Energy loss in the laboratory frame against the minimum found from (3.9).

Figure 3.7: Distribution of the minimum value resulting from the minimization, on the $(\vec{p}_{\tau_{1\text{-prong}}}, \vec{p}_{\tau_{3\text{-prong}}})$ parameter space, of the function F_{kin} (3.9). On the right plot, the same distribution is shown jointed with the variable δE^{lab} , defined as the missing energy (mainly from ISR/FSR) in the tau pair system, measured in the laboratory frame. For higher minima, a correlation is observed. Note that both axis are in log scale.

The minimization routine converges successfully for all the 64497 events. In Figure 3.7a the distribution of the minimum value found for F_{kin} is plotted on a logarithmic

scale. The distribution of the minimum value shows two categories of events. The first one ($\min(F_{\text{kin}} < 10^{-8})$) for which the minimum is really close to zero, and the second one, for which the constraints on total energy and momentum are not well satisfied:

$$(E_{\tau_{1\text{-prong}}} + E_{\tau_{3\text{-prong}}} - E_{\text{lab}})^2 + |\vec{p}_{\tau_{1\text{-prong}}} + \vec{p}_{\tau_{3\text{-prong}}} - \vec{p}_{\text{lab}}|^2 > 0 \quad (3.10)$$

In order to prove this statement, we define the energy loss in the laboratory as

$$\delta E^{\text{lab}} = E_{\text{lab}} - E_{\tau_{1\text{-prong}}}^{\text{MC}} - E_{\tau_{3\text{-prong}}}^{\text{MC}}$$

where the tau energies are the ones from MC generation. $\delta E^{\text{lab}} > 0$ is due to ISR and FSR photons, which are taken into account in the KK2f tau pair generator. Note that KK2f doesn't simulate the beam energy spread, that is of the order of few MeV. The joint distribution of $\min(F_{\text{kin}})$ and δE^{lab} shows a correlation between this two variables for events belonging to the region of higher F_{kin} minima. The events with $\delta E^{\text{lab}} > 1$ GeV are concentrated in that region.

Therefore, tau pair events with high ISR/FSR losses are not properly reconstructed by the minimization procedure, as the term (3.10) will dominate and force the total tau four-momentum near a wrong value. The same problem is expected to occur for the global reconstruction, where the term (3.10) is unchanged. Hence events resulting in an high minimum value of F_{kin} are preliminary discarded. Choosing arbitrary to cut at the plateau $\min(F_{\text{kin}}) = 10^{-8}$, in the region below the cut the average energy loss is $\langle \delta E \rangle = 135$ MeV while, for the 17224 excluded events with $\min(F_{\text{kin}}) > 10^{-8}$, the mean missing energy is $\langle \delta E \rangle = 1.34$ GeV. This class of events, which has a significant energy loss, could be reduced also cutting events with high energy photons reconstructed in the ECL.

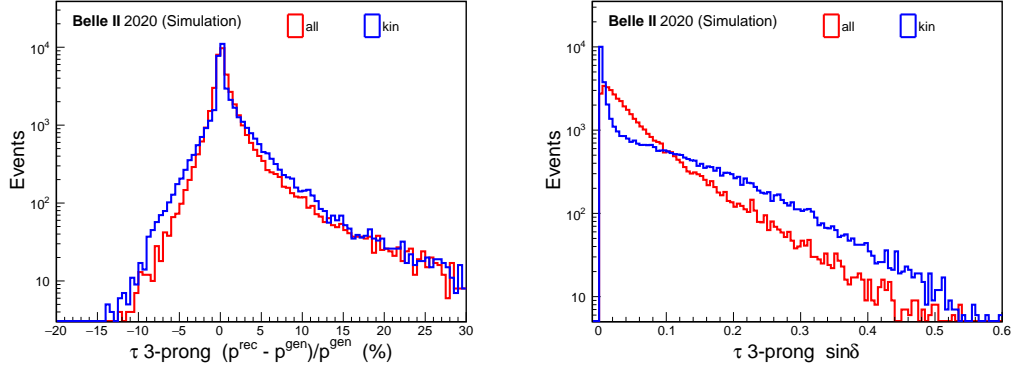
3.4.2 Reconstruction of tau decay time

The 47273 events left after the cut on $\min(F_{\text{kin}})$ are used to test the reconstruction presented in section 3.3.2. The function to be minimized is $F = F_{\text{kin}} + F_{\text{ver}}$, where

$$F_{\text{ver}}(\vec{p}_{\tau_{1\text{-prong}}}, \vec{p}_{\tau_{3\text{-prong}}}, \ell_{\tau_{1\text{-prong}}}, \ell_{\tau_{3\text{-prong}}}, \text{IP}_x, \text{IP}_z, L_{1\text{-prong}}) = \left\{ \left| \vec{\text{IP}} + \ell_{\tau_{3\text{-prong}}} \hat{n}_{\tau_{3\text{-prong}}} - \vec{v}_{3\text{-prong}} \right|^2 + \left| \vec{\text{IP}} + \ell_{\tau_{1\text{-prong}}} \hat{n}_{\tau_{1\text{-prong}}} - \vec{\delta}_{1\text{-prong}} - L_{1\text{-prong}} \hat{n}_{\pi_{1\text{-prong}}} \right|^2 \right\} / (100 \mu\text{m})^2 \quad (3.11)$$

and F_{kin} is the function (3.9), divided by (GeV^2) to be adimensional as well. The starting values for the minimization are chosen to the nominal position for the IP, while the other length parameters $\ell_{\tau_{1\text{-prong}}}$, IP_x , IP_z and $L_{1\text{-prong}}$ are initially set to $100 \mu\text{m}$. The tau momenta start again from the measured hadronic momenta. The vertical IP position IP_y is fixed to its nominal value. The 3-prong vertex position $\vec{v}_{3\text{-prong}}$ is obtained exploiting the `TreeFitter` module, rejecting about 100 events for which the fit fails. The minimization of F fails for 448 events out of 47273. The optimized parameters are compared with the MC truth.

Reconstructed tau momenta



(a) Relative difference among the reconstructed and the generated τ 3-prong momentum modules. (b) $\sin \delta$ distribution, where δ is the angle between the reconstructed and the generated τ 3-prong momentum vectors.

Figure 3.8: Distributions of the reconstructed $\tau_{3\text{-prong}}$ momentum using only the kinematic constraints (3.9), or the full set (3.11). The variables shown are the relative difference with the generated momentum module (a), and the sin of the angle δ between $\tau_{3\text{-prong}}^{\text{gen}}$ (b).

The minimization of the complete set of constraints improves the quality of the tau momentum determination. A comparison of the results using only the kinematic constraints (3.9), or the full set (3.11), is presented in the following. The distributions of the difference between the reconstructed and generated module $p_\tau \equiv |\vec{p}_\tau|$ are plotted in Figure 3.8a for the 3-prong tau. Figure 3.8b shows the $\sin \delta$ distributions, where δ is the angle between the reconstructed tau momentum and the true momentum at the generator level, computed as

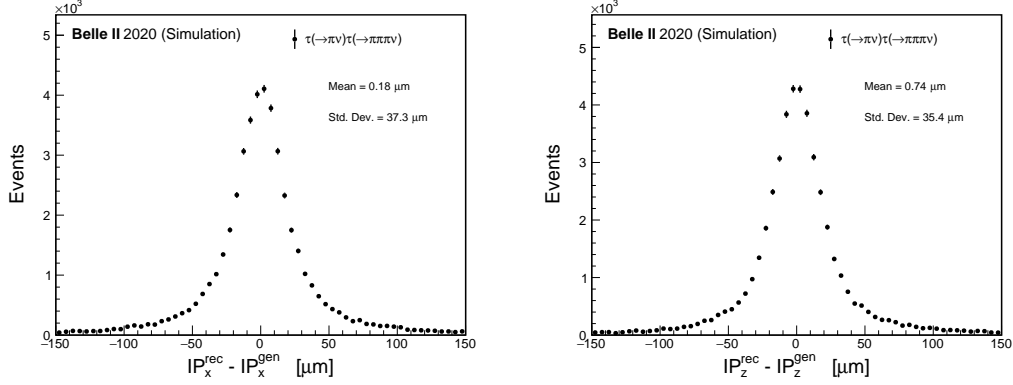
$$\sin \delta = \sqrt{1 - \left(\frac{\vec{p}_\tau^{\text{rec}} \cdot \vec{p}_\tau^{\text{gen}}}{p_\tau^{\text{rec}} p_\tau^{\text{gen}}} \right)^2}$$

For the histogram of Figure 3.8a, an asymmetric tail at $p^{\text{rec}} > p^{\text{gen}}$ is present for both the reconstruction distributions. It is due to residual ISR/FSR energy losses which reduce the generated momentum respect to the nominal one. This implies that for both methods the reconstructed momentum is overestimated.

Considering the tau direction, Figure 3.8b shows that minimizing only F_{kin} , the fraction of badly reconstructed momenta is higher. In particular, $\sin \delta$ is greater than 0.1 for 33% of the events reconstructed minimizing F_{kin} , while only 21% of the momenta which minimize F have $\sin \delta > 0.1$. The reason of such difference lies in the two-fold ambiguity of the kinematic system (3.3), which is removed when adding the constraints of F_{ver} . However, excluding the tails, the distribution obtained from F_{kin} only has a much narrower peak, implying a better resolution for the kinematic

reconstruction. This is not surprising, as adding F_{ver} also introduces new terms, whose error can be dominant in the minimization.

Reconstructed vertexes and decay time



(a) Residual distribution of the reconstructed primary vertex x position. (b) Residual distribution of the reconstructed primary vertex z position.

Figure 3.9: Distributions of the reconstructed—generated x (a) and z (b) primary vertex positions. The reconstruction is performed minimizing the 11-parameters function (3.11). The two distributions have comparable standard deviations, though they are generated with $\sigma_x^* = 6.4 \mu\text{m}$ and $\sigma_z^* = 155 \mu\text{m}$

Figure 3.9 shows the residual distribution of the reconstructed primary vertex positions IP_x and IP_z . Since the generated IP_x is distributed with $\sigma_x = 6.4 \mu\text{m}$, the implemented method is not able to resolve the x coordinate of primary vertex, reconstructed with a standard deviation of $37.3 \mu\text{m}$. Nonetheless, the variable IP_x^{rec} can be used as a control parameter to exclude events not properly reconstructed. On the other hand, the z position of the IP is estimated with a standard deviation of $35.4 \mu\text{m}$, much smaller than the generated distribution of the beam spot region, equal to $\sigma_z = 155 \mu\text{m}$. Hence, the actual longitudinal coordinate of the interaction vertex can be monitored exploiting tau pair events decaying to hadrons.

In Figure 3.10 the residual distributions for the reconstructed τ -decay proper time are shown. They are computed using the parameters $\vec{p}_\tau^{\text{rec}}$, ℓ_τ^{rec} optimized from the minimization of F ,

$$ct_\tau = \frac{m_\tau}{|\vec{p}_\tau^{\text{rec}}|} \ell_\tau^{\text{rec}}$$

The two distributions present an opposite bias, which is about double for the 1-prong proper time. All considered, the 3-prong decay mode seems more favorable for the measurement of the decay time, because of its smaller standard deviation and bias. Therefore, the information from the fitted 3-prong vertex position leads to a more accurate decay length reconstruction than using only the impact parameter of one

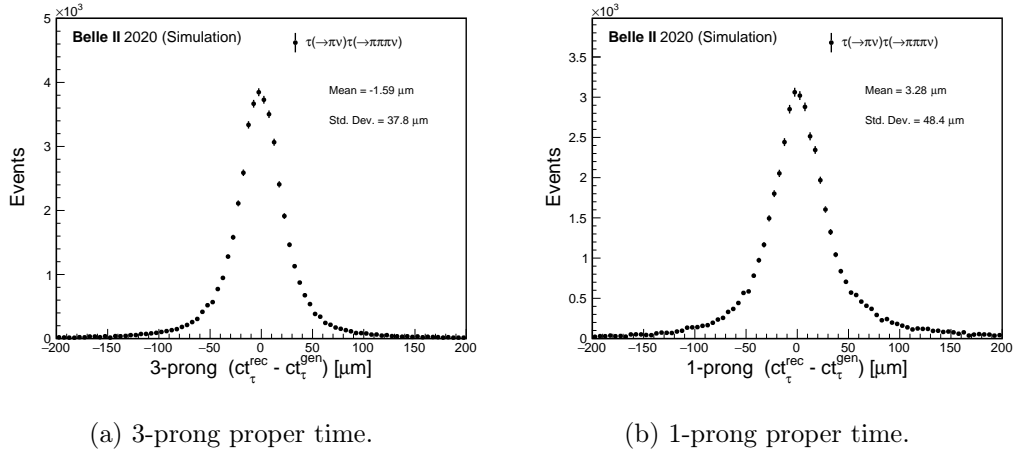


Figure 3.10: Reconstructed–generated decay proper times for the 3-prong (a) and 1-prong (b) tau candidates.

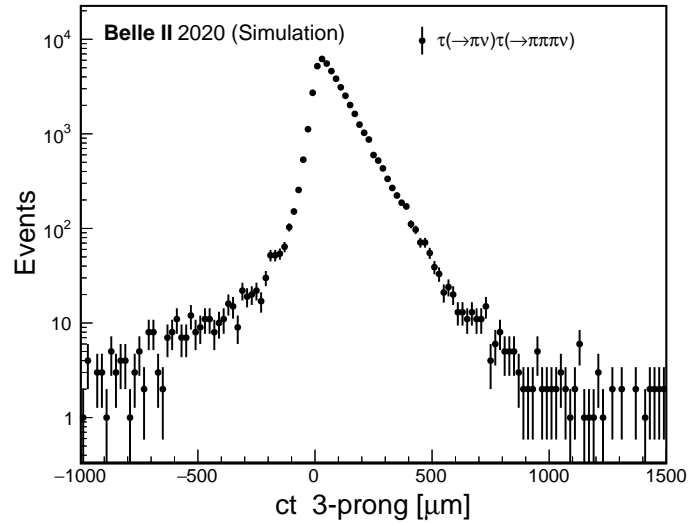


Figure 3.11: Proper time distribution of the reconstructed 3-prong tau. The reconstruction, minimizing the sum of functions (3.9) and (3.11), was performed on a MC sample containing pure $\tau(\rightarrow \pi\nu) \times \tau(\rightarrow \pi\pi\pi\nu)$ events. No selection was applied, except for an upper cut on the minimum value found on (3.9), rejecting events with $\min(F_{\text{kin}}) > 10^{-8}$.

track. As for IP_x , the decay length reconstructed on the 1-prong side can be used for cross check or as an additional selection variable to reduce the contamination from short lived backgrounds.

The proper time distribution for the 3-prong tau decay is shown in Figure 3.11. To extrapolate lifetime the distribution must be fitted with a probability density function (pdf) of the type (3.1), where the resolution function $\mathcal{R}(t^{\text{rec}} - t^{\text{gen}}; \vec{\xi})$ is a parametrization of the distribution in Figure 3.10a.

Chapter 4

Event selection and reconstruction

We want to test the method described in chapter 3 with Belle II data. After choosing an event topology, it is necessary to develop some selection criteria in order to have a sample with the highest fraction of events following the required decay mode. A Monte Carlo sample is used as reference for optimizing the quality of the selection.

4.1 Event Topology

To test the inclusive τ lifetime reconstruction method, we exploit the 1-prong \times 3-prong event topology in which the 1-prong tau decays as $\tau \rightarrow \pi\pi^0\nu_\tau$, while the 3-prong follows the mode $\tau^- \rightarrow \pi^- \pi^+ \pi^- \nu_\tau$ (Figure 4.1).

The main advantage of looking for the decay $\tau \rightarrow \pi\pi^0\nu_\tau$ on the 1-prong hemisphere is given by the fact that this is the highest branching ratio decay channel of the tau, with $\mathcal{B}_{1\text{-prong}} = (25.49 \pm 0.09)\%$. This value is about 2.5 times larger than the fraction of $\tau \rightarrow \pi\nu_\tau$. In addition, the π and the π^0 come mainly from the ρ meson resonance, making possible a clean selection on the 1-prong invariant mass around $m_\rho \simeq 775 \text{ MeV}$ (being $\Gamma_\rho \simeq 150 \text{ MeV}$). Therefore the decay $\tau \rightarrow \pi\pi^0\nu_\tau$ has also a stronger signature respect to $\tau \rightarrow \pi\nu_\tau$.

The test on the reconstruction method, performed in section 3.4.2, was done on a pure MC sample of $\tau(\rightarrow \pi\nu) \times \tau(\rightarrow \pi\pi\pi\nu)$ events. Using the ρ tag on the 1-prong side, we have an additional π^0 which must be considered in the kinematic reconstruction. Hence, referring to the set of constraints in the function (3.9), $p_{h_{1\text{-prong}}}$ is the total hadronic four-momentum on the 1-prong side, i.e.

$$E_{h_{1\text{-prong}}} = E_{\rho^\pm} = E_{\pi^\pm} + E_{\pi^0} \quad \vec{p}_{h_{1\text{-prong}}} = \vec{p}_{\rho^\pm} = \vec{p}_{\pi^\pm} + \vec{p}_{\pi^0} \quad \text{1-prong side}$$

Anyway, the impact parameter $\vec{\delta}_{1\text{-prong}}$, entering the relation 3.5, is the one measured for the charged track only. Thus, the unit vector $\hat{n}_{\pi_{1\text{-prong}}}$ defining the 1-prong track direction is determined just by the charged pion momentum

$$\hat{n}_{\pi_{1\text{-prong}}} = \frac{\vec{p}_{\pi^\pm}}{|\vec{p}_{\pi^\pm}|} \quad \text{1-prong side}$$

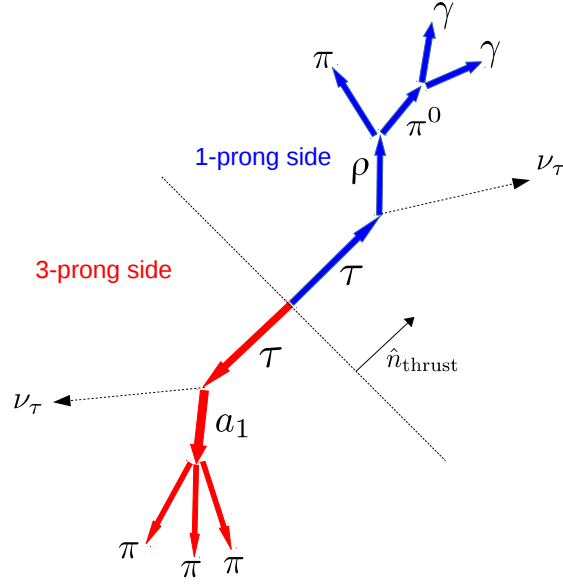


Figure 4.1: Scheme of the expected $\tau\tau$ signal event in the center of mass. The 1-prong side is defined by one charged pion and two photons from a π^0 and it goes through the intermediate ρ resonance. The decay into 3 charged pions without any π^0 on the 3-prong side passes through the $a_1(1260)$ resonance.

The presence of the π^0 could therefore affect the reconstruction of the tau momentum, but it is not expected to contribute directly in the reconstruction of primary vertices and decay lengths.

From PDG [11], the branching ratio for the decay $\tau^- \rightarrow \pi^- \pi^+ \pi^- \nu_\tau$ is $\mathcal{B}_{3\text{-prong}} = (9.02 \pm 0.05)\%$, with the pions predominantly coming from the $a_1(1260)$ vector resonance which goes into a $\rho^0 \pi$ intermediate state in S-wave. It is worth noticing that not all the a_1 decays contribute to the 3-prong channel, as the chain $a_1 \rightarrow \pi^0 \rho (\rightarrow \pi \pi^0)$ is possible as well. The latter a_1 decay mode represents a possible background contribution for the 1-prong side with one additional π^0 in the final state.

Being the τ pair production cross section at the $\Upsilon(4S)$ energy $\sigma(e^+e^- \rightarrow \tau^+\tau^-) = 0.919$ nb, for the $\tau(\rightarrow \rho\nu) \times \tau(\rightarrow \pi\pi\pi\nu)$ channel we expect:

$$\sigma_{\text{sgn}} = 2 \sigma(e^+e^- \rightarrow \tau^+\tau^-) \mathcal{B}_{1\text{-prong}} \mathcal{B}_{3\text{-prong}} = (42.3 \pm 0.3) \text{ pb} \quad (4.1)$$

Equivalent to about 42300 signal events produced for each fb^{-1} of integrated luminosity.

4.1.1 Background sources

$\tau\tau$ background

A fraction of the total background will come from τ pairs decaying with different topology. Regarding the 1-prong side, the main background sources coming from τ

decays are:

- $\tau^- \rightarrow \pi^- 2\pi^0 \nu_\tau$ where one π^0 is not reconstructed. This channel has $(1.04 \pm 0.07)\%$ branching ratio and can be partially reduced requiring selections on invariant mass $M_{1\text{-prong}}$ around the ρ -meson peak and rejecting events with additional photons on the 1-prong side.
- $\tau^- \rightarrow \pi^- \nu_\tau$ with a fake reconstructed π^0 . It has a $(10.82 \pm 0.05)\%$ branching fraction; can be suppressed by requirements on invariant mass $M_{1\text{-prong}}$ and on π^0 momentum.
- $\tau^- \rightarrow \ell^- \bar{\nu}_\ell \nu_\tau$ ($\ell = e, \mu$) with a fake π^0 and the lepton misidentified as a pion. This decay has a total branching ratio $\approx 35.21\%$ and can be rejected using cuts on $M_{1\text{-prong}}$ and π^0 momentum, but also exploiting the different decay kinematics, with two neutrinos instead of one in the final states. In addition, some particle ID requirements can be used for discriminating between leptons and pions.
- $\tau^- \rightarrow K^- \pi^0 \nu_\tau$ where the K^- takes the place of the π^- (branching ratio $\approx 0.43\%$). Using a pion mass hypothesis, the hadron energy would be underestimated for such events. They can also be rejected with cuts on $M_{1\text{-prong}}$ or using the particle ID on the 1-prong charged pion.

Regarding the 3-prong side, the dominant background source from τ decay are:

- $\tau^- \rightarrow \pi^- \pi^+ \pi^- \pi^0 \nu_\tau$ where the π^0 is not reconstructed, having a branching ratio $(4.49 \pm 0.05)\%$. As it doesn't come from a_1 resonance, it can be reduced looking at the 3-prong invariant mass $M_{3\text{-prong}}$. Furthermore, this background can be reduced by rejecting events with additional photons on the 3-prong side.
- $\tau^- \rightarrow K^- \pi^+ \pi^- \nu_\tau$ and $\tau^- \rightarrow K^- K^+ \pi^- \nu_\tau$, with a total branching ratio $\approx 0.44\%$. The yield of these events can be reduced with particle ID cuts discriminating K from π .

Light quarks

The scattering processes $e^+e^- \rightarrow q\bar{q}$ with $q = u, d, s, c$ can produce final states similar to the signal ones with π s and K s. The total cross section for this type of background is $\sigma(e^+e^- \rightarrow q\bar{q}) = 3.65 \text{ nb}$. This is potentially the only irreducible background, however can be excluded studying the event kinematic and shape. The main difference respect to the signal is the absence of neutrinos, which means different missing momentum and energy distributions. Another distinction comes from the shape of the event: while signal is originated by two taus back-to-back in the center of mass, at the Belle II energy, $q\bar{q}$ events are less jet-like.

Table 4.1: List of the processed datasets collected at the $\Upsilon(4S)$ energy which were used for the analysis. The 2019 datasets are all processed under the proc11 scheme, while the 2020 experiments are split into prompt processing (called buckets). The uncertainty indicated for the integrated luminosity is only statistical.

Experiment name	Processing scheme	Release	Integrated luminosity [fb^{-1}]
Exp 7	proc11	04-02-02	0.4255 ± 0.0003
Exp 8	proc11	04-02-02	4.5974 ± 0.0009
Exp 10	proc11	04-02-02	3.7413 ± 0.0011
Exp 12	bucket9	04-02-02	2.7687 ± 0.0011
Exp 12	bucket10	04-02-02	10.3611 ± 0.0021
Exp 12	bucket11	04-02-04	12.6871 ± 0.0023
Total integrated luminosity			34.581 ± 0.004

Other backgrounds

Other background sources to be taken into account for the analysis are the low multiplicity processes with 4 particles in the final state. Also the $B\bar{B}$ events will be included in the Monte Carlo samples, though they are unlikely to be a major background source due to their high multiplicity.

Because of its high cross section, also the (radiative) Bhabha $e^+e^- \rightarrow e^+e^-(\gamma)$ and the two photons $e^+e^- \rightarrow e^+e^-e^+e^-$ backgrounds will be inserted in the MC samples, although they have a very different topology from $\tau\tau$ events.

4.2 Dataset

The present analysis is performed on Belle II data and uses the a MC sample from the official Belle II production as reference.

4.2.1 Data samples

We use the data acquired during the full 2019 data taking period (2019a/b/c) and the March-July period of 2020 (2020a/b) at the $\Upsilon(4S)$ center of mass energy (see table 4.1). All runs marked as *good* are included. The luminosity is estimated from Bhabha, the uncertainty reported is only statistical, a systematic of 1% must be added. The total number of signal events produced in such a sample, from (4.1), is expected to be $N_{\text{sgn}} = (1.46 \pm 0.01) 10^6$ events.

4.2.2 Monte Carlo samples

Regarding simulation, MC13a run-independent productions are used. The complete list of the samples with the corresponding integrated luminosity and the production cross section is summarized in table 4.2. The cross section reported for the Bhabha

Table 4.2: Complete list of the MC13a run-independent production used in the analysis. For every process the production cross section at $\sqrt{s} = 10.58$ GeV is provided. Note that the cross section for the (radiative) Bhabha process $e^+e^- \rightarrow e^+e^-(\gamma)$ takes into account the selection criteria $p_e > 0.5$ GeV/c and e in ECL acceptance, applied at the generator level.

Process	Cross section [nb]	Integrated luminosity [fb ⁻¹]
$e^+e^- \rightarrow \tau^+\tau^-$	0.919	200
$e^+e^- \rightarrow u\bar{u}$	1.59	200
$e^+e^- \rightarrow d\bar{d}$	0.40	200
$e^+e^- \rightarrow s\bar{s}$	0.36	200
$e^+e^- \rightarrow c\bar{c}$	1.30	200
$e^+e^- \rightarrow \Upsilon(4S) \rightarrow B^+\bar{B}^-$	0.54	100
$e^+e^- \rightarrow \Upsilon(4S) \rightarrow B^0\bar{B}^0$	0.51	100
$e^+e^- \rightarrow e^+e^-(\gamma)$	73.3	10
$e^+e^- \rightarrow e^+e^-e^+e^-$	39.7	100
$e^+e^- \rightarrow e^+e^-\mu^+\mu^-$	18.9	100
$e^+e^- \rightarrow \mu^+\mu^-(\gamma)$	1.148	50
$e^+e^- \rightarrow e^+e^-\pi^+\pi^-$	1.84	10

process accounts for selection requirements at the generator level. All the batches were produced at the $\Upsilon(4S)$ energy with default conditions using the software release 04-00-03, except for the $e^+e^- \rightarrow e^+e^-\pi^+\pi^-$ sample, produced with release 04-02-01. The input lifetime for the τ pair sample is set to the PDG value $c\tau_\tau = 87.03$ μm .

4.3 Event selection

All the datasets are first analyzed through the `basf2` software in order to preselect events compatible with the $\tau \rightarrow \rho\nu \times \tau \rightarrow 3\nu$ topology. At this level only some loose cuts are applied, mainly focused to select the general event topology. Afterwards, optimized cuts are applied studying the MC distributions of signal and background.

4.3.1 Preselection

The preselection is applied firstly on single objects, e.g. charged tracks, ECL clusters, and then on the global event topology, exploiting the separation of the 1-prong and 3-prong taus into different hemispheres.

Tracks

From the perspective of the analyst, each track is defined by a set of 6 parameters:

- the coordinates \vec{x} of the POCA (point of closest approach to the origin)
- the momentum vector \vec{p} computed at the POCA

In some cases it is useful to express the coordinates of the POCA with respect to the nominal position of the interaction point \vec{IP} , as $\vec{dx} = \vec{x} - \vec{IP}$.

Because of the short τ lifetime, tracks coming from a prompt tau decay have a lower impact parameter compared to beam background, decay from long lived particles and material interactions. Therefore, in order to select tracks coming from tau and reduce background, tracks with large transverse (dr) or longitudinal (dz) impact parameter are excluded from the analysis. Taking as reference a 100 fb^{-1} MC13b $e^+e^- \rightarrow \tau^+\tau^-$ sample with run-dependent beam background $\text{BG} \times 1$ and loose preselection $|dz| < 20 \text{ cm}$ and $dr < 20 \text{ cm}$, the symmetric cut

$$-3 \text{ cm} < dz < 3 \text{ cm} \quad \text{and} \quad dr < 1 \text{ cm} \quad (4.2)$$

leads to a 96.78% signal efficiency with 73.33% background rejection [30]. Where the signal is defined by all the tracks having a tau as ancestor, excluding material interactions.

Usually the τ pair selection relies more on the event topology rather than on track identification. In this particular study, anyway, we are interested only in hadronic-decaying τ s, therefore some kind of ID discrimination may be helpful. In order to keep pions and reject electrons from Bhabha, leptonic tau decays $\tau \rightarrow e\nu_e\nu_\tau$, and other low multiplicity processes, we ask the ratio between the energy E_{cluster} deposited in the ECL and the track momentum p to be lower than 0.8

$$\frac{E_{\text{cluster}}}{p} < 0.8 \quad (4.3)$$

If the variable E_{cluster} is undefined, for example when the track doesn't reach the ECL, then the default value $E_{\text{cluster}} = -1$ is set and the track is not discarded.

The cuts (4.2) and (4.3) are applied on all track objects. The event topology $\rho \times 3\pi$ requires 4 charged pions, hence we keep only the events having exactly 4 tracks passing the selection cuts and with total null electric charge. Hereafter, all the kinematics variables of the tracks are computed using a pion mass hypothesis.

π^0 reconstruction

The Belle II detector operates under severe beam conditions. As a consequence, the ECL detects many low energetic photons stemming from machine background. These photons are rejected by requiring a minimum photon energy. Concerning the event topology $\tau(\rightarrow \rho\nu) \times \tau(\rightarrow \pi\pi\pi\nu)$, an efficient $\pi^0 \rightarrow \gamma\gamma$ reconstruction is critical both to select as much $\rho \rightarrow \pi\pi^0$ decays as possible, and to veto τ backgrounds with additional π^0 s (i.e. $\pi 2\pi^0$ on 1-prong side and $3\pi\pi^0$ on the 3-prong side). At the same time a very low purity reconstruction should be avoided as it would add fake pions to the event, increasing the yields from background channels such as $\tau \rightarrow \pi\nu$ and $\tau \rightarrow \ell\bar{\nu}$.

As a reference we use the May 2020 recommendations obtained from studies on a $B\bar{B}$ MC12 sample [31]. Various selections are proposed with different efficiency

Table 4.3: Efficiency and purity for π^0 selection criteria recommendations studied from a $B\bar{B}$ MC12 sample [31]. The criteria **eff50** was chosen for the analysis.

	eff60	eff50	eff40	eff30	eff20	eff10
efficiency (%)	59.82	49.82	39.93	29.84	19.81	9.81
purity (%)	2.49	10.87	18.82	29.78	50.03	69.25

and purity (see table 4.3). We choose to adopt the selection labeled as **eff50**. The proposed cuts on photons from π^0 are:

- Number of weighted crystals in the ECL cluster: $\text{clusterNHits} > 1.5$
- Polar angle of the cluster's centroid position, with respect to the origin of the system of coordinates: $17^\circ < \text{clusterTheta} < 150^\circ$, i.e. the CDC acceptance
- A region dependent cut on the energy of the ECL cluster:
 - $E_{\text{cluster}} > 25 \text{ MeV}$ if the cluster is located in the forward or in the barrel ECL region
 - $E_{\text{cluster}} > 40 \text{ MeV}$ if the cluster is located in the backward ECL region

Hence the π^0 s in the event are reconstructed looking at the pairs of previously selected photons with the following requirement:

- Photons pair invariant mass: $105 \text{ MeV} < M_{\gamma\gamma} < 150 \text{ MeV}$

In the event topology we are looking for, the goal is to select the final state $\rho \rightarrow \pi\pi^0$ rejecting other τ decays with possible additional π^0 s. Therefore the preliminary requirement on each events is to have exactly one reconstructed π^0 .

Photons

It is important to keep record of all the photons in the event, as they carry important information. Indeed photons can be part of the total event energy and momentum, coming from ISR or FSR, radiative decays of τ , or from unreconstructed π^0 s. However, a huge number of low energy photons come from beam background, which is not properly modeled in the current MC. Thus, photons with an energy below 200 MeV are discarded and not considered at all in the analysis. Additional requirements for a calorimeter neutral cluster to be considered a candidate photon are:

- Number of weighted crystals in the ECL cluster: $\text{clusterNHits} > 1.5$
- Polar angle of the cluster's centroid position, with respect to the origin of the system of coordinates: $17^\circ < \text{clusterTheta} < 150^\circ$, i.e. the CDC acceptance
- Energy of the ECL cluster: $E_{\text{cluster}} > 200 \text{ MeV}$
- It is not a daughter of a reconstructed π^0

At this stage, all the photons that pass this selection are saved as *good* photons.

Event shape

After the selection of good tracks and good photons, event shape selection criteria are applied. Every event includes:

- 4 charged tracks
- 1 reconstructed π^0
- a list of *good* photons

All these are used for computing the variables which define the event kinematic and shape.

In the center of mass frame the two taus are back to back, and one can define two opposite hemispheres divided by the plane perpendicular to the tau direction. The decay products may be as well separated between the two hemispheres, and, in the case of 1×3 topology, assigned them to the 1-prong or to the 3-prong side.

To determine the two hemispheres, we make use of the thrust of the event, defined as

$$T = \max_{\hat{n}} \frac{\sum_i |\vec{p}_i^{\text{CMS}} \cdot \hat{n}|}{\sum_i |\vec{p}_i^{\text{CMS}}|} \quad (4.4)$$

where the index i runs over all the visible particles in the event. The unit vector \hat{n} , that maximizes the thrust value, is called thrust axis of the event. For a perfect spherical event the thrust value should be $T = 1/2$, while is $T = 1$ in case of a only two particles event, being the thrust axis aligned with the particles direction in the center of mass. The tau pairs are jet-like and are characterized by thrust value larger than $q\bar{q}$ and smaller than Bhabha. The thrust axis \hat{n} is an estimate for tau momentum direction in the CMS (see also Figure 4.1).

In order to select the topology with $\pi^0\pi^\pm$ and $\pi^\mp\pi^\pm\pi^\mp$ lying on opposite hemispheres, we look at the angle between the candidate particle's momentum in the center of mass and the thrust axis of the event, computed using all the tracks, the π^0 and the *good* photons:

$$\cos \varphi_i = \vec{p}_i^{\text{CMS}} \cdot \hat{n}$$

We then select the events where the sign of $\cos \varphi_{\pi^0}$ is the same as of one charged track and opposite to the other 3 tracks. The two hemispheres are respectively labeled as 1-prong and 3-prong and the *good* photons are assigned to either, based on their $\cos \varphi_i$ sign.

To summarize, all the events passing the selection above include the following candidates divided between the two sides:

- 1-prong side
 - 1 charged track
 - 1 reconstructed π^0
 - *good* photons assigned to 1-prong side

- 3-prong side
 - 3 charged tracks
 - *good* photons assigned to 3-prong side

3-prong vertex fit

The last preselection applied tests the compatibility of the 3-prong tracks with the products of a decay. For this purpose the `TreeFitter` module (see section 2.3.4) is used making a single vertex fit of the 3 candidate pions. We retain all the events where the decay fit succeeds with a chi-square probability greater than 0.001.

The `TreeFitter` also returns the optimized values for the total 3-prong momentum and the vertex position, which will be used for the reconstruction fit.

4.3.2 Data/MC agreement

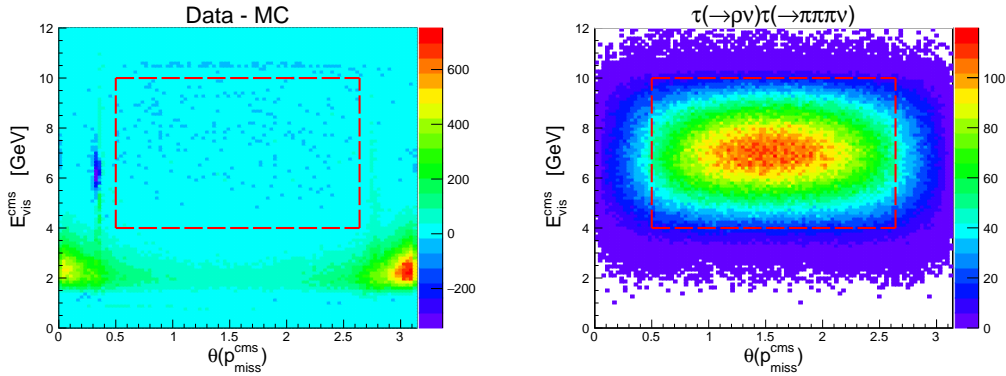
The MC events are weighted to the data luminosity. About 226 k signal events $\tau(\rightarrow \rho\nu)\tau(\rightarrow \pi\pi\pi\nu)$ pass the preselection, with a 15.5% efficiency and a 42.1% purity, defined as the fraction of signal events:

$$\mathcal{P} = \frac{N_{\text{sgn}}}{N_{\text{tot}}}$$

The number of data events passing the preselection exceeds by a factor 1.48 the total MC yields. The discrepancy is probably due to the part of beam background not completely described by MC13, and to the two-photons events for which there are not implemented generators. Furthermore, as pointed out in section 4.2.2, the Bhabha MC sample does not cover the whole phase space, favoring events in which the electrons and positrons are within the detector acceptance. On the other side, on data, the full phase space is populated, so more low momentum Bhabha electrons could in principle pass the preselection.

The visible energy and momentum, E_{vis} and \vec{p}_{vis} , are computed including all the candidates in the event (charged tracks, reconstructed π^0 and *good* photons) either in the laboratory or in the center of mass frame. The missing momentum \vec{p}_{miss} is given subtracting \vec{p}_{vis} from the nominal total momentum of the beams \vec{p}_{lab} . These variables can be exploited for improving the data/MC agreement. Indeed, we expect the radiative and the two photons backgrounds to be characterized by missing momentum \vec{p}_{miss} close to the beam axis. Such hypothesis is confirmed from the scatter plot in Figure 4.2a, which shows two big excesses in the data–MC difference at low visible energies and with the missing momentum pointing along the beams. Both variables here are computed in the center of mass frame so that $\theta(p_{\text{miss}}^{\text{CMS}})$ distribution is symmetric around $\pi/2$.

In Figure 4.2b the distribution of the MC13 signal events $\tau(\rightarrow \rho\nu)\tau(\rightarrow \pi\pi\pi\nu)$ is shown on the same scatter plot. In this case $E_{\text{vis}}^{\text{CMS}}$ and $\theta(p_{\text{miss}}^{\text{CMS}})$ distributions are peaked around 7 GeV and $\theta = \pi/2$ respectively.



(a) Number of data events subtracted by the total MC13a, after preselection. (b) Signal events from MC13a simulation passing the event preselection.

Figure 4.2: Scatter plots of the total visible energy of the event $E_{\text{vis}}^{\text{CMS}}$ against the missing momentum's polar angle $\theta(p_{\text{miss}}^{\text{CMS}})$, both calculated in the center of mass frame. The red dashed line defines the signal region window.

From these two plots we can define a signal region containing the majority of $\tau(\rightarrow \rho\nu)\tau(\rightarrow \pi\pi\pi\nu)$ events and excluding areas with evident data–MC discrepancies. The selection region is defined by:

- $1.5 < \theta(p_{\text{miss}}^{\text{CMS}}) < 2.64$
- $4 \text{ GeV} < E_{\text{vis}}^{\text{CMS}} < 10 \text{ GeV}$

Such a window keeps 85% of the signal events, rejecting mostly the ones with missing momentum pointing forward or backward in the CMS. The above selection is necessary for having a good data-MC overall agreement. In future, with a more reliable background simulation, one may avoid losing 15% of the initial statistics.

To further remove Bhabha background, the thrust value distribution can be used as well: events like $e^+e^- \rightarrow e^+e^-$ should have a thrust close to 1, while we know that tau pair events have a lower thrust due to the presence of neutrinos. In Figure 4.3 the excess in data is evident in the high thrust region, where the Bhabha background gives the dominant contribution. Therefore we set an additional cut as

- $\text{thrust} < 0.99$

After these cuts there are 361254 data events left, with an overall data/MC ratio of 1.02. At this stage, the signal purity and efficiency are $\mathcal{P} = 54.3\%$ and $\mathcal{E} = 13.2\%$. The tau pair background contributes to the 32.4% of the total events, while the $q\bar{q}$ background is equivalent to 12.6% of the sample. All the other backgrounds types, including Bhabha and two photons events, sum up to 0.6%.

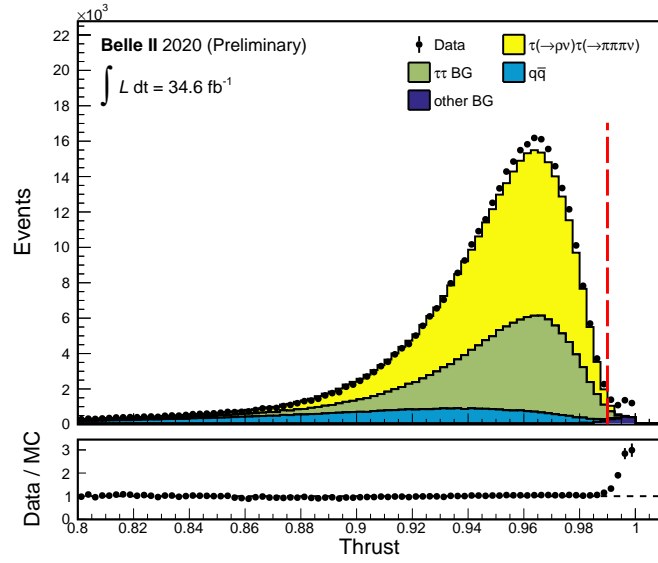


Figure 4.3: Superimposed thrust value distribution of data and Monte Carlo MC13a after the preselection for the $\tau(\rightarrow \rho\nu)\tau(\rightarrow \pi\pi\pi\nu)$ event topology and the rectangular cut shown in figure 4.2. The MC is scaled to the data integrated luminosity and the different contributions are divided in signal and background categories and stacked. On this variable the cut $\text{thrust} < 0.99$ is applied in order to reduce Bhabha background and therefore improve the agreement between data and MC. As evident from the lower pad plot, the excluded region presents an excess in the data.

4.3.3 Optimization cuts

We want to increase the purity of the sample and at the same time maintain an high signal yield. To this end, a series of cuts is performed on variables having a good signal background separation. The cuts are chosen so that they maximize a figure of merit defined as the product of signal efficiency \mathcal{E} and signal purity \mathcal{P} . Up to a constant, such a figure of merit can be written as

$$\mathcal{E} \cdot \mathcal{P} \propto \frac{N_{\text{sig}}^2}{N_{\text{tot}}} \quad (4.5)$$

which is equivalent to maximizing the figure of merit $N_{\text{sig}}/\sqrt{N_{\text{sig}} + N_{\text{bkg}}}$. Note that the background from τ decays in the optimization is counted in N_{bkg} as the non-tau background processes.

1-prong invariant mass

The first variable we look at is the invariant mass of the π and π^0 candidates on the 1-prong side. From the distribution shown in Figure 4.4 the ρ mass peak is evident. The maximization of $\mathcal{E} \cdot \mathcal{P}$ defines the optimized lower and upper cuts:

- $0.5 \text{ GeV} < M_{\text{inv}}(1\text{-prong}) < 1.3 \text{ GeV}$

with a resulting signal efficiency $\mathcal{E} = 12.4\%$ and a purity $\mathcal{P} = 60.7\%$.

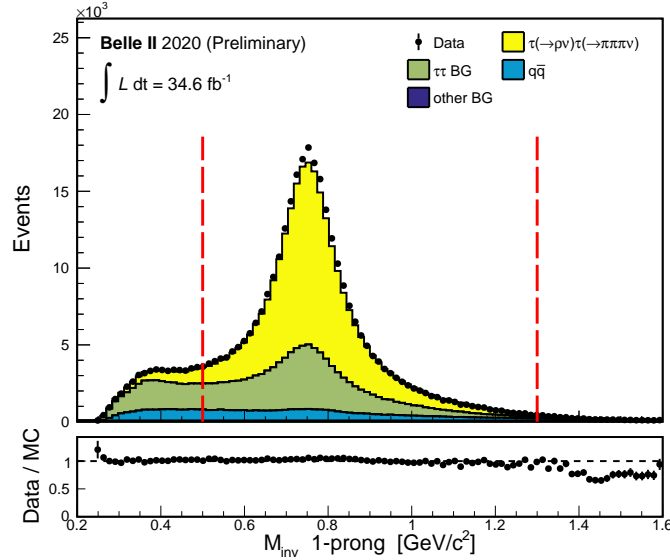


Figure 4.4: Distribution of 1-prong π and π^0 invariant mass for data and MC13a after preselection and the cuts of section 4.3.2. The different MC contributions are divided between signal and background categories and are stacked. Note that the MC are scaled to the data luminosity but no trigger efficiency correction has been applied.

The tau pair background distribution presents a peak on the ρ mass as well. This can be explained by the events with the a_1 resonance decaying as $\rho^\pm\pi^0$, where the branch $\rho^\pm \rightarrow \pi^\pm\pi^0$ is considered as signal, and the other π^0 is not reconstructed.

3-prong invariant mass

After the cut on $M_{\text{inv}}(1\text{-prong})$, a similar approach is repeated for the invariant mass distribution of the 3 charged π on the 3-prong side. In this case, the signal distribution is peaked at ≈ 1.1 GeV, while the dominant $\tau\tau$ background is slightly displaced at lower masses. The major background of this type comes from the decay $\tau \rightarrow \pi\pi\pi\pi^0$ with the π^0 unidentified.

Due to the broader width of the signal, the separation is not as good as it was for 1-prong invariant mass, anyway, the $\tau\tau$ background tail at low M_{inv} can be rejected losing only few signal events. The optimized cut window, highlighted in Figure 4.5 by the red dashed lines, is:

- $0.8 \text{ GeV} < M_{\text{inv}}(3\text{-prong}) < 1.6 \text{ GeV}$

Selecting this region we obtain an efficiency $\mathcal{E} = 12.3\%$ and a purity $\mathcal{P} = 65.8\%$.

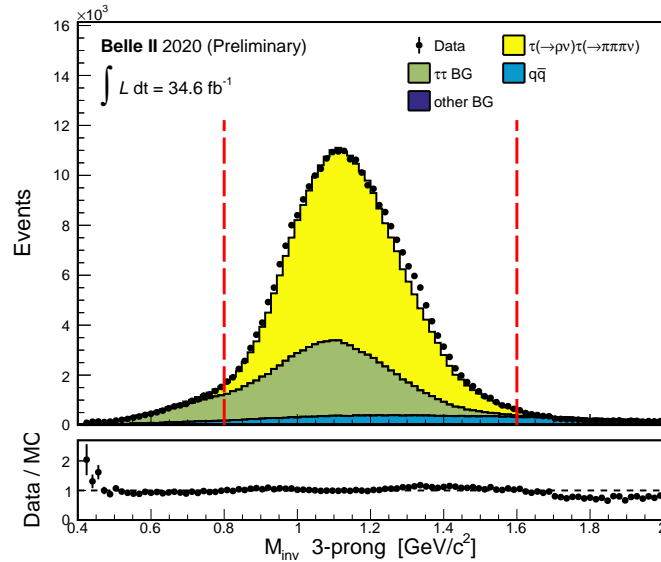


Figure 4.5: Distribution of 3π invariant mass on the 3-prong side for data and MC13a after the selection on the 1-prong invariant mass. The different MC contributions are stacked. The MC is scaled to the data luminosity but no trigger efficiency correction has been applied. The cuts which maximize the $\mathcal{E} \cdot \mathcal{P}$ figure of merit are indicated by the vertical dashed lines.

π^0 momentum

The background with a fake π^0 on the 1-prong side can be rejected looking at the kinematic of the reconstructed π^0 . Pairs of beam background photons that by chance

pass the invariant mass selection for π^0 s, are expected to populate the lower part of the energy spectrum, respect to real π^0 from a $\tau \rightarrow \rho\nu$ decay. Indeed, the π^0 momentum distribution in Figure 4.6 shows a narrow peak at $p_{\pi^0} \approx 100$ MeV for the backgrounds, while the signal has a maximum at $p_{\pi^0} \approx 800$ MeV and a long tail at high momenta. Therefore, maximizing $\mathcal{E} \cdot \mathcal{P}$, a lower π^0 momentum cut is imposed:

- $p_{\pi^0} > 200$ MeV

This brings to a purity $\mathcal{P} = 71.8\%$, while the signal efficiency is reduced to $\mathcal{E} = 11.7\%$.

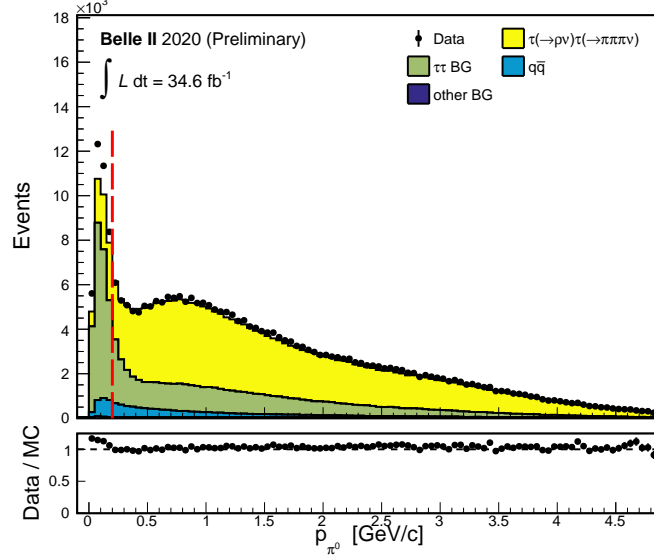


Figure 4.6: Momentum of the reconstructed π^0 on the 1-prong side. Data and MC13a distributions are shown after preselection and optimized cuts on the two sides invariant masses. The MC contribution are stacked and each is scaled to the data integrated luminosity. The dashed line on the plot indicates the chosen p_{π^0} threshold.

4.4 Candidate reconstruction

To ensure using well reconstructed tracks, we require that each charged track in the event has at least one hit in the PXD:

- $\forall \text{track} : N_{\text{Hits}}(\text{PXD}) \geq 1$

Together with the selection described in the previous section, this leads to a data sample of 181957 events, and a data/MC ratio of 97.4. A lower data yield is expected as the MC samples don't account for the trigger efficiency. The signal purity is $\mathcal{P} = 72.8\%$ and the different background contaminations are, in descending order, $\tau\tau$ background (21.8%), $q\bar{q}$ (5.3%) and low multiplicity (0.1%). The signal efficiency is reduced to $\mathcal{E} = 9.3\%$.

4.4.1 Tau momentum reconstruction

A precise test of the event topology can be made through the full kinematic reconstruction. We therefore calculate the minimum of F_{kin} from (3.9) as a function of the unknown tau momenta. The known parameters are the measured hadron momenta and energies:

$$\begin{aligned}\vec{p}_{h_{1\text{-prong}}} &= \vec{p}_{\pi} + \vec{p}_{\pi^0} & E_{h_{1\text{-prong}}} &= E_{\pi} + E_{\pi^0} & \text{1-prong side} \\ \vec{p}_{h_{3\text{-prong}}} &= \sum_{i=1}^3 \vec{p}_{\pi_i} & E_{h_{3\text{-prong}}} &= \sum_{i=1}^3 E_{\pi_i} & \text{3-prong side}\end{aligned}$$

In Figure 4.7, the distribution of the minimum value of F_{kin} found in the event per event minimization is shown. This variable can be used for a further background rejection. As in section 3.4.1, to ensure that all the constraints of F_{kin} are close to zero, we want to set an upper cut on the minimum value. However, an optimization based on the figure of merit (4.5) would lead to select almost all events, as signal events are present on both peaks of Figure 4.7. Therefore, we now maximize the purity only, since the efficiency has already been kept high by the previous cuts. The maximum of purity is $\mathcal{P} = 78.5\%$, obtained selecting:

- $\min(F_{\text{kin}}) < 5 \times 10^{-5}$

with the efficiency becoming $\mathcal{E} = 8.2\%$.

Because of the constrain on the total energy and momentum, the minimum of F_{kin} is sensible to undetected final states in the event. After the cut on $\min(F_{\text{kin}})$, $\tau\tau$ background with two π^0 s on the 1-prong side is reduced by 40%, while the events with an additional π^0 on the 3-prong side are reduced by just 12%, since the unreconstructed π^0 is expected to have a lower energy spectrum in the 3-prong case. In addition, the scatter plot in Figure 4.8 shows the correlation between the missing energy in the laboratory frame and the minimum value of F_{kin} for the signal MC events. The variable δE^{lab} is computed as the difference between the nominal beam energy and the initial generated energies of the two τ s. The region excluded by the cut, contains δE^{lab} values close or greater than 1 GeV. The energy loss can be attributed to ISR/FSR photons.

After the cut we are left with 149330 data events with a data/MC ratio still of 97.9%. Among the different background components, the $\tau\tau$ represents now a 19.3% of the total and the $q\bar{q}$ contamination is reduced to 2.1%. Other background contributions are negligible. In table 4.4 the major fractions of $\tau\tau$ background are classified depending on the corresponding tau decay mode. As expected, the dominant contributions come from events with an unreconstructed π^0 on either side, about 59% of the total. Another 25% is formed by events where one (or more) K takes the place of a π , and since the pion mass hypothesis is assumed for all charged tracks, it follows that in these cases the hadron's energy is systematically underestimated. However, we didn't apply any cut focused on removing such events.

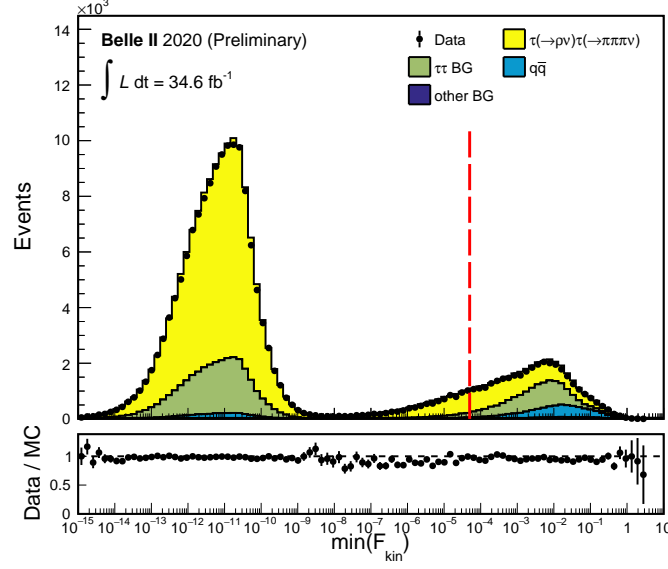


Figure 4.7: Data and MC13a stacked distributions of the minimum values found for the function F_{kin} calculated on each event. The Monte Carlo are weighted to the data luminosity and no trigger efficiency correction has been applied. The vertical dashed line highlights the upper cut which maximizes the signal purity \mathcal{P} .

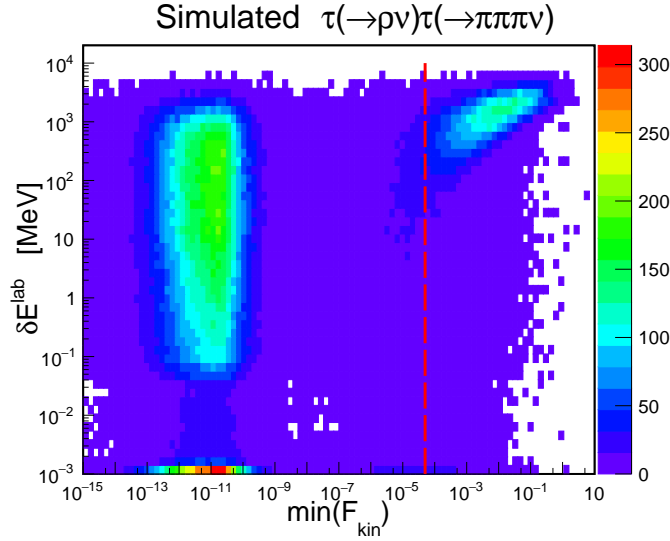


Figure 4.8: Scatter plot of the missing initial $\tau\tau$ energy at the generator level against the minimum value of F_{kin} . Only signal MC events are shown. The red dashed line corresponds to the cut $\min(F_{\text{kin}}) < 5 \times 10^{-5}$ which maximizes the signal purity. The excluded region (right) contains events with δE^{lab} in average higher than in the retained region, while in the left region the events are split between a flat bunch of a few MeV and a narrow strip below 1 keV of energy loss.

Table 4.4: $\tau\tau$ background divided into its different contributions considering the 1-prong (columns) and 3-prong (rows) decay. Only decays that contribute to more than 1% of the total $\tau\tau$ background have been included.

	$\tau \rightarrow \rho\nu$	$\tau \rightarrow \pi\pi^0\pi^0\nu$	$\tau \rightarrow K\pi^0\nu$	$\tau \rightarrow \pi\nu$	$\tau \rightarrow \mu\nu\nu$	$\tau \rightarrow \pi\pi^0\gamma\nu$
$\tau \rightarrow \pi\pi\pi\nu$	sgn	27%	5%	3%	2%	1%
$\tau \rightarrow \pi\pi\pi\pi^0\nu$	29%	3%				
$\tau \rightarrow K\pi\pi\nu$	15%					
$\tau \rightarrow KK\pi\nu$	5%					
$\tau \rightarrow \rho\nu$	1%					

4.4.2 Tau Lifetime reconstruction

The selected sample is finally used for the decay vertex reconstruction. In this case the function to be minimized is $F = F_{\text{kin}} + F_{\text{vertex}}$ (see (3.9) and (3.11)) where the free parameters are the momenta of the two taus, $\vec{p}_{1\text{-prong}}$, $\vec{p}_{3\text{-prong}}$, their decay lengths $\ell_{1\text{-prong}}$, $\ell_{3\text{-prong}}$, the IP coordinates IP_x , IP_z and the distance L_π between the POCA and the secondary vertex for the 1-prong charged pion. Energies and momenta are measured in GeV, while distances are in μm , so the scale factor is set to $S = 0.01$.

$\vec{\delta}_{1\text{-prong}}$ are the POCA coordinates of the 1-prong charged pion and the unit vector $\vec{n}_{\pi_{1\text{-prong}}}$ is along the direction of the 1-prong charged pion momentum. The decay vertex position $\vec{v}_{3\text{-prong}}$ on the 3-prong side was previously fitted by the **TreeFitter**.

The minimization succeeds for 148682 data events (99.6%) and for the 99.7% of the luminosity-weighted Monte Carlo. For these events, the proper decay time for the 3-prong tau is computed as:

$$t = \ell_{3\text{-prong}} \frac{m_\tau}{|\vec{p}_{3\text{-prong}}|c}$$

Where the tau mass value $m_\tau = 1.777 \text{ GeV}$ has been used.

The obtained τ proper time distribution is shown in Figure 4.9. Both the signal and $\tau\tau$ background distributions present an exponential shape for large proper time, while at low and negative values of ct the resolution function is dominant. The $q\bar{q}$ background distribution is peaked at zero though it has an asymmetric tail for positive times, originated by the $c\bar{c}$ component. The data/MC ratio shows an unexpected excess around 50% in data between -600 fs and -300 fs .

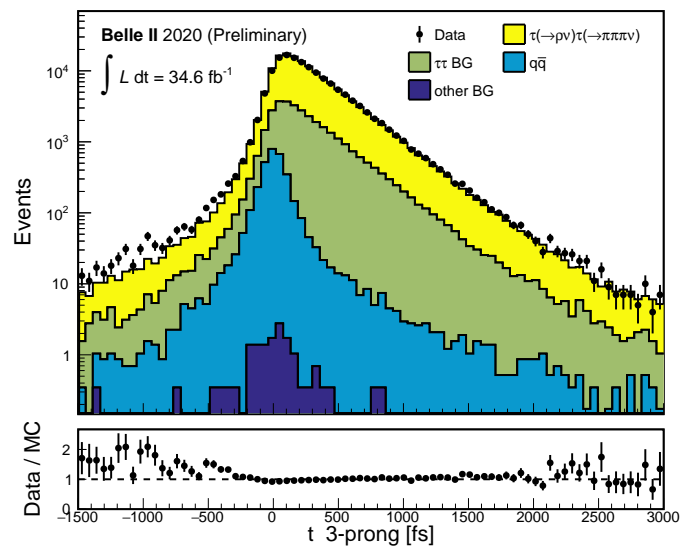


Figure 4.9: Data and MC13a distributions for the reconstructed decay proper time of the τ on the 3-prong side. The MC are stacked and scaled to the data luminosity. The lower pad shows an excess on data between -600 fs and -300 fs.

Chapter 5

τ lifetime extraction

The reconstruction method developed in chapter 3 has been exploited in chapter 4 in order to obtain the proper decay time distribution. In the topology selected for the reconstruction one τ decays to a ρ resonance and a neutrino, and the other to 3 charged pions and a neutrino. In this chapter, the τ lifetime is extracted from the proper time distribution of the τ lepton decaying to 3-prong.

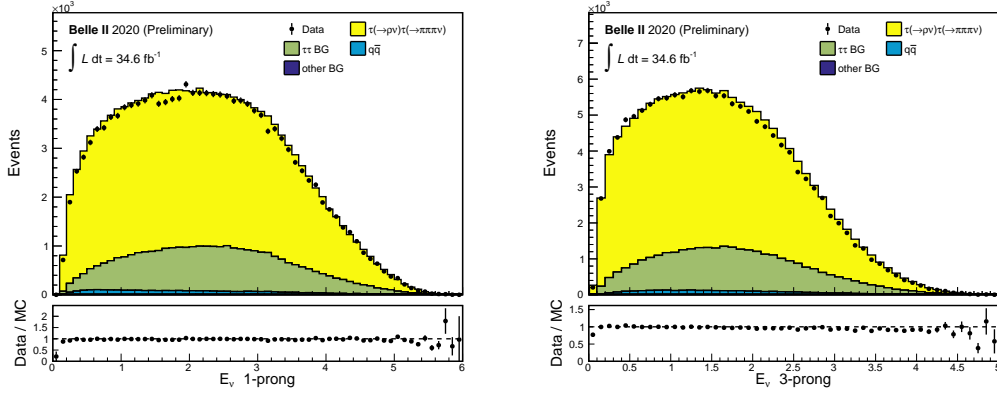
5.1 Reconstructed parameters

The reconstruction of section 4.4.2 leads to 12 optimized variable. Beyond the tau proper decay time, other variables may be of interest for physical analysis or can be used to control the method's performance.

5.1.1 Tau candidate kinematics

From the reconstructed tau pair kinematic distributions in the laboratory frame, the two neutrino momenta can be extracted subtracting the total measured momentum of the final state hadrons. As shown in Figure 5.1, the neutrino energies are reconstructed with a good data/MC agreement on both sides, despite MC don't consider the trigger efficiency. The comparison between the true and the reconstructed tau momentum vectors, was already performed in section 3.4 on a pure $\tau(\rightarrow \pi\nu)\tau(\rightarrow \pi\pi\pi\nu)$ signal sample without any selection cut. Similar results are expected for the neutrino momenta as well, with the two-fold ambiguity solved by the introduction of the vertex constraints.

The knowledge of both tau and neutrino momenta, can be exploited to calculate the decay matrix elements, which could be sensible to new physics contributions. For instance, as shown by [32], one can set limits on $g - 2$ anomaly and electric dipole moment of τ , putting further constraints on beyond SM physics.



(a) Reconstructed energy of the ν_τ candidate on 1-prong side. (b) Reconstructed energy of the neutrino from the 3-prong tau decay.

Figure 5.1: Tau-neutrino energies computed from the measured hadronic final states and from the tau momenta, obtained through the full reconstruction method. Different MC contributions are stacked. $\tau\tau$ events are distinguished between the signal topology targeted in the reconstruction and the residual of other tau pair decays, mainly with an additional unidentified pion. The rest, formed by continuous $q\bar{q}$ and $B\bar{B}$ background, represent about 2% of the total MC yield.

5.1.2 Interaction Point

The IP position is a run-dependent variable, i.e. its (nominal) value varies for each run. Since the sample analyzed contains data collected during ≈ 2200 good runs from 4 different run periods (see table 4.1), IP_x and IP_z distributions are expected to change many times in the whole data set. Instead, the MC used are run-independent, meaning that parameters such as IP position and beam energies are fixed. In order to compare data and MC for the reconstructed primary vertex coordinates IP_x , IP_z , one can look at the difference with the nominal position. Such variable is plotted for IP_x in Figure 5.2, both in linear (5.2a) and logarithmic (5.2b) scale.

The distribution on data appears to be slightly wider than the total MC. Indeed, restricting to the range $(-200 \mu\text{m}, 200 \mu\text{m})$, the standard deviation of the $(IP_x^{\text{rec}} - IP_x^{\text{nom}})$ distribution is $48.6 \mu\text{m}$ for the data and $44.3 \mu\text{m}$ for the total MC. From Figure 5.2a also the shapes of the two distributions look different. These differences can be ascribed to a small mismatch among the actual and the simulated IP horizontal size.

As the logarithmic plot 5.2b shows, both data and MC present long non-Gaussian tails. However, the true IP_x should be approximately Gaussian distributed, so the events in the tails are clearly an excess. Since they are reproduced by the MC, they cannot be due to a wrong nominal IP_x in the data. Then, the only explanation of such tails is a failure in the reconstruction procedure. Since a bad IP_x^{rec} would imply a bad reconstruction also for the decay lengths, events in the tails of 5.2b are discarded. A conservative cut is chosen at about 10 standard deviations from the nominal position:

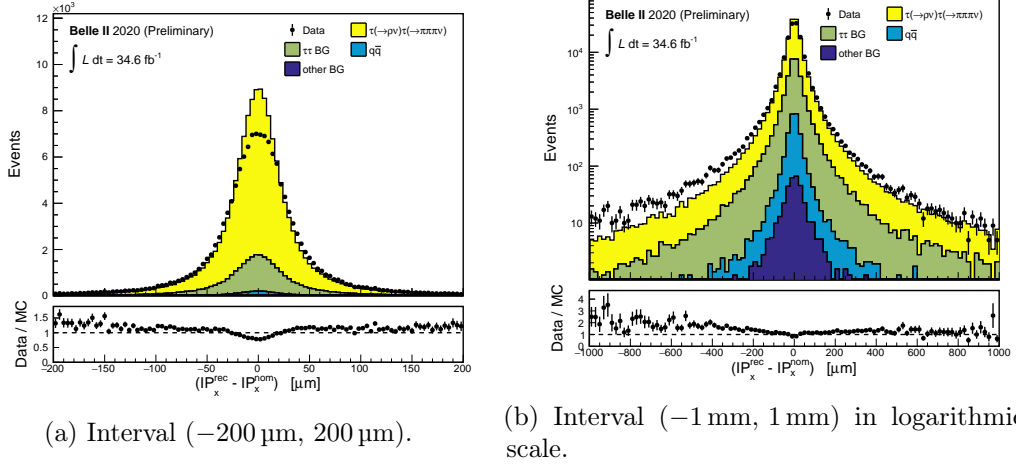


Figure 5.2: Two different scales for the distribution of IP_x^{rec} , the reconstructed x coordinate of primary vertex. To bypass the fact that the IP position is a run-dependent variable and its changing is not reproduced in the MC, the difference with the run by run nominal value IP_x^{nom} is plotted instead. The MC and data distributions are slightly different, but both are centered around zero.

- $|\text{IP}_x^{\text{rec}} - \text{IP}_x^{\text{nom}}| < 500 \mu\text{m}$

This selection doesn't introduce any sensible bias on the mean generated decay time.

Unfortunately, it is not possible to compare data and MC for the IP_z position, since in a large fraction of runs the IP_z^{nom} is systematically displaced respect to the mean value of IP_z^{rec} . Therefore the distribution $\text{IP}_z^{\text{rec}} - \text{IP}_z^{\text{nom}}$ is of no utility in the present processed dataset and the IP_z resolution can be studied only on MC. A correction of the IP_z^{nom} estimation would be helpful in order to pass a plausible initial value for the minimization of F .

5.2 Resolution function

The proper decay time distribution is in general given by the convolution of an exponential distribution with a proper time resolution, not known a priori. For an ideal case, the resolution is a Dirac delta-function, but in general it will contain miscellaneous contributions from the detector response and from the reconstruction method, which cannot be modeled from first principles. These effects should be all reproduced in the MC simulated events, where the true value of the proper time is known at the generator level. Hence the resolution function is studied on the reconstructed MC sample, with the cuts defined in chapter 4 and the additional condition $|\text{IP}_x^{\text{rec}} - \text{IP}_x^{\text{nom}}| < 500 \mu\text{m}$ motivated above.

5.2.1 Resolution on signal

The difference between the reconstructed proper time $t^{\text{rec}} = \lambda_{\tau}^{\text{rec}} m_{\tau} / |\vec{p}_{\tau}^{\text{rec}}|c$ and the truth-matched t^{gen} is computed for each tau pair event. At first, following the conventions of chapter 4, we distinguish among pure signal $\tau(\rightarrow \rho\nu)\tau(\rightarrow \pi\pi\pi\nu)$ events and other $\tau\tau$ decays, both having well defined t^{rec} and t^{gen} .

Two different parametrizations have been considered. The first is a linear combination of 3 Gaussians, while the second one is a function ad hoc for the proper time resolution at the previous Belle experiment. They are tested on the $\tau\tau$ MC sample passing the selection cuts, correspondent to a 200 fb^{-1} integrated luminosity.

Three Gaussians

A binned maximum likelihood fit is performed on the $\Delta t = t^{\text{rec}} - t^{\text{gen}}$ distribution. The probability density function (pdf) is a linear combination of 3 Gaussian distributions:

$$p(\Delta t; \mu_1, \sigma_1, \varepsilon, \mu_2, \sigma_2, \delta, \mu_3, \sigma_3) = (1 - \varepsilon - \delta) \mathcal{N}(\Delta t; \mu_1, \sigma_1) + \varepsilon \mathcal{N}(\Delta t; \mu_2, \sigma_2) + \delta \mathcal{N}(\Delta t; \mu_3, \sigma_3) \quad (5.1)$$

where $\mathcal{N}(\Delta t; \mu_i, \sigma_i)$ is a normalized Gaussian distribution of mean μ_i and standard deviation σ_i

$$\mathcal{N}(\Delta t; \mu_i, \sigma_i) = \frac{1}{\sqrt{2\pi}\sigma_i} e^{-\frac{(x - \mu_i)^2}{2\sigma_i^2}}$$

The binned likelihood is a function in the parameter space $\vec{\xi}$:

$$L(\vec{\xi}; \vec{n}) = \prod_i P(n_i; \lambda_i)$$

\vec{n} is the array containing the number of observed counts n_i for each i -bin, while $P(n_i; \lambda_i)$ is the Poisson distribution of the occurrences in the i -bin

$$P(n_i; \lambda_i) = e^{-\lambda_i} \frac{\lambda_i^{n_i}}{n_i!}$$

where λ_i is the expected number of events in the i -bin

$$\lambda_i = \int_{\text{bin}_i} N p(\Delta t; \vec{\xi}) d(\Delta t)$$

the total number of events N can be also let free as a nuisance parameter. The maximum likelihood fit consists in finding the minimum, in the parameter space $\vec{\xi}$, of

$$-\ln L = \sum_i (\lambda_i - n_i \ln \lambda_i)$$

defined up to constants. For the minimization of $-\log L$ we use the MINUIT package.

Table 5.1: Parameters optimized fitting the proper time resolution of the 3-prong tau using the pdf (5.1). The fit is performed on the signal $\tau(\rightarrow \rho\nu)\tau(\rightarrow \pi\pi\pi\nu)$ events and on the other $\tau\tau$ (background) events. The mean values of the two wider Gaussians are fixed to zero.

	$\tau\tau$ signal	$\tau\tau$ background
N	$(6.671 \pm 0.008) \times 10^5$	$(1.658 \pm 0.004) \times 10^5$
μ_1 [fs]	-3.22 ± 0.12	-4.4 ± 0.3
σ_1 [fs]	61.6 ± 0.2	71.0 ± 0.5
ε [%]	28.6 ± 0.4	27.8 ± 0.7
σ_2 [fs]	140 ± 1	176 ± 3
δ [%]	4.2 ± 0.1	3.7 ± 0.2
σ_3 [fs]	386 ± 3	500 ± 10

In table 5.1 the optimized parameters using the pdf (5.1) are listed for the proper time residual distributions of pure $\tau\tau$ signal and $\tau\tau$ with non $\rho\nu \times \pi\pi\pi\nu$ decays. Figure 5.3 shows the two fits superimposed to the respective distributions. The mean value of the two Gaussians having larger σ , labeled as 2 and 3, are fixed to $\mu_2 = \mu_3 = 0$. So that the only location parameter is the mean value μ_1 of the narrower Gaussian. In both distributions a negative bias is present. The major difference between the two fit are the standard deviation of the Gaussians, that are about 20% larger for the tau pair background. An overall resolution can be defined as

$$\sigma = \sqrt{(1 - \varepsilon - \delta) \sigma_1^2 + \varepsilon \sigma_2^2 + \delta \sigma_3^2}$$

and we find out $\sigma = 120$ fs for the $\tau\tau$ signal and $\sigma = 146$ fs for the $\tau\tau$ background.

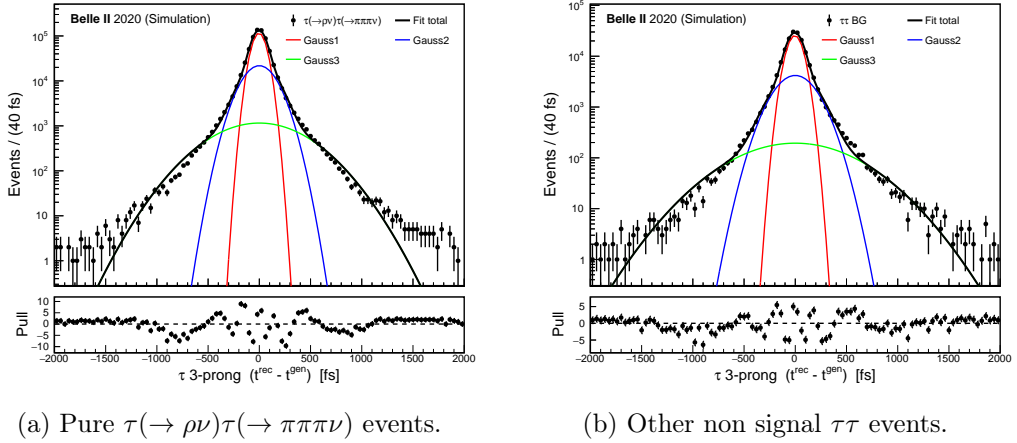


Figure 5.3: Distributions of the difference between reconstructed and generated proper decay time for the 3-prong tau. Maximum binned likelihood fits are performed with the pdf (5.1). The single Gaussian components are shown separately. The mean values of Gauss2 and Gauss3 are fixed to zero. The MC events included correspond to 200 fb^{-1} .

"Belle" function

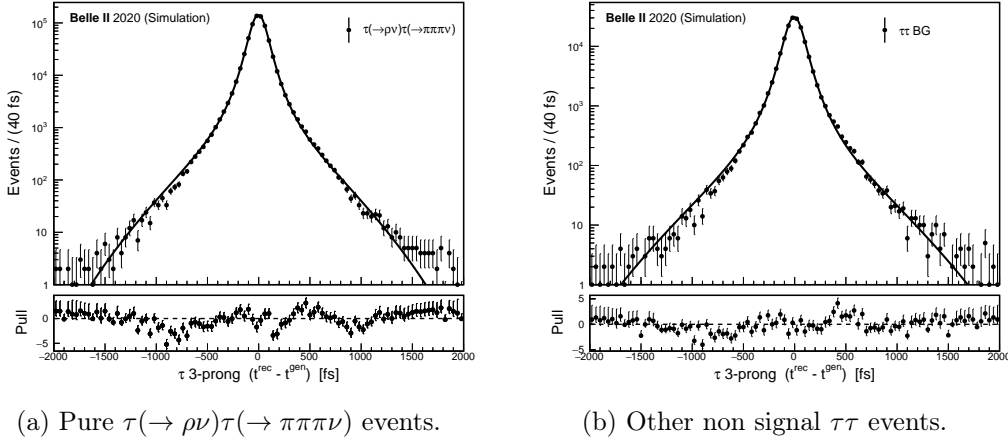
A better model is represented by the resolution function used in the Belle τ -lifetime measurement [12]. It is parametrized as a Gaussian distribution where the standard deviation is written like a series expansion of the observable $\Delta t = t^{\text{rec}} - t^{\text{gen}}$

$$\mathcal{R}(\Delta t; t_0, a, b, c, d) = N e^{-\frac{(\Delta t - t_0)}{2\sigma^2}} \quad (5.2)$$

where

$$\sigma = a + b|\Delta t - t_0|^{1/2} + c|\Delta t - t_0| + d|\Delta t - t_0|^{3/2}$$

The normalization coefficient N is computed integrating numerically over Δt and it depends on all the parameters. The advantage of function (5.2) is that there is only one location parameter (t_0) while the other (a, b, c, d) account for the variation of the width.



(a) Pure $\tau(\rightarrow \rho\nu)\tau(\rightarrow \pi\pi\pi\nu)$ events.

(b) Other non signal $\tau\tau$ events.

Figure 5.4: Distributions of the difference between reconstructed and generated proper decay time for the 3-prong tau. Maximum binned likelihood fits are performed with the pdf (5.2). The MC events included correspond to 200 fb^{-1} .

The maximum likelihood binned fits performed both on pure $\tau(\rightarrow \rho\nu)\tau(\rightarrow \pi\pi\pi\nu)$ and on the rest of $\tau\tau$, exploiting this pdf, are shown in Figure 5.4. The parameters obtained from the optimization are listed in the second and third columns of table 5.2. As noted in the previous fit with the 3-Gaussian combination, the location parameter is again negative for both fits and the other parameters confirm that the non signal tau pair proper time residual is distributed with a slightly larger width.

The same fit can be performed on the whole $\tau\tau$ set, without making distinction of events which are not really $\tau(\rightarrow \rho\nu)\tau(\rightarrow \pi\pi\pi\nu)$, but anyway are τ decays. The results of such fit are in the last column of 5.2 and the best fitted function is shown in Figure 5.5. As expected, the parameters found are closer to the ones obtained for $\tau\tau$ signal, which contains about 4 times more events than the other tau pairs.

Table 5.2: Fitted parameter for the residual τ 3-prong proper time distributions. The fits are performed using the (5.2) "Belle" pdf. The two different classes of tau pairs and their sum are separately considered. The MC events are equivalent to 200 fb^{-1} .

	$\tau\tau$ signal	$\tau\tau$ background	$\tau\tau$ all
Events (200 fb^{-1})	667137	165893	833030
t_0 [fs]	-2.75 ± 0.10	-3.7 ± 0.2	-2.93 ± 0.09
a [fs]	86.6 ± 0.9	92 ± 2	85.3 ± 0.08
b [$\text{fs}^{1/2}$]	-7.13 ± 0.15	-6.8 ± 0.3	-6.67 ± 0.13
c	0.594 ± 0.008	0.568 ± 0.017	0.567 ± 0.007
$d \times 10^3$ [$\text{fs}^{-1/2}$]	-6.6 ± 0.1	-5.7 ± 0.3	-6.0 ± 0.1

The distribution of the residual shows a better agreement with the unity than for the 3 Gaussian pdf used for Figure 5.3. Hereafter the proper time resolution will be modeled using the pdf (5.2).

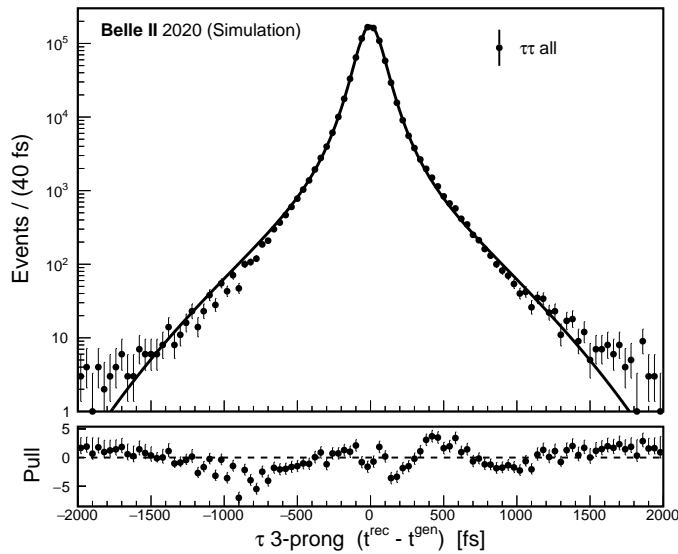


Figure 5.5: Distribution of the difference between reconstructed and generated proper decay time for the 3-prong tau. All the tau pair events passing the selections are included. A maximum binned likelihood fit has been performed with the pdf (5.2).

One last check to be done on the resolution function is its dependence on the generated proper time itself. At the scope, 4 approximately equally populated interval of (true) proper time have been selected and the fit on the full $\tau\tau$ MC sample was performed. The results for the optimized location parameter are collected in table 5.3. The value of the bias t_0 depends on the proper time range. This is an undesired behavior, whose origin needs to be further understood as it may add a systematic

Table 5.3: Fitted location parameter of the resolution function (5.2) considering 4 different intervals of true proper time. The full $\tau\tau$ distribution is considered.

t_{τ}^{gen} [fs]	(0, 80)	(80, 200)	(200, 400)	(400, $+\infty$)
Events (200 fb $^{-1}$)	200612	213923	208256	210239
t_0 [fs]	0.7 ± 0.2	-2.9 ± 0.2	-3.1 ± 0.1	-9.5 ± 0.2

contribution to the final lifetime estimation.

5.2.2 Background subtraction

Besides $\tau\tau$ events, the sample passing the selection cuts contains non- $\tau\tau$ background as well. In order to perform a fit on the proper time t^{rec} distribution, the background needs to be also modeled. For this purpose, the MC distributions are exploited, assuming that they consistently reproduce the actual background on data.

From the MC simulation, the dominant background component is represented by the $q\bar{q}$ type, where q includes u , d , s and c quarks. Among the other types of background simulated, the only relevant ones are the $B\bar{B}$ mesons coming from the $\Upsilon(4S)$ resonance.

We now split all these quark-antiquark events into two categories: light quarks u , d , s and heavy quarks c , b . For the firsts, all the measured tracks are expected to come from the interaction point, thus the (fake) reconstructed tau-candidates should have zero decay time. On the contrary, the reconstruction on $c\bar{c}$ and $b\bar{b}$ events could result in some decay time component, due to the presence of intermediate D or B hadrons.

u , d , s quarks background

The reconstructed proper time distribution is studied for the $q\bar{q}$ background, with $q = u, d, s$. This category constitutes the 1.87% of the total MC yields. We expect that no lifetime component should be present, then the t^{rec} distribution can be simply fitted with the resolution pdf (5.2).

The fitted function is shown in Figure 5.6, while in table 5.4 are listed the parameters optimized through the binned maximum likelihood fit. As evident from the normalized residuals, the shape of the distribution is well reproduced by the fit. Not surprisingly, the a^{uds} parameter, describing the width around the center t_0^{uds} , is larger than what found for the tau pair events. Indeed, the kinematic relations (3.4) are not true for $q\bar{q}$ events, because there are no neutrinos. However, the vertex relations (3.5) and (3.7) are still valid, in the special case $\ell_{\tau\pm} = 0$. Unlike the tau pairs, the fitted bias t_0^{uds} for light $q\bar{q}$ is compatible with zero. This agrees with the observation that the negative bias increases selecting higher true proper times (see table 5.3).

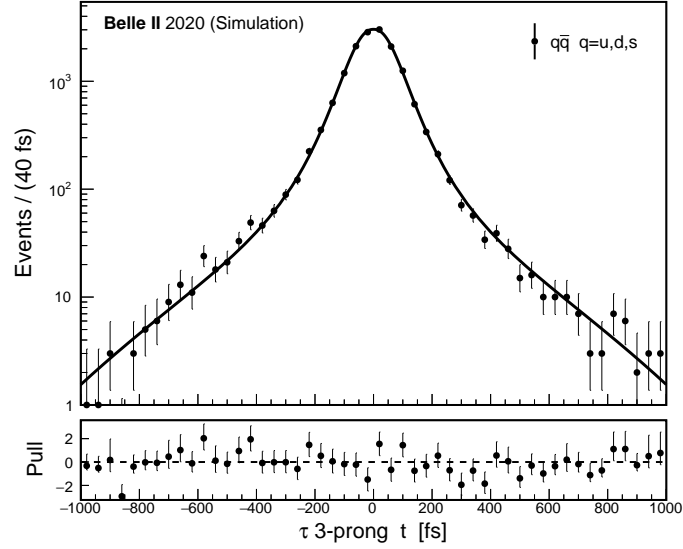


Figure 5.6: Distribution of the difference between reconstructed and generated proper decay time on the reconstructed 3-prong tau candidate for the $q\bar{q}$ background, with $q = u, d, s$ quarks. A maximum binned likelihood fit has been performed with the pdf (5.2).

Table 5.4: Optimized parameters for the proper time distribution of $q\bar{q}$ background, $q = u, d, s$ quarks. A binned maximum likelihood fit was done using the pdf (5.2) (Figure 5.6).

		$\bar{q} q = u, d, s$
t_0^{uds}	[fs]	0.1 ± 0.7
a^{uds}	[fs]	113 ± 4
b^{uds}	[fs ^{1/2}]	-11.1 ± 0.7
c^{uds}		0.82 ± 0.04
d^{uds}	[fs ^{-1/2}]	$(-10.1 \pm 0.8) \times 10^{-3}$

c, b quarks background

In the MC selected sample, the $q\bar{q}$ background where q is a c or b quark, represents a fraction 0.24% of the total. The shape of the proper time distribution is more difficult to understand and requires a deeper study. A first possibility is the convolution of an exponential with the same resolution function fitted for the u, d, s background (table 5.4). This accounts for events having non-zero lifetime but doesn't fit the region around $t^{\text{rec}} = 0$. Therefore, two normalized Gaussian pdfs with zero mean value are added. The chosen pdf for modeling the reconstructed proper time t for c and b quark events is

$$\mathcal{S}_{cb}(t; t_0^{cb}, \tau^{cb}, \varepsilon, \sigma_1, \delta, \sigma_2) = (1 - \varepsilon - \delta) \left[\frac{e^{-\frac{t}{\tau^{cb}}}}{\tau^{cb}} * \mathcal{R}_{uds}(t; t_0^{cb}) \right] + \varepsilon \mathcal{N}(t; 0, \sigma_1) + \delta \mathcal{N}(t; 0, \sigma_2) \quad (5.3)$$

\mathcal{R}_{uds} is the pdf (5.2) with the width parameters fixed to the values of table 5.4, a^{uds} , b^{uds} , c^{uds} and d^{uds} , obtained for proper time distribution of light quarks. The binned maximum likelihood fit with the pdf (5.3) returns the parameters of table 5.5. The fitted function and its single components are plotted in Figure 5.7.

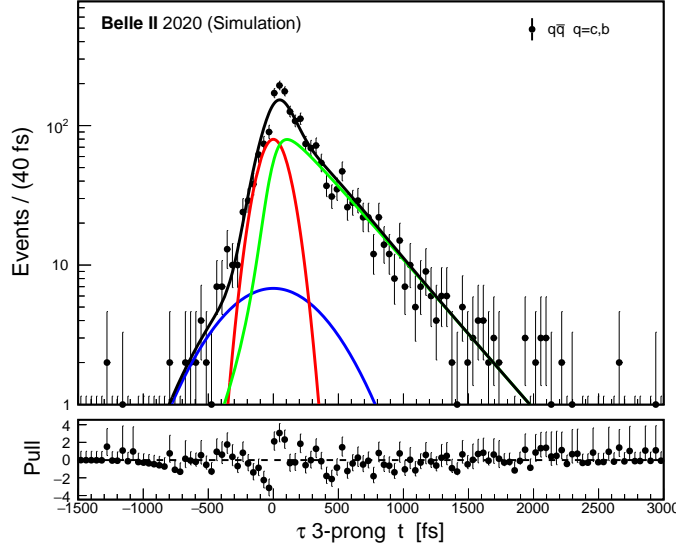


Figure 5.7: Maximum likelihood binned fit on the reconstructed proper time distribution of the tau 3-prong candidate. The MC sample includes the $c\bar{c}$ and $b\bar{b}$ events passing all the selections. The three components of the pdf (5.3) are shown in different colors.

The exponential decay component has a fitted mean life of (405 ± 15) fs, the same order of magnitude of mesons D^0 , D_s^\pm and B^\pm . The location parameter t_0^{cb} is again negative.

Table 5.5: Fitted parameter for the $q\bar{q}$ background distribution, with $q = c, b$ quarks. The fit is done with the pdf (5.3).

		$\bar{q} \ q = c, b$
t_0^{cb}	[fs]	-7 ± 2
τ^{cb}	[fs]	405 ± 15
ε	[%]	29 ± 3
σ_1	[fs]	118 ± 9
δ	[%]	8 ± 2
σ_2	[fs]	400 ± 50

5.3 Lifetime fit

The single pdfs, which have been found to model the simulated $\tau\tau$ signal and the $q\bar{q}$ background, are put together in order to extrapolate the tau mean decay time from data. The normalized pdf that describe the tau proper decay time t for the total selection is thus

$$p(t; t_0, a, b, c, d, \tau_\tau) = (1 - f_{uds} - f_{cb}) \left[\frac{1}{\tau_\tau} e^{-\frac{t}{\tau_\tau}} * \mathcal{R}(t; t_0, a, b, c, d) \right] + f_{uds} \mathcal{R}_{uds} + f_{cb} \mathcal{S}_{cb} \quad (5.4)$$

the exponential distribution with mean life τ_τ is convoluted with \mathcal{R} , the resolution function (5.2). The convolution is computed numerically with discrete Fourier transform. \mathcal{R}_{uds} and \mathcal{S}_{cb} are the parametrization for the u, d, s and c, b quark-antiquark background respectively, weighted with the relative fractions f_{uds} and f_{cb} . All the parameters of \mathcal{R}_{uds} and \mathcal{S}_{cb} are fixed to the MC-optimized values of tables 5.4 and 5.5. Also the background fractions are set to be equal to the relative yields in the MC: $f_{uds} = 0.0187$ and $f_{cb} = 0.0024$. The only free parameters are thus t_0, a, b, c, d and the mean life τ .

A binned maximum likelihood fit is performed on the 3-prong tau reconstructed proper decay time. The full data set passing the selection is used. The fit is shown in Figure 5.8, together with the $q\bar{q}$ and the total MC contributions, scaled to the data integrated luminosity. The optimized parameters are in the second column of table 5.6. The third column contains the parameters obtained from the fit, using the same pdf, on the total MC, where the number of produced tau pairs is equivalent to 200 fb^{-1} luminosity.

The parameters t_0 and τ present a disagreement between data and MC, respectively of 3 and 4 standard deviations. The discrepancy of the location parameter t_0 is relevant, as a change of sign of the offset could indicate a different resolution function in data respect to MC. Also, regarding the total MC, the compatibility with the fitted resolution function (last column of table 5.2) is marginal. Furthermore, the mean value of the proper decay time at the generator level is $\tau_\tau^{\text{gen}} = (289.4 \pm 0.3) \text{ fs}$, for the 3-prong tau, in strong disagreement with the lifetime fitted on the MC sample.

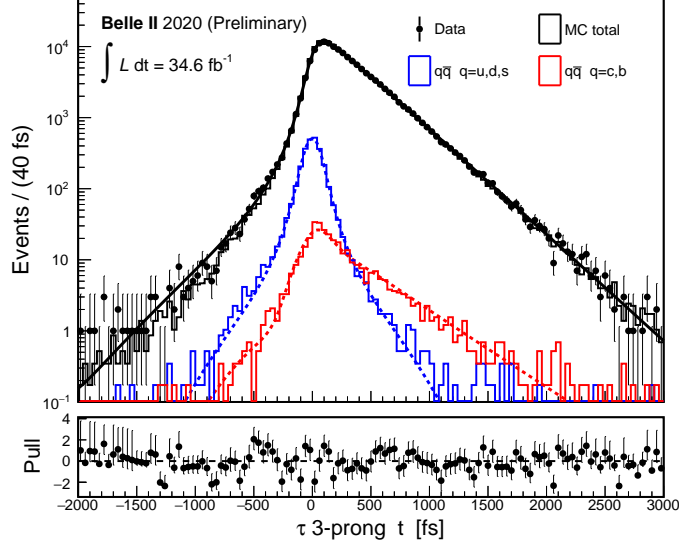


Figure 5.8: Fit of the reconstructed tau 3-prong proper time for the selected data set. The pdf (5.4) was used to build the binned likelihood. The total and $q\bar{q}$ background MC distributions are superimposed in the plot, scaled to the data integrated luminosity. The dashed lines are the single fitted components for the $q\bar{q}$ backgrounds, whose parameters are all fixed.

Table 5.6: Parameters optimized from the maximum likelihood fit binned, using the pdf (5.4). The fit is performed, after applying all the selection cuts, on the data and on the total MC sample.

	Data $\int \mathcal{L} dt = 34.6 \text{ fb}^{-1}$	MC $\int \mathcal{L} dt = 200 \text{ fb}^{-1}$
t_0 [fs]	1.1 ± 0.7	-2.1 ± 0.3
a [fs]	72 ± 1	76 ± 3
b [$\text{fs}^{1/2}$]	-4.5 ± 1.0	-5.4 ± 0.5
c	0.46 ± 0.05	0.49 ± 0.02
d [$\text{fs}^{-1/2}$]	$(-4.1 \pm 0.8) \times 10^{-3}$	$(-4.7 \pm 0.4) \times 10^{-3}$
τ_τ [fs]	287.7 ± 1.0	284.5 ± 0.4

Naively, assuming that MC reproduces data accurately, the fitted decay time τ_τ^{data} for the data can be corrected applying the same scale factor observed for the MC lifetime. An estimation of the true value would then be:

$$\tau_\tau = \frac{\tau_\tau^{\text{gen}}}{\tau_\tau^{\text{MC}}} \tau_\tau^{\text{data}} = (292.7 \pm 1.1) \text{ fs}$$

This result would be 2 standard deviations in excess respect to the present PDG average (290.3 ± 0.5) fs. Here the uncertainty is only statistical and systematic effects should be considered as well. Anyway, further studies are required and, instead of rescaling τ_τ^{data} , the discrepancy between generated and fitted lifetime in the MC should be clearly understood.

A deeper investigation would be needed in order to understand the dependence of t_0 on the proper time (table 5.3) and how it can affect the mean life, being t_0 anti-correlated to τ_τ . Apart from this, we propose a list of some of the possible systematic contributions to be studied:

- Data/MC modelling, i.e. at what level of precision the MC reproduces the data and in particular the $q\bar{q}$ background, whose parametrization is fixed from MC. The effect on τ_τ can be investigated varying the background parameters in the total fit, and if necessary the $q\bar{q}$ fraction can be further reduced with aimed cuts.
- The choice of the resolution function. It needs to be understood how the convolution with different resolution functions can affect the lifetime parameter in the fit. Other parametrizations can better describe the residual distribution of Figure 5.5.
- Possible bias in the reconstruction due to correlations of the different optimized parameters. This can be deepened fixing same variable or changing the starting values. In general an improvement of the minimization performance would be helpful.
- Correction on the total initial energies. We have already shown that in a fraction of events the total energy of taus is different from the assumed beam energy. A systematic overestimation of the tau momenta would shift the mean proper time to lower values. This important effect should be mitigated through the implemented cut on the minimum of F_{kin} . In addition, the deposited energy in the ECL, should be sensible to photons from ISR/FSR radiation losses.
- Vertical position of the beam spot IP_y , fixed to its nominal value. Varying it in the minimization could be enough to prove whether it may contribute to the systematics.
- Alignment and deformation of the VXD. This was the dominant systematic contribution for the τ lifetime measurement at Belle [12]. It can be studied looking at eventual angular dependence of the mean life and requires a very good understanding of PXD and SVD.

With more statistics, some of these aspects could be clarified analyzing the 3-prong \times 3-prong decay as well. From the branching ratio, this topology is roughly expected to have a signal yield 5 times lower than the one considered in the present study.

Conclusions and outlook

In this thesis a new method for τ -lepton lifetime measurement has been studied. The method is designed specifically for the Belle II experiment, where, at the interaction point (IP), the nano-beam collision scheme provides a beam spot having a vertical size below $1\ \mu\text{m}$.

In events of the type $e^+e^- \rightarrow \tau^+\tau^-$, where both taus decay to hadrons, the momentum vectors of taus and neutrinos can be reconstructed with a two-fold ambiguity. The ambiguity is resolved imposing the vertical position of the IP and using the measured impact parameter, for tau decaying 1-prong, or the fitted secondary vertex, in case of a 3-prong tau. The conditions added to remove the ambiguity are functions of the τ^+ and τ^- decay lengths. The whole constraints are put together into a positive defined function, and the unknown quantities are extracted through a numerical minimization. The reconstructed momenta and decay lengths eventually give the proper decay time of each tau.

A preliminary selection was developed on $34.6\ \text{fb}^{-1}$ integrated luminosity Belle II data. The target $\tau(\rightarrow \rho\nu)\tau(\rightarrow \pi\pi\pi\nu)$ topology, has been selected with a 78.4% purity and 8.0% efficiency. The minimization procedure, restricted to the energy-momentum constraints, made possible an additional cut, as the minimum value found is sensible to the event topology and to the total initial energy. Such selection is completely new in literature and may improve other τ -physics analysis, besides lifetime measurement.

The reconstruction method, applied to the selected data sample, leads to a 0.4% statistical uncertainty on the lifetime of the 3-prong tau. Anyway, the estimate obtained needs to be carefully checked, with special regard to the dependence of the resolution function on the proper time. Moreover, all the systematic contributions have still to be evaluated. From this side, the strength of the developed method is its applicability to all the different hadronic tau decay topologies, and the possibility of using several control parameters. On the other hand, the correlation between different parameters must be treated with caution, as it could introduce undesired systematics.

For the 1-prong \times 3-prong investigated topology, the τ lifetime measurement is expected to become competitive respect to the present PDG average at about $170\ \text{fb}^{-1}$ integrated luminosity. About 5 times more statistics would be needed to be competitive using the 3-prong \times 3-prong topology. Over the next decade, Belle II aims to collect a total of $50\ \text{ab}^{-1}$ integrated luminosity, thus a 0.01% statistical uncertainty could

be potentially reached. The systematic will therefore represent the dominant source of uncertainty. This is the reason why the exploration of new methods, as the one proposed in this thesis, is decisive in attempting to lower the systematics.

Together with the τ to leptons branching ratio, the τ lifetime measurement is a fundamental element for testing the universality of the weak coupling constants in the lepton sector. The improvement in the uncertainty possible at Belle II, would be a very strong challenge to the SM lepton flavor universality.

During its operation, Belle II will produce about 50 billions of $\tau^+\tau^-$ pairs in a clean environment. The full data sample will be an unprecedented amount for the tau physics in general making possible further tests on the SM, in particular for lepton flavor violating decays.

Bibliography

- [1] Mark Thomson. *Modern Particle Physics*. Cambridge University Press, 2013.
- [2] F. Halzen and Alan D. Martin. *Quarks and Leptons: an introductory course in Modern Particle Physics*. New York: Wiley, Jan. 1984.
- [3] Gianfranco Bertone, Dan Hooper, and Joseph Silk. “Particle dark matter: evidence, candidates and constraints”. In: *Physics Reports* 405.5-6 (Jan. 2005), pp. 279–390.
- [4] M. Tanabashi et al. “Review of Particle Physics”. In: *Physical Review D* 98 (3 Aug. 2018).
- [5] E. Kou et al. “The Belle II Physics Book”. In: *Progress of Theoretical and Experimental Physics* 2020.2 (Feb. 2020).
- [6] “Electroweak Measurements in Electron-Positron Collisions at W-Boson-Pair Energies at LEP”. In: *Physics Reports* 532.4 (Nov. 2013), pp. 168–170.
- [7] ATLAS Collaboration. “Test of the universality of τ and μ lepton couplings in W -boson decays from $t\bar{t}$ events with the ATLAS detector”. In: (July 28, 2020). arXiv: 2007.14040v1 [hep-ex].
- [8] Gregory Ciezarek et al. “A challenge to lepton universality in B-meson decays”. In: *Nature* 546.7657 (June 2017), pp. 227–233.
- [9] Yasmine Sara Amhis et al. “Averages of b -hadron, c -hadron, and τ -lepton properties as of 2018”. In: (2019). arXiv: 1909.12524 [hep-ex].
- [10] Alberto Lusiani. “Status and progress of the HFLAV-Tau group activities”. In: (Apr. 23, 2018). arXiv: 1804.08436v3 [hep-ex].
- [11] P. A. Zyla et al. “Review of Particle Physics”. In: *Prog. Theor. Exp. Phys.* 083C (01 2020).
- [12] K. Belous, M. Shapkin, and A. A. Sokolov. “Measurement of the τ -lepton Lifetime at Belle”. In: *Physical Review Letters* 112 (3 Jan. 2014), p. 031801.
- [13] Kazunori Akai, Kazuro Furukawa, and Haruyo Koiso. “SuperKEKB Collider”. In: (Sept. 6, 2018). arXiv: 1809.01958v2 [physics.acc-ph].
- [14] SuperB Collaboration. “SuperB: A High-Luminosity Asymmetric $e^+ e^-$ Super Flavor Factory. Conceptual Design Report”. In: *INFN Publishing Services* (Sept. 4, 2007). arXiv: 0709.0451v2 [hep-ex].

- [15] T. Abe et al. *Belle II Technical Design Report*. Nov. 1, 2010. eprint: 1011.0352 (physics.ins-det).
- [16] Ikeda H. et al. “A detailed test of the CsI(Tl) calorimeter for BELLE with photon beams of energy between 20 MeV and 5.4 GeV”. In: *Nuclear Instruments and Methods in Physics Research Section A: Accelerators, Spectrometers, Detectors and Associated Equipment* 441.3 (Mar. 2000), pp. 401–426.
- [17] S. Jadach, B. F. L. Ward, and Z. Wa. “The precision Monte Carlo event generator for two-fermion final states in collisions”. In: *Computer Physics Communications* 130.3 (Aug. 2000), pp. 260–325.
- [18] Swagato Banerjee et al. “Tau and muon pair production cross-sections in electron-positron annihilations at $\sqrt{s} = 10.58$ GeV”. In: *Physical Review D* (June 22, 2007). arXiv: 0706.3235v2 [hep-ph].
- [19] Tobias Schlüter. “Vertexing and Tracking Software at Belle II”. In: *PoS (Vertex2014)* (Nov. 13, 2014). arXiv: 1411.3485v1 [physics.ins-det].
- [20] P. V. C. Hough. *Method and Means for Recognizing Complex Patterns*. Dec. 1962.
- [21] R. E. Kalman. “A New Approach to Linear Filtering and Prediction Problems”. In: *Journal of Basic Engineering* 82.1 (Mar. 1960), pp. 35–45.
- [22] J. F. Krohn et al. “Global Decay Chain Vertex Fitting at B-Factories”. In: *Nuclear Instruments and Methods in Physics Research Section A: Accelerators, Spectrometers, Detectors and Associated Equipment* 976 (Jan. 31, 2019). arXiv: 1901.11198v1 [hep-ex].
- [23] G. Alexander et al. “Improved measurement of the lifetime of the τ lepton”. In: *Physics Letters B* 374.4 (May 1996), pp. 341–350.
- [24] The ALEPH Collaboration. “Updated measurement of the tau lepton lifetime”. In: *Physics Letters B* 414.3-4 (Oct. 23, 1997), pp. 362–372. arXiv: hep-ex/9710026v1 [hep-ex].
- [25] L3 Collaboration. “Measurement of the Lifetime of the Tau Lepton”. In: *479* (Mar. 16, 2000), pp. 67–78. arXiv: hep-ex/0003023v1 [hep-ex].
- [26] The DELPHI Collaboration. “A precise measurement of the tau lifetime”. In: *The European Physical Journal C* 36.3 (Aug. 2004), pp. 283–296.
- [27] Alberto Lusiani. “Measurement of the Tau Lepton Lifetime with BaBar”. In: *Nuclear Physics B - Proceedings Supplements* 144 (July 2005), pp. 105–112.
- [28] J. H. Kühn. “Tau kinematics from impact parameters”. In: *Physics Letters B* 313.3-4 (Sept. 1993), pp. 458–460.
- [29] Jorge Nocedal and Stephen J. Wright. *Numerical Optimization*. New York, NY: Springer New York, Dec. 11, 2006. Chap. Quasi-Newton Methods, pp. 135–163.
- [30] Robin Leboucher. “Good track selection for tau events”. In: *Belle II Notes (Internal)* (June 2020).

- [31] A. Selce, T. Koga, and S. Stengel. “Optimization of π^0 reconstruction selection and first systematic uncertainty evaluation of the efficiencies”. In: *Belle II Notes (Internal)* (Feb. 2020).
- [32] Xin Chen and Yongcheng Wu. “Search for the Electric Dipole Moment and anomalous magnetic moment of the tau lepton at tau factories”. In: *J. High Energ. Phys.* 89 (10 Oct. 2019).